國立交通大學

光電工程研究所

博士論文

具混合式反射鏡共振腔氮化鎵面射型雷射之研究

Study of Nitride-Based Vertical-Cavity Surface Emitting Lasers with Hybrid Mirrors

研 究 生：高 志 強

指導教授：王 興 宗 教授

郭 浩 中 教授

中華民國 九十六 年 九 月

國 立 交 通 大 學

光電工程研究所

博士論文

具混合式反射鏡共振腔氮化鎵面射型雷射之研究

Study of Nitride-Based Vertical-Cavity Surface Emitting Lasers with Hybrid Mirrors

研 究 生：高 志 強　　Student: Chih-Chaing Kao

指導教授：王 興 宗　　Advisor: Shing Chung Wang

郭 浩 中　　Hao-Chung Kuo

中華民國 九十六 年 九 月

具混合式反射鏡共振腔氮化鎵面射型雷射之研究

Study of Nitride-Based Vertical-Cavity Surface Emitting Lasers with Hybrid Mirrors

研 究 生：高 志 強　　Student: Chih-Chaing Kao

指導教授：王 興 宗　　Advisor: Shing-Chung Wang

郭 浩 中　　Hao-Chung Kuo

國立交通大學

光電工程研究所

博士論文

A dissertation

Submitted to Institute of Electro-optical Engineering

College of Electrical Engineering and Computer Science

National Chiao Tung University

In Partial Fulfillment of the Requirements

For the Degree of

Doctor of Philosophy

In Electro-Optical Engineering

September 2007

Hsin-chu, Taiwan, Republic of China

中華民國 九十六 年 九 月

具混合式反射鏡共振腔氮化鎵面射型雷射之研究

研究生:高志強　　指導教授:王興宗　教授

郭浩中　教授

國立交通大學光電工程研究所

摘要

在過去數年來，氮化鎵系列材料已被廣泛使用於許多光電元件諸如發光二極體與雷射二極體以及光偵測器，而這些元件更被加以大量應用於光儲存、平面顯示、照明及生物科技中。也因為其應用面相當的廣大，氮化鎵材料吸引了不少研究的目光。

本論文旨在發展具混合式反射鏡共振腔之氮化鎵光激發面射型雷射的製作方法並研究其雷射特性。在此研究中，所設計製作的氮化鎵面射型雷射乃由一個光程約五倍波長的共振腔、一組鋁化鎵/氮化鎵之布拉格反射鏡與一組氧化物反射鏡所組成。其雷射之臨界激發能量約為 2.6 mJ/cm^2 而其所輻射波長為 456.2 nm 且半高寬僅僅 0.2 nm.此外，其極化程度與發散角皆相當優異，可分別達到 84%與 7.6 度。更特別的是，此雷射的自發輻射耦合率高達 0.02，是一般邊射型雷射的 1000 倍之高，這代表著其效率被微共振腔大幅提高。我們還發現了多個雷射點與穩定模態情況，這情況與共振腔與增益介質之不均勻有著極大關係。

我們進一步建立了電激發面射型雷射的製程並將此製程應用於光激發面射型雷射結構上製作出一個具有非長高品質因子的微共振腔發光二極體。我們在製程中使用了高透明度的氧化錫銦做為透明電極來減少吸收。此元件之發光波長落於 463.2 nm，於 10 微安時，其半高可達至 0.52 nm，即數值約 895 的品質因子。這表示著已相當接近雷射操作的可能。

最後，我們更發展了光激發的光子晶體面射型雷射，我們製作了不同週期(190 nm – 300 nm)的光子晶體且皆達到了大面積雷射操作，雷射波長落於 395 nm 到 425 nm。此種雷射具有的極化與發散角分別約為 53%與小於 10 度。由對照粗

略理論的計算，我們發現雷射乃發生於光子晶體能帶的邊緣交集處，也就是滿足布拉格條件處，且越大的光子晶體週期會對應到具較高的歸一頻率的能帶邊緣，這可充份提供設計此種雷射的線索，而此實驗成果亦充份顯示此種雷射有相當大潛力應用於高功率大面積單模雷射。

Study of Nitride-Based Vertical-Cavity Surface Emitting Lasers with Hybrid Mirrors

Student: Chih-Chiang Kao Advisor: Dr. Shing-Chung Wang

Dr. Hao-Chung Kuo

Department of photonics & Institute of Electro-Optical Engineering
National Chiao-Tung University

Abstrate

Over past few years, ntride-based materials have been widely used in several optoelectronic devices, such as light emitting diodes, laser diodes, and photo-detectors. These devices have highly potential in the applications such as flat panel display, competing storage technologies, automobiles, general lighting, and biotechnology, and so on. Therefore, nitride wide-bandgap devices have attracted lots of attention.

In this study, we have demonstrated the fabrication of the optically-pumped nitride-based vertical cavity surface emitting laser (VCSEL) with hybrid mirrors and investigated characteristics of this kind of laser. The nitride-based VCSEL was formed by a five-lamda (λ) micro-cavity sandwiched by hybrid DBR mirrors, consisting of AlN/GaN DBR and Ta_2O_5/SiO_2 DBR. The laser action was observed under the optical pumping at room temperature with a threshold pumping energy density of about 2.6 mJ/cm^2. The GaN VCSEL emits 456 nm blue wavelength with a linewidth of 0.2 nm and the laser beam shows a large degree of polarization of about 84%, a high characteristic temperature to be about 244 K, and a small divergence angle to be about 7.6^o. The coupling efficiency of spontaneous emission (β) of our VCSEL was fitted to be a value as high as 0.02, which is three order of magnitude

higher than that of the typical edge emitting semiconductor lasers (normally about 10^{-5}), indicating the enhancement of the spontaneous emission into a lasing mode by the high quality factor microcavity effect in the VCSEL structure. Furthermore, we found the multiple laser spots and stable mode behaviors of the nitride-based VCSEL. These two phenomena are believed to be related with the inhomogeneous gain and cavity.

We also have established the fabrication process for nitride-based VCSELs and used the process to complete a current-injected high-Q micro-cavity light emitting diode (MCLED) based on the structure of our optically-pumped VCSEL. We used high-transparency indium-tin-oxide as our transparent contact to decrease cavity absorption. The MCLED showed a very narrow linewidth of 0.52 nm equivalent to a cavity Q value of 895 at a driving current of 10 mA and a dominant emission peak wavelength at 465.3 nm. The MCLED also showed an invariant emission peak wavelength with varying current. The results in this report should be promising for developing GaN-based VCSELs.

Finally, we have further developed a novel nitride-based 2-D photonic crystal surface emitting laser (PCSEL) and investigated characteristics of this laser device. The structure of this device composed of a 5-λ cavity, an AlN/GaN DBR, and a triangular-lattice photonic crystal with a diameter of 50 μm. The lattice constants (a) of photonic crystals were ranged from 190 nm to 300 nm with a fixed ratio of radius of hole and lattice constant being 0.28. All these devices show a similar threshold pumping energy densities to be about 3.5mJ/cm^2. These nitride-based 2-D PCSELs emit violet wavelengths ranging from 395nm to 425nm with a linewidth of about 0.11 nm, and has a degree of polarization and a divergence angle of the laser emission to be about 53% and smaller than 10^{o}, respectively. The laser emission was observed to occur over a large area nearly equal to the whole area of photonic crystal. We also found that normalized frequency of each laser emission from photonic crystal devices can exactly correspond to the points of Brillouin-zone boundary, Γ、M、K points. Furthermore, the device with a larger lattice constant of PC would lase at the PC band edge with a larger

normalized frequency. This observation could be a direction for designing this kind of laser device. These results suggest PCSEL could have strong competitiveness for the application of high power and single mode lasers.

誌謝

晃眼之間，博士班的求學之路也告了一個段落，五年時光說長不長，說短不短，卻足夠讓我這曾經稚嫩的腦袋在老師們的教導下慢慢成長，除了在待人處事與知識增長上有所進步，做事的方法與態度也有了長足的改善。而能夠全心在優秀的環境下學習並有小小的成果，全都要歸功於辛苦養育且全力支持我求學的父母、諄諄教誨的老師們與許許多多的伙伴與朋友。

王興宗老師是我最敬佩與感謝的老師，不論是老師對研究的熱忱與要求抑或是老師肚裡高深的學問，都讓我受益良多；郭浩中老師在求學路上的指導與生活上的關心也讓我深深感謝，當然，盧廷昌老師的討論與幫助更是不可或缺的助力，也有許多老師給與許多意見與建議，在此，志強深深地致上感謝之意。

實驗室是我最常活動的地點，不論是實驗或是分析，身邊來來去去的這些學長姐、同學與學弟妹可說是革命的同伴。裕鈞、宗鼎、剛帆、立凡是與我一同努力的學弟，有這些成果都是他們的汗水帶來的，我很感謝這條路有這些好學弟忍耐我急燥的個性與他們的大力幫忙；俊毅、偉倫、威佑、永龍，我一直深信我們的情誼是堅固不移的，你們在這期間的大力相助，點滴在我心；長治學長、振甫學長、忻宏學長、道鴻學長、亞衡學長、睿彥學長、鴻儒學長以及芳儀學姐等學長姐的經驗分享與知識傳授，是我能順利切入研究的源頭，十分感謝您們，尤其是待我如好友的長治學長，您的無私分享，是千萬句感謝也無法描述的；游敏、敏瑛、文登、瑞溢、潤琪、昀恬、意偵、皇伸、柏傑等學弟妹，也很感謝你們參與了我求學路，陪我做實驗、討論、去阿里山、去充電之旅、車上熱烈八卦、吃吃喝喝、慶生、酒醉等說也說不盡的趣事，我的博士生活靠你們把它填上了色彩；然而，我最感謝的人應該是小朱，我們一同出國、一同擔事、一同出遊、一同為雷射努力，我們一同約定一起讀博士一起努力，我最希望與你一同畢業，雖然陰錯陽差遇上了 SARS，無法同時畢業，我還是要感謝遇見了你，一個最沒架子的學長兼好友；泓文與詒安，也謝謝你們的協助與相伴，若不是泓文的快手與無私的分享論文，我也無法有著如今的成果，當然，你們排除萬難在公司幫忙也要對你們說聲，辛苦了!還有許多的學弟妹無法盡訴我的感謝之意，於此，向你們都說聲..謝謝。

我也要特別感謝我的舅舅們，在我的父親生病時給予了最大的關懷與幫助。

尤其是大舅，不時地在我人生路上給予最大的幫忙與意見，能順利完成學業，志強十分感謝大舅您的關心；曉芳，妳一路陪伴我成長，忍受著我的脾氣，溫柔地打點我的一切，我的一切都靠妳的體貼與付出所換得的，一同走過了九個年頭，謝謝妳，也要請妳再陪我繼續努力，我們還有很長遠的路；最後，我要感謝我的父母對我的全力支持、無怨無悔的付出與辛苦的栽培，在我心中，您們是最偉大的父母，您們讓我的心靈是富裕的，無時無刻，我都以您們為榮。於此，也將此論文獻于我的父母與家人，謝謝您們。

志強

交大光電所

2007.9.12

CONTENTS

Abstract (in Chinese) I

Abstract III

Acknowledgement VI

Contents VIII

List of tables XI

List of figures XII

Chapter 1 Introduction 1

1-1 Wide-bandgap III-N materials 1

1-2 Nitride-based semiconductor lasers 1

1-2.1 Edge Emitting Lasers 2

1-2.2 Vertical Surface Emitting Lasers 3

1-2.3 Two-Dimentional Photonic Crystal Lasers 6

1-3 Objectives of this thesis 8

References

Chapter 2 Fundamentals of Micro-Cavity Surface Emitting Lasers 17

2-1 Operation Mechanism of Semiconductor Lasers 17

2-2 Penetration Depth of Distributed Bragg Reflectors 20

2-3 Coupling Efficiency of Spontaneous Emission into a Lasing Mode 22

2-4 Characteristics of Microcavity Semiconductor Lasers 24

2-5 Band Edge Laser in a 2-D Triangular-Lattice Photonic Crystal 27

References

Chapter 3 Fabrication and Characteristics of an Optically Pumped Nitride-Based VCSEL 37

3-1 Design of a Nitride-based VCSEL 38

3-1.1 Reflectance Simulation of Ta_2O_5/SiO_2 and Nitride-Based DBRs 38

3-1.2 Optimization of Location of the Active Region in a VCSEL ··· 39
3-2 Fabrication of the Nitride-Based VCSEL Structure ····· 40
3-2.1 Growth of Nitride-Based Reflectors and Micro-Cavity ····· 41
3-2.2 Deposition of the Dielectric Mirror ····· 42
3-3 Measurement and Characteristics of Nitride-Based VCSELs ····· 42
3-3.1 Photoluminescence and Quality Factor of Nitride-Based VCSELs ·· 42
3-3.2 Characteristics of Nitride-Based VCSELs ····· 44
References

Chapter 4 Effects of Inhomogeneous Gain on Lasing Action of Nitride-based VCSEL ····· 67

4-1 Inhomogeneous Spontaneous Emission Intensity of Nitride-Based VCSELs ····· 67
4-2 Multiple Laser spots phenomenon of Nitride-Based VCSELs ····· 68
4-3 Well-Organized Mode Patterns of Nitride-Based VCSELs ····· 69
References

Chapter 5 Fabrication and Characteristics of High-Q Micro-Cavity Light Emitting Diodes ····· 86

5-1 Fabrication Processes for Nitride-based VCSELs ····· 87
5-2 Devices characteristics ····· 89
5-3 Fabrication technique for current confinement – implantation ····· 91
References

Chapter 6 Fabrication and Characteristics of nitride-based two-dimensional photonic crystal surface emitting lasers ····· 111

6-1 Fabrication Technique – Electron-Beam Lithography ····· 111
6-2 Design of Nitride-Based 2-D Photonic Crystal Surface-Emitting Lasers ·· 112

6-3 Fabrication of Nitride-Based 2-D Photonic Crystal Surface-Emitting Lasers 114
6-4 Characteristics of Nitride-Based 2-D Photonic Crystal Surface-Emitting Lasers 114
References

Chapter 7 Conclusions and Future Works 132

Publication List 138

List of tables

Chapter 3

Table 3.1 Parameters for the estimation of material gain. 60

List of figures

Chapter 1

Figure 1.1 The band-gap diagram of II-VI and III-V semiconductor materials. 12

Figure 1.2 The schematic diagram of an edge emitting laser diode. 13

Figure 1.3 The Schematic diagram of a vertical-cavity emitting laser diode. 14

Figure 1.4 Schematic diagrams of three nitride-based VCSEL structures 15

Figure 1.5 The band diagram of a 2-D triangular-lattice PC structure. 16

Chapter 2

Figure 2.1 An illustration of output power vs. current for a diode laser. 31

Figure 2.2 A schematic diagram of DBRs 32

Figure 2.3 The internal photon number n_0 versus the pump rate P as a function of a spontaneous emission coefficient β. 33

Figure 2.4 (A) The band diagram of a triangular-lattice photonic crystal. (B) The schematic diagram of a reciprocal space. 34

Figure 2.5 Wave-vector diagrams at (A) point I, (B) point II, and (C) point III. k_i and k_d indicate incident and diffracted wave vector. 35

Figure 2.6 The wave-vector diagram at point III in vertical direction. 36

Chapter 3

Figure 3.1 Simulated reflectivity spectra of 5, 10, 15, and 25 pairs of AlN/GaN DBR. 49

Figure 3.2 Simulated reflectivity spectra of three different nitride - based DBRs with high reflectivity. 49

Figure 3.3 Simulated reflectivity spectra of 3, 5, and 8 pairs of Ta_2O_5/SiO_2 DBR. 50

Figure 3.4 Electric field intensity and refractive index as a function of the distance from top layer. 50

Figure 3.5 Cross-sectional TEM images of (A) the DBR sample and (B) one set of 5.5 pairs of GaN/AlN SL insertion layers. 51

Figure 3.6 AFM image of the DBR sample. 52

Figure 3.7 The reflectivity spectrum of the AlN/GaN DBR. 53

Figure 3.8 (A) OM and (B) cross-sectional TEM images of the as-grown micro-cavity sample. 54

Figure 3.9 The reflectivity spectrum of the Ta_2O_5/SiO_2 DBR. 55

Figure 3.10 (A) Schematic diagram, (B) SEM image, and (C) OM images of the VCSEL structure. 56

Figure 3.11 PL emission of as-grown structure and VCSEL structure, and the reflectivity spectrum of VCSEL structure. 57

Figure 3.12 The optical pumping setup. 58

Figure 3.13 The light emission intensity of VCSEL as a function of the pumping energy. 59

Figure 3.14 Emission spectra of VCSEL under different pumping energy. 59

Figure 3.15 Emission images of nitride-based VCSEL under different pumping energy. 60

Figure 3.16 The laser emission intensity of VCSEL as a function of the angle of the polarizer at the pumping energy of 1.71E_{th}. ····· 61

Figure 3.17 (A) Near-field intensity distribution and (B) Far-field emission pattern of the laser spot. ····· 62

Figure 3.18 Semi natural-logarithm plot of the dependence of the threshold pumping energy (lnEth) on the operation temperature. ····· 63

Figure 3.19 The lasing wavelength of nitride-based VCSEL as a function of temperature. ····· 64

Figure 3.20 The center wavelength of AlN/GaN DBR as a function of temperature. ····· 65

Figure 3.21 Photon numbers as a function of pump ratio. The solid lines are fitting curves with β values of 0.02, 0.025, and 0.03, and the dots are experiment data. ····· 66

Chapter 4

Figure 4.1 The PL intensity distribution of one region on the as-grown sample with a scanning area of 20×20 μm^2. ····· 74

Figure 4.2 (A) The wavelength distribution of the region shown in figure 4.1. (B) The PL spectrum of the dotted circle and the reflectivity spectrum of the region. ····· 75

Figure 4.3 Emission images of multiple laser spots under four different pumping energy of 0.8 E_{th}, 1.1E_{th}, 1.3E_{th}, and 1.4E_{th}. ····· 76

Figure 4.4 Emission spectra of multiple laser spots under four

different pumping energy of 0.8 E_{th}, 1.1E_{th}, 1.3E_{th}, and 1.4E_{th}. 77

Figure 4.5 Four observed lasing emission images and intensity distributions simialr to TEM_{00}, TEM_{01}, TEM_{02} and TEM_{11} in the four different regions. 78

Figure 4.6 The threshold characteristic of pumping region I on GaN VCSEL sample. 79

Figure 4.7 The threshold characteristic of pumping region II on GaN VCSEL sample. 80

Figure 4.8 Emission spectra of the pumping region I under different pumping energy. 81

Figure 4.9 Emission spectra of the pumping region II under different pumping energy. 82

Figure 4.10 Emission spectra of nitride-based VCSEL emitting two kinds of mode patterns, similar to TEM_{01} and TEM_{11} at the same region with the same pumping energy. 83

Figure 4.11 PL Emission intensity distributions of four pumping regions shown in figure 4.5. 84

Figure 4.12 PL spectra of three places marked in the photo shown in the inset. The inset is PL emission image of the region emitting TEM01. 85

Chapter 5

Figure 5.1 Transmission (T) and reflectivity (R) versus wavelength

of Ni/Au (5/5nm) and ITO (300nm) films deposited on glass substrate. 95

Figure 5.2 Electric field intensity and refractive index as a function of the distance from top layer. 96

Figure 5.3 The process flowchart of nitride-based micro-cavity devices. 97

Figure 5.4 The current-voltage characteristic of ITO contact. 98

Figure 5.5 The schematic diagram of a fabricated micro-cavity light emitting diode. 99

Figure 5.6 SEM images of the fabricated device. (A) Top view. (B) Cross-sectional view. 100

Figure 5.7 The probe station measurement setup. 101

Figure 5.8 Current versus voltage and light output power curves of a fabricated device at room temperature. 102

Figure 5.9 (A) Emission images under different injection current. (B)A MCLED chip monted on a metal can. 103

Figure 5.10 Emission spectra of the MCLED under different current of 3 mA, 6 mA, and 10 mA. 104

Figure 5.11 The variation of emission (A)linewidth and(B)wavelength of the MCLED with increasing current. 105

Figure 5.12 Emission peak wavelength of the MCLED as a function of temperature. 106

Figure 5.13 (A) The simulation and (B) SIMS data of Mg+ ion distribution inside the implanted sample with 100nm-thick SiNx buffer layer. 107

Figure 5.14 OM image of the implanted sample. 108

Figure 5.15 (A) Emission images of Mg+ implanted MCLEDs after

deposition of ITO transparent contact layer. (B) Emission image of MCLED with aperture size of 40 μm in high magnification.(C)Emission image of fabricated implanted MCLED. 109

Figure 5.16 Current-voltage curves of the conventional and the Mg^{+}-implanted MCLEDs. 110

Chapter 6

Figure 6.1 A schematic diagram of a typical electron beam lithography system. 119

Figure 6.2 The band diagram of the 2-D triangular-lattice PC structure on our sample structure. The value of r/a here is 0.28. 120

Figure 6.3 The schematic diagram of our photonic crystal surface emitting lasers. 121

Figure 6.4 The μ-PL of as-grown sample. 122

Figure 6.5 SEM images of our photonic crystal surface emitting lasers. (A) Top view. (B) Cross-sectional view. 123

Figure 6.6 Normalized frequencies of our PCSELs as a function of lattice constant. 124

Figure 6.7 The laser emission intensity from a 2-D PCSEL as a function of the pumping energy density. 125

Figure 6.8 Emission spectra of a 2-D PCSEL under four different pumping energy densities. 126

Figure 6.9 Lasing spectra of PC devices I, II, and III with three different lattice constants, 201 nm, 244 nm, and 290 nm, respec-

tively. 127

Figure 6.10 The comparison of simulated PC band diagram (figure 6.2) and experiment data (figure 6.6). 128

Figure 6.11 (A) The spontaneous emission image at $0.92E_{th}$ (pumping spot size was about 50μm) and (B) Laser emission image at $1.47E_{th}$. 129

Figure 6.12 The laser emission intensity of a PCSEL as a function of the angle of the polarizer. 130

Figure 6.13 The laser emission intensity of a PCSEL as a function of the detecting angle of the fiber. 131

Chapter 7

Figure 7.1 Schematic diagram of a photonic crystal surface emitting laser 137

Chapter 1

Introduction

1-1 Wide-bandgap III-N materials

Wide-bandgap nitride materials have attracted great attention over past decade due to their promising potential for the applications of optoelectronic devices such as flat panel display, competing storage technologies, automobiles, general lighting, and biotechnology, and so on [1-4]. The III-N materials are synthesized mainly using the four kinds of atoms, gallium (Ga), nitride (N), aluminum (Al), and indium (In), to form the binary and ternary compunds such as GaN, InN, AlN, $In_xGa_{1-x}N$, and $Al_xGa_{1-x}N$ etc. The bandgap of these materials cover a very wide range from 0.9eV to 6.1eV (figure 1.1), which implies the large band off-set in hetero-structure could be achieved in this material system. The large band off-set is very useful to confine carrier for the high-speed and high power electronic devices and light emitting devices [5]. Their wide-range bandgap also provide possibility of full-color emission because they cover red, green, and blue emission regions. This property further makes nitride materials important and important for the applications of full-color display or solid-state lighting. Furthermore, nitride materials still have lots of advantages such as high bond energy (~2.3eV), high saturation velocity ($\sim 2.7 \times 10^4$ cm/s), high breakdown field ($\sim 2 \times 10^6$ V/cm), and strong excitonic energy (>50meV)[6-7]. Although wurtzite nitride compounds have some unique properties such as piezoelectric field and spontaneous polarization which is harmful to the efficiency of light emitting devices, the material system still is a very strong candidate for the future optoelectronic applications due to their superior material properties.

1-2 Nitride-based semiconductor lasers

The research of blue light emitting devices began from the development of gallium nitride light emitting diodes in the early 1970s [8-10]. Two decades later, with several efforts devoted to the growth of nitride materials, doping concentration, efficiency of quantum wells, and so on, Nakamura et. al. [2] developed the first prototype high-brightness (>100 times greater than previous alternatives, about 1 candela) GaN blue light emitting diodes in 1993. Then, in 1995, they also developed the first successful GaN electron-injection laser [1]. This makes nitride laser diodes begin to step on the road toward the commercial applications of high-information-density storage, laser printer, compact projector, and etc. In these years, the performance of nitride laser diodes has been improved to emit power as high as 100mW at room temperature with a low threshold only 3 kA/cm^2 [11], and the devices have been already successfully commercialized to be applied to digital versatile disc (DVD). This next-generation DVD would enlarge the storage capacity from 4.7 giga-bytes which current DVD owns to 27 giga-bytes.

1-2.1 Edge emitting lasers

The major type of commercial nitride-based laser diodes now is edge emitting laser. This kind of structure is currently the most mature and producible one among all nitride laser devices. It is featured by a stripe-type long cavity and a pair of cleaved facet as the mirrors as shown in figure 1.2. Typically, the cavity length of the structure is about several hundred micro-meters. The light in the cavity is resonant in the horizontal direction and emits from the cleaved mirrors. The standard epi-layer structure of EELs usually is grown on sapphire and composes of p-n junction, multiple quantum wells (active region), and some cladding layer for photons and electrons. Over this decade, several improvements and researches on the growth and optimization of its structure were reported [12-15]. One is to improve the great amounts of defects and threading dislocations existing in the grown nitride materials on sapphire substrate due to the large lattice-mismatch between the nitride material and sapphire.

The epitaxally lateral overgrowth (ELOG) is a very efficient method to reduce threading dislocation and defect density [12, 13]. It is a method using the patterned SiOx to make GaN laterally coalesce and bend threading dislocations to reduce the dislocation density. Generally, ELOG could decrease dislocation density down to the order of 10^8 cm^{-2}. Other one is to raise the low confinement factor of the optical field in the structure. Because the index difference between $Al_xGa_{1-x}N$ and GaN is small, the guiding of optical field in active region is usually weak. Nakamura et. al. provided a solution that using modulation doped strain superlattice layer to improve the optical confinement [12, 13]. The other is to reduce spontaneous polarization and piezoelectric field in multiple quantum wells. Recently, M. Schmidt et. al. [14] and D. Feezell [15] et. al. demonstrated nonpolar laser diode on m-plane GaN substrate. The laser diode emits violet light ~410nm and has the threshold current density of 3.7-8.2 KA/cm^2. The spontaneous and piezoelectric polarization effect was eliminated and the performance of laser diode could be further improved using this lattice matched substrate. The fabrication of flat and high-reflectivity mirrors is also a key point for achieving an excellent lasing performance. In order to obtain a flat facet, the etching and cutting techniques were rapidly developed.

1-2.2 Vertical Surface Emitting Lasers

Although the optimization of the edge emitting laser keeps going, some properties of this kind of laser are unfavorable. One of those properties is its elliptic beam shape. On one hand, the coupling efficiency would be low as the elliptic beam is coupled into optical fiber (typically in the form of circular core). On the other hand, for the application of storage, the elliptic beam not only makes each writing pixel larger but also raises expenses for correcting light shape. Usually, this kind of laser shows slightly large divergence angle to be over ten degree. This also is disadvantageous to the projection. Furthermore, the side emitting laser devices also makes the testing of devices a tough task. The wafer should be cut into several

stripes (several laser devices on one strip) before the testing. For a commercial product, the complicated testing would result in a poor producing efficiency and be disadvantageous. Therefore, in order to have a superior laser device, K. Iga [16] demonstrated a new kind of laser diodes, vertical cavity surface emitting laser, in 1977. Vertical cavity surface emitting laser (VCSEL) is a vertical-emitting-type laser. It is formed by sandwiching a few-lambda cavity in a pair of reflectors, usually in the form of distributed Bragg reflector (DBR), with a very high reflectivity (>99.9%) (as shown in figure 1.3). In contrast to EELs, photons in the cavity of VCSEL are vertically in resonance and emit outside perpendicularly to the surface of the structure. This laser diode can have many advantageous properties than conventional edge emitting laser, such as circular beam shape, lower divergence angle, two-dimensional laser array possible, efficient testing, low threshold, and so on. Owing to these superior performances, VCSELs had become very attractive and started to be applied to the commercial products at long wavelength range. In fact, short-wavelength VCSELs are also very promising for the applications of storage, display, and projection. In particular, the use of two-dimensional arrays of blue VCSELs could further reduce the read-out time in high density optical storage and increase the scan speed in high-resolution laser printing technology [17]. In recent years, several efforts have been devoted to the realization of nitride-based VCSELs [18-27]. Currently, three kinds of structures were reported:

I. Fully epitaxial grown VCSEL structure

In 2005, J. F. Carlin [26] and E. Feltin [27] demonstrated the wholly epitaxial and high quality nitride-based micro-cavity (as shown in figure 1.4(A)) using metalorganic vapor phase epitaxy (MOVPE or MOCVD). They used the lattice-matched AlInN/GaN as the bottom and top reflectors to avoid cracks happened due to the accumulation of the strain after stacking large pairs of layers. The reflectivity of AlInN/GaN could be achieved as high as 99.4%. They showed the 3/2-lambda cavity emitted a very narrow emission with a linewidth of 0.52 nm, corresponding to a quality factor of ~800.

II. VCSEL structure with two dielectric mirrors

Compared to epitaxial grown reflectors, the fabrication of dielectric mirrors is relatively simple. Furthermore, the large index difference of dielectric mirrors makes them could easily have wide stop band (>50nm) and high reflectivity (>99%) by coating just few stacks of 1/4-lambda-thick layers. Therefore, using dielectric mirrors to accomplish nitride-based VCSELs had begun attractive. Song *et al.* [19], Tawara *et al.* [20] and J. T. Chu *et. al.* [22] successively reported the structure (as shown in figure 1.4(B)) after 2000. They employed some process techniques such as wafer bonding and laser lift-off to make dielectric mirrors be coated onto both sides of nitride-based cavity. They showed a micro-cavity could have a very high quality factor to be greater than 400 and achieve lasing action using optical pumping.

III. VCSEL structure with hybrid mirrors

The so-called hybrid mirrors are a combination of two different kinds of reflectors, for example, a dielectric mirror and an epitaxial reflector. Typically, the fabrication of this structure is to grow bottom reflector and cavity using MOCVD and then coat dielectric mirror to complete VCSEL structure (as shown in figure 1.4(C)). The hybrid-cavity nitride-based VCSEL\formed by the dielectric mirror and the epitaxially grown high-reflectivity GaN/$Al_xGa_{1-x}N$ DBR was reported earlier. In 1999, Someya et al. [18] used 43 pairs of $Al_{0.34}Ga_{0.66}N$/GaN as the bottom DBR and reported the lasing action at ~400nm. Then, Zhou et al [21] also employed a bottom DBR of 60 pairs $Al_{0.25}Ga_{0.75}N$/GaN and observed the lasing action at 383.2nm. Both these AlGaN/GaN DBR structures required large numbers of pairs due to the relatively low refractive index contrast between $Al_xGa_{1-x}N$ and GaN. Therefore, recently some groups began to study the AlN/GaN for application in nitride VCSEL. The DBR structure using AlN/GaN has higher refractive index contrast ($\Delta n/n=0.16$)[28] that can achieve high reflectivity with relatively less numbers of pairs. It has wide stop band that can easily align with the active layer emission peak to achieve lasing action. However, the AlN/GaN combination also has relatively large lattice mismatch (~2.4%) and the difference in

thermal expansion coefficients between GaN (5.59×10^{-6}/K) and AlN (4.2×10^{-6}/K) that tends to cause cracks in the epitaxial film during the growth of the AlN/GaN DBR structure and could result in the reduction of reflectivity and increase in scattering loss. With the mature of epitaxy techniques, the high-reflectivity AlN/GaN DBR structure with relatively smooth surface morphology has become possible with just twenty or thirty pairs [29].

In comparison of these three VCSELs, it doesn't require complicated process such as laser lift-off technique to complete a hybrid VCSEL device. This means the fabrication of such structure is stable and reliable comparing to other structures. Thus, the hybrid structure is more advantageous in the aspects of fabrication and commercialization

In fact, the investigation of the characteristics of the GaN-based VCSELs has gradually attracted more attentions. Kako *et al.* [30] investigated the coupling efficiency of spontaneous emission (β) and the polarization property of the nitride VCSEL and obtained a high β value of 1.6×10^{-2} and a strong linear polarization of 98%. Tawara *et al.* [20] also found a high β value of 10^{-2} in the nitride VCSEL with two dielectric mirrors. Honda *et al.* reported the estimation of high characteristics temperature of GaN-based VCSEL [31]. These all mean the development of nitride-based VCSEL and the understanding of the laser performance has become more and more important. Especially, the current-injected nitride-based VCSEL still can't be realized, therefore, more efforts on it are necessary and crucial for high performance future application.

1-2.3 Two-dimensional (2-D) photonic crystal lasers

Besides VCSEL, a novel structure, photonic crystal (PC) laser, was demonstrated to be a new type of the vertical emitting laser after 1990s. It is featured by a periodic structure called photonic crystal. According to the theory, the light in the photonic crystal structure would be forbidden or only allowed in specific modes, and those modes could be plotted as a photonic band diagram as shown in figure 1. 5. Consequently, such structures can act not only as a

passive waveguide or resonator to direct the wave propagation but also as an active medium to control light emission [32]. For fabricating laser devices, there are two kinds of 2-D PC lasers to be reported in these few years. One is 2-D PC nano-cavity laser, and another is 2-D PC band-edge laser.

I. 2-D PC Nano-Cavity Lasers

In 1994, P. R. Berman *et al.* first presented that photonic crystal could be a reflective mirror around the cavity of a laser [33]. Then, in 1999 O. Painter practically demonstrated an optically pumped InGaAs-based 2-D PC nano-cavity laser emitting 1.55 micrometers (as shown in figure 1.6.1) [34]. The optical cavity he demonstrated consisted of a half-wavelength-thick waveguide for vertical confinement and a 2-D PC mirror for lateral localization. A defect was introduced as a nano-cavity (a volume of 2.5 cubic half-wavelength, approximately 0.03 cubic micrometers) in the 2-D PC to trap photons inside. In 2004, Hong-Gyu Park *et al.* realized the electrically driven single-cell 2D-PC laser (λ=1519.7 nm) [35]. They used a sub-micrometer-sized semiconductor post placed below the center of the single-cell photonic crystal resonator to connect bottom electrode and achieved lasing action via current injection.

In 2005, nitride-based blue (about 488nm) photonic crystal membrane nano-cavity with Q factor about 800 was also reported by Y. S. Choi *et al.* [36]. They used photo-enhanced chemical etching to form a GaN membrane with a total thickness of 140 nm and patterned a photonic crystal cavity on it. Some resonance modes from the nano-cavities with lattice constant 180 nm could be observed in the photoluminescence (PL) emission.

II. 2-D PC Band-edge lasers

Compared to 2-D PC nano-cavity lasers, it is not necessary to create a defect in the 2-D photonic crystal to be a nano-cavity for a 2-D PC band-edge laser. That is, the 2-D photonic band-edge laser is composed of a perfect photonic crystal structure. Then, by satisfying Bragg condition, the laser action would happen in those band edge points in the photonic band

diagram. In 1999, Noda *et al.* reported the electrically driven 2-D PC band-edge laser under pulsed operation [37]. The PC was a triangular-lattice structure composed of InP and air holes, which is integrated with an InGaAsP/InP multiple-quantum-well active layer by a wafer fusion technique. They demonstrated the single-mode, large-area and surface-emitting lasing action, and analyzed the lasing mechanism based on the satisfying of Bragg condition. Then, they further reported the room-temperature (RT) 2-D PC band-edge laser under continuous wave (CW) operation in 2004 [38]. This opens a new road toward the large-area single-mode surface emitting laser.

1-3 Objectives of this thesis

From the view of superior laser devices, the single mode, large area, high output-power, and surface emitting have become basic requirements for the future laser device. In this thesis, we mainly focus on the study of nitride-based surface emitting lasers including the vertical-cavity surface emitting laser and 2-D PC surface emitting laser. The study of nitride-based VCSELs consists of the design, fabrication, and characteristics of the laser. We discuss and analyze the performance of nitride-based VCSEL such as threshold characteristics, laser spectrum, polarization, divergence angle, characteristic temperature, and coupling efficiency of spontaneous emission. Furthermore, unique lasing phenomenon, such as specific mode behavior and multiple-spot lasing, of the nitride-based VCSEL resulting from the inhomogeneity of gain and quality factor in the structure are also investigated. We also establish the fabrication processes of nitride-based vertical-cavity surface emitting devices and put the VCSEL structure into the processes to get a high-quality surface emitting device. Besides, we develop the other surface emitting laser, 2-D PC surface emitting laser, using the epitaxial part of our nitride-based VCSEL, i. e. the structure with a nitride cavity and a nitride bottom reflector. The fabrication and characteristics of the nitride-based 2-D PC surface emitting laser are also demonstrated and investigated.

References

1. S. Nakamura, M. Senoh, N. Iwasa, and S. Nagahama, *Jpn. J. Appl.Phys.*, **34**, L797 (1995)
2. S. Nakamura, T. Mukai, and M. Senoh, *Appl. Phys. Lett.*,**64**, 1687 (1994)
3. S. Nakamura, M. Senoh, S.Nagahama, N.Iwasa, T. Yamada, T. Matsushita, Y. Sugimoto, and H.Kiyoku, *Appl. Phys. Lett.*, **70**, 868 (1997)
4. S. Nakamura, *Science*, **281**, 956 (1998)
5. Y. Arakawa, *IEEE J. Select. Topics Quantum Electron.*, **8**, 823 (2002)
6. H. Morkoc, *Nitride Semiconductors and Devices (Spring Verlag, Heidelberg)* (1999)
7. S. N. Mohammad, and H. Morkoc, *Progress in Quantum Electron.*, **20**, 361 (1996)
8. J. I. Pankove, E. A. Miller, J. E. Berkeyheier, *J. Luminescence*, **5**, 84 (1972)
9. H. P. Maraska, D. A. Stevenson, J. I. Pankove, *Appl. Phys. Lett.*, **22**, 303 (1973)
10. J. I. Pankove, *Phys. Rev. Lett.*, **34**, 809 (1975).
11. M. Takeya, T. Tojyo, T. Asano, S. Ikeda, T. Mizuno, O. Matsumoto, S. Goto, Y. Yabuki, S. Uchida, and M. Ikeda, *phys. stat. sol. (a)*, **192**, 269 (2002)
12. S. Nakamura, M. Senoh, S. Nagahama, N. Iwasa, T.Yamada, T. Matsushita, H. Kiyoku, Y. Sugimoto, T. Kozaki, H. Umemoto, M. Sano, and K. Chocho, *Appl. Phys. Lett.*, **72,** 211 (1998)
13. S. Nakamura, *IEEE J. Select. Topics Quantum Electron.*, **4**, 483 (1998)
14. M. C. Schmidt, K. C. Kim, R, M. Farrell, D. F. Feezell, D. A. Cohen, M. Saito, K. Fujito, J. S. Speck, S. P. Denbaars, and S. Nakamura, *Jpn. J. Appl. Phys*, **46**, L190 (2007)
15. D. F. Feezell, M. C. Schmidt, Robert M. Farrell, K. C. Kim, M. Saito, K. Fujito, D. A. Cohen, J. S. Speck, S. P. Denbaars, and S. Nakamura, *Jpn. J. Appl. Phys*, **46**, L284 (2007)
16. K. Iga, *IEEE J. Quantum Electron.*, **24**, 1845 (1988)
17. K.Iga, *Proceedings of the First International Symposium on blue lasers and light emitting diodes*, Th-11 (1996)
18. T. Someya, R.Werner, A. Forchel, M. Catalano, R. Cingolani, Y.Arakawa, Science, **285**,

1905 (1999)

19. Y.-K. Song, H. Zhou, M. Diagne, A. V. Nurmikko, R. P. Schneider, Jr., C. P. Kuo, M. R. Krames, R. S. Kern, C. Carter-Coman, and F. A. Kish, *Appl. Phys. Lett.*, **76**, 1662 (2000)
20. T. Tawara, H. Gotoh, T. Akasaka, N. Kobayashi, and T. Saitoh, *Appl. Phys. Lett*., **83**, 830 (2003)
21. H. Zhou, M. Diagne, E. Makarona, A. V. Nurmikko, J. Han, K. E. Waldrip and J. J. Figiel, *Electron. Lett.*, **36**,1777 (2000)
22. J.T. Chu *et. al.*, *Jpn. J. Appl. Phys*, **45**, 2556 (2006).
23. J. T. Chu *et. al.*, *Appl. Phys. Lett.*, **89**, 121112 (2006).
24. C. C. Kao *et. al.*, *Appl. Phys. Lett.*, **87**, 081105-1 (2005).
25. C. C. Kao *et. al.*, *IEEE Photon. Technol. lett*., **18**, 877 (2006).
26. J. F. Carlin, J. Dorsaz, E. Feltin, R. Butté, N. Grandjean, M. Ilegems, and M. Laügt, *Appl. Phys. Lett.*, **86**, 031107 (2005)
27. E. Feltin, R. Butté, J. F. Carlin, J. Dorsaz, N. Grandjean, and M. Ilegems, *Electron. Lett.*, **41**, 94 (2005)
28. T. Ive, O. Brandt, H. Kostial, T. Hesjedal, M. Ramsteiner, and K. H. Ploog, *Appl. Phys. Lett*., **85**, 1970 (2004)
29. H.H. Yao, C.F. Lin, H.C. Kuo, S.C. Wang, *J. Crystal Growth,* **262**, 151 (2004)
30. S. Kako, T. Someya, and Y. Arakawa, *Appl. Phys. Lett.*, **80**, 722 (2002)
31. T. Honda, H. Kawanishi, T. Sakaguchi, F. Koyama and K. Iga, *MRS Internet J. Nitride Semicond.* **4S1**, G6.2-1 (1999).
32. C. M. Lai, H. M. Wu, P. C. Huang, S. L. Peng, *Appl. Phys. Lett.*, **90**, 141106, (2007)
33. P. R. Berman, New York:Academic, (1994)
34. O. Painter, R. K. Lee, A. Scherer, A. Yariv, J. D. O`Brien, P. D. Dapkus, I. Kim, *Science*, **284**, 1819, (1999)
35. H. G. Park, S. H. Kim, S. H. Kwon, Y. G. Ju, J. K. Yang, J. H. Baek, S. B. Kim, Y. H. Lee,

Science, **305**, 1444, (2005)

36. Y. S. Choi, K. Hennessy, R. Sharma, E. Haberer, Y. Gao, S. P. DenBaars, C. Meier, *Appl. Phys. Lett.*, **87**, 243101, (2005)
37. M. Imada, S. Node, A. Chutinan. and T. Tokuda, *Appl. Phys. Lett.*, **75**, 316, (1999)
38. D. Ohnishi, T. Okano, M. Imada, and S. Node, *Opt. Exp.,* **12**, 1562, (2004)

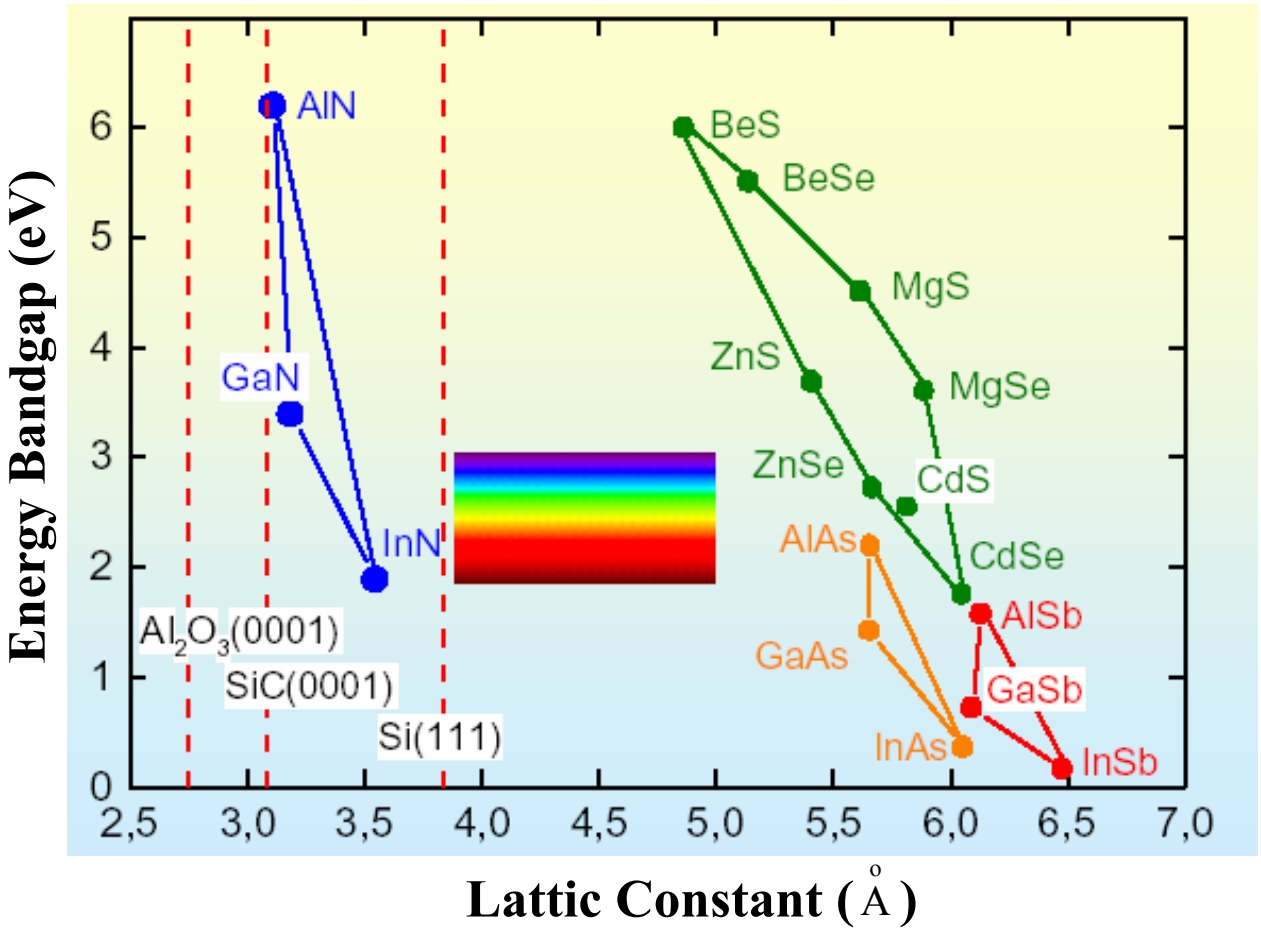

Figure 1.1 The band-gap diagram of II-VI and III-V semiconductor materials.

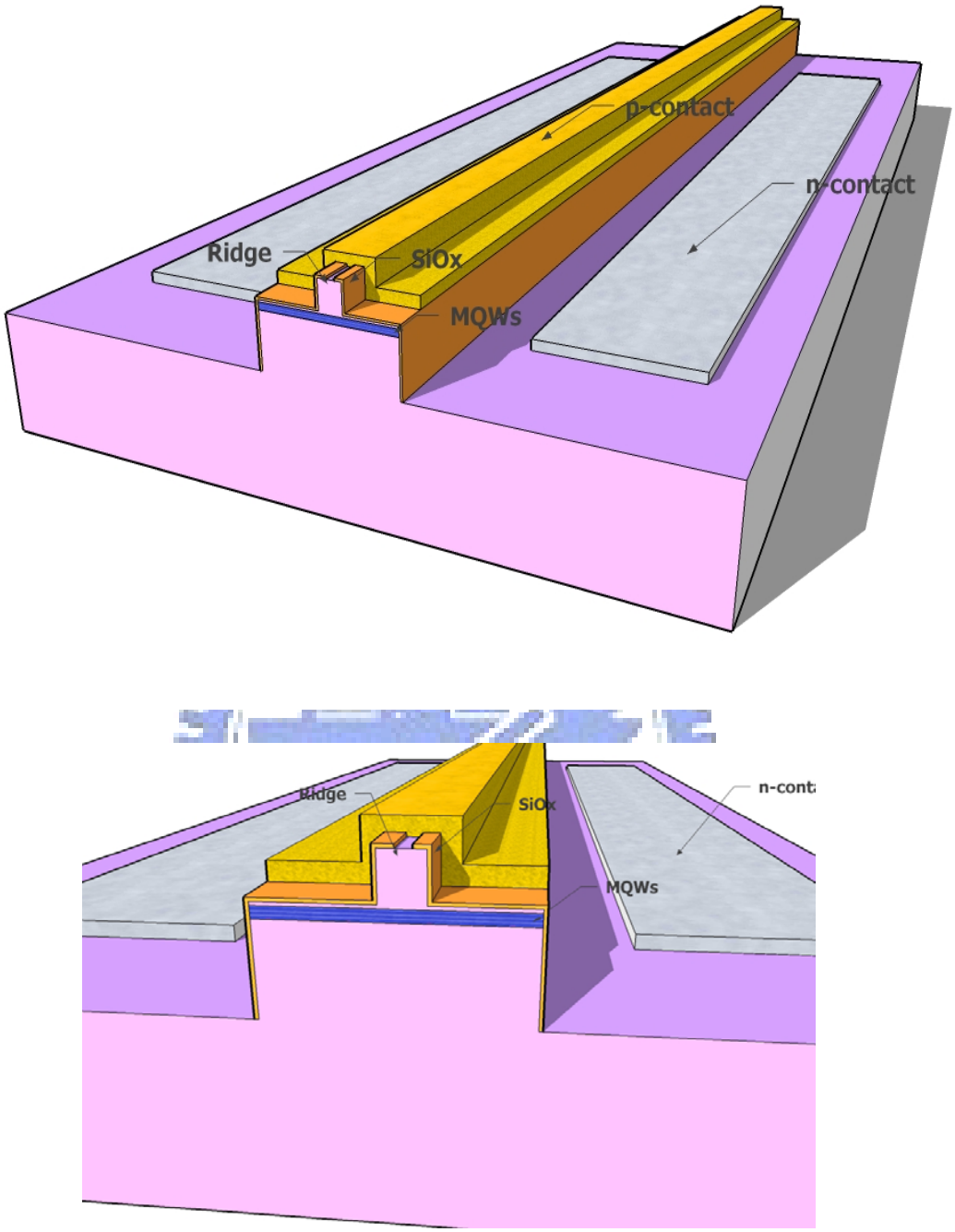

Figure 1.2 The schematic diagram of an edge emitting laser diode.

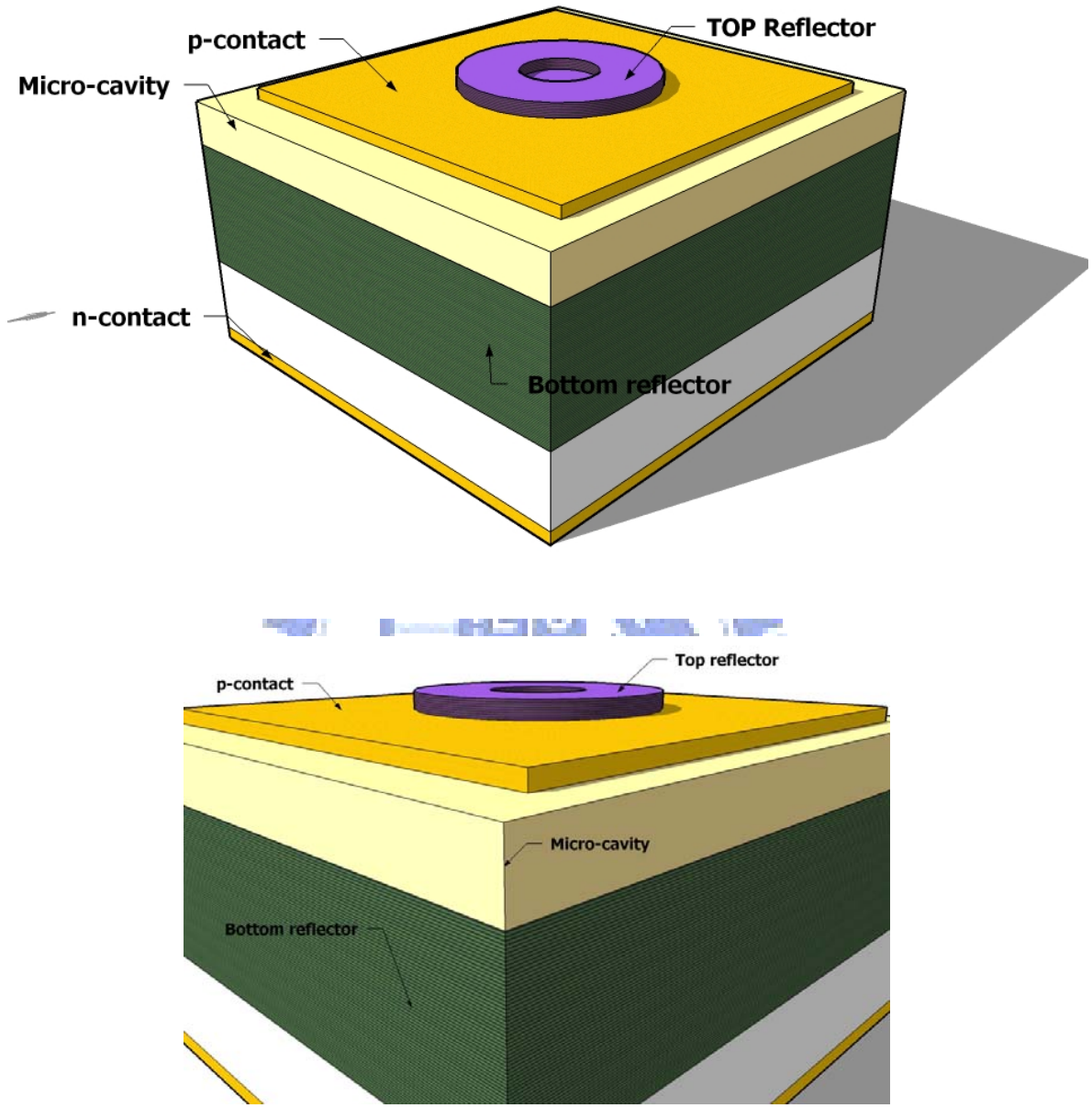

Figure 1.3 The schematic diagram of a vertical-cavity emitting laser diode.

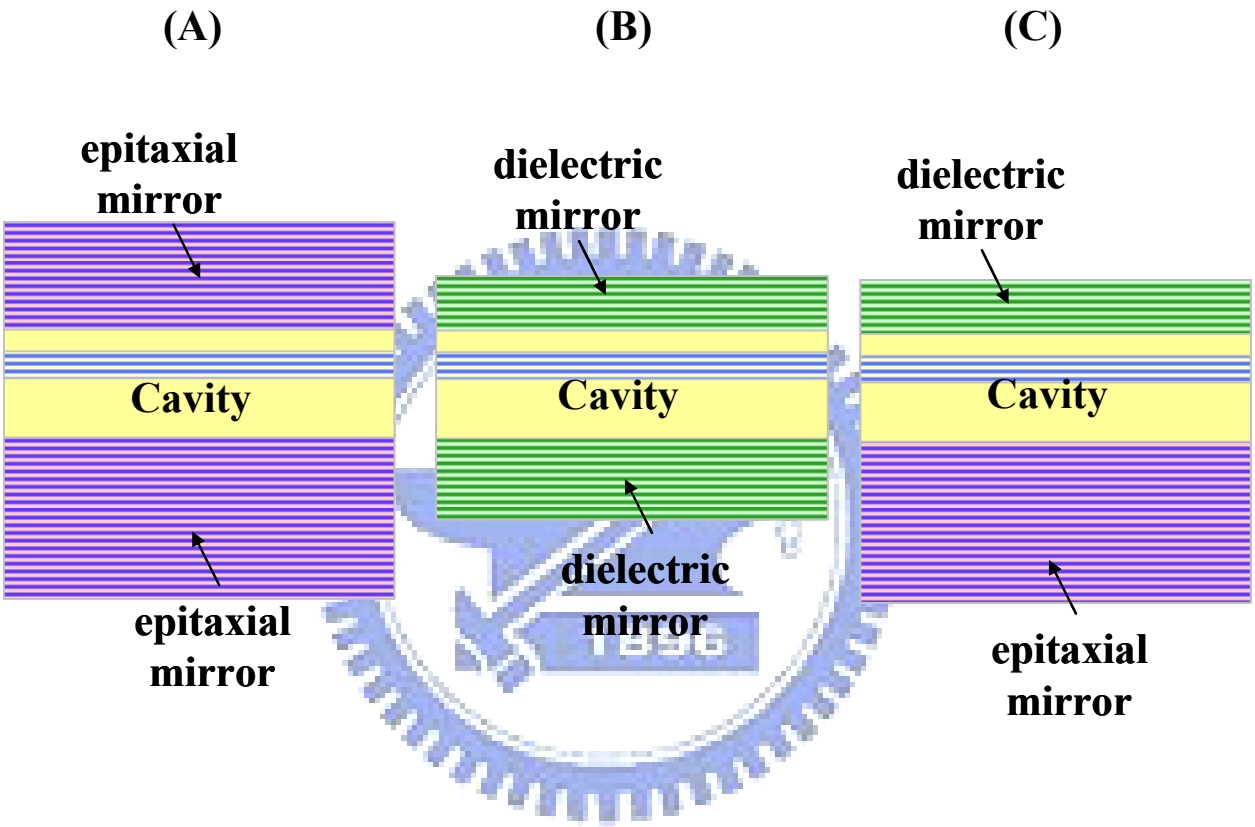

Figure 1.4 Schematic diagrams of three nitride-based VCSEL structures.

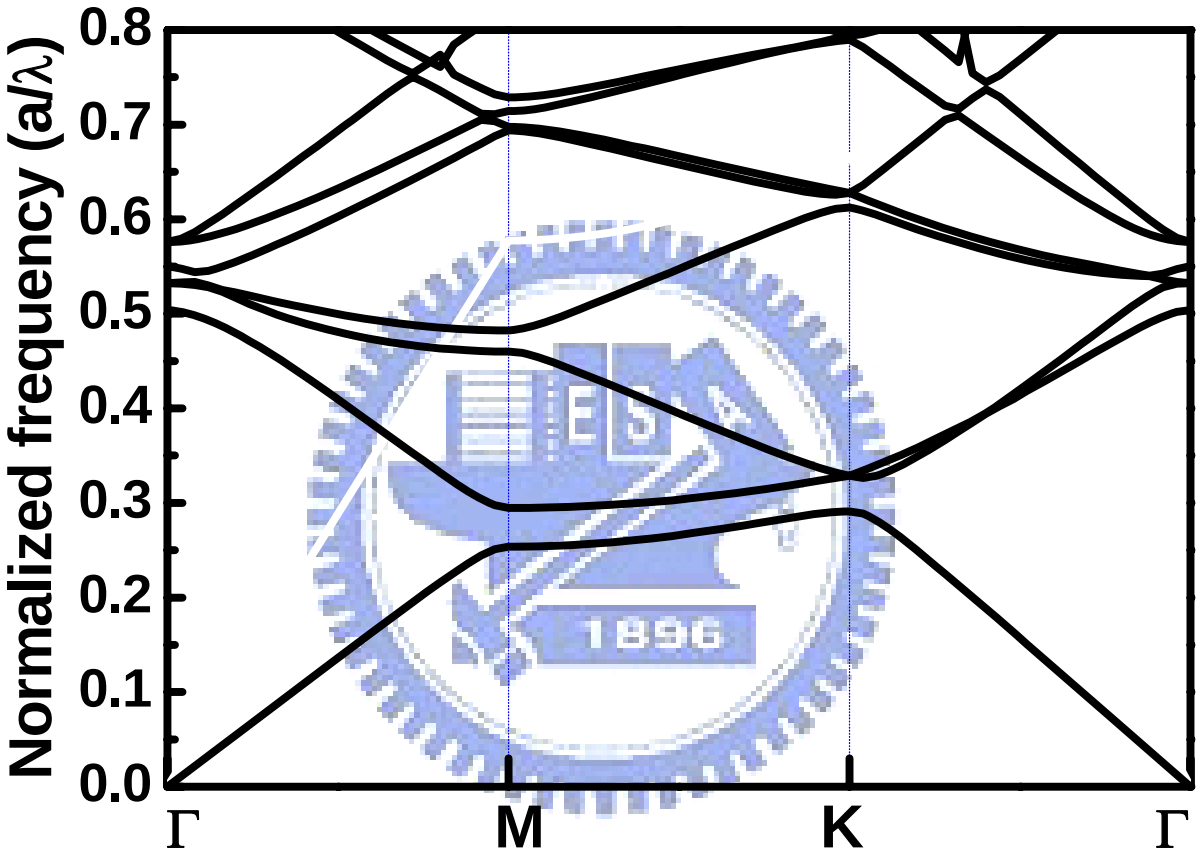

Figure 1.5 The band diagram of a 2-D triangular-lattice PC structure.

Chapter 2

Fundamentals of Micro-Cavity Surface Emitting Lasers

2-1 Operation Mechanism of Semiconductor Lasers [1-7]

Carrier density rate equation

For the DH active region, the injected current provides a generation term, and various radiative and nonradiative recombination process as well as carrier leakage provide recombination terms. Thus, we can write the carrier density rate equation,

$$\frac{dN}{dt} = G_{gen} - R_{rec} \tag{2.01}$$

where N is the carrier density (electron density), G_{gen} is the rate of injected electrons and R_{rec} is the ratio of recombining electrons per init volume in the active region. Since there areη_i I/q electrons per second being injected into the active region, $G_{gen} = \frac{\eta_i I}{qV}$, where V is the volume of the active region. The recombination process is complicated and several mechanisms must be considered. Such as, spontaneous recombination rate, $R_{sp} \sim BN^2$, nonradiative recombination rate, R_{nr}, carrier leakage rate, R_l, ($R_{nr} + R_l = AN+CN^3$), and stimulated recombination rate, R_{st}. Thus we can write $R_{rec} = R_{sp} + R_{nr} + R_l + R_{st}$. Besides, $N/\tau \equiv R_{sp} + R_{nr} + R_l$, where τ is the carrier lifetime. Therefore, the carrier density rate equation could be expressed as

$$\frac{dN}{dt} = \frac{\eta_i I}{qV} - \frac{N}{\tau} - R_{st} \tag{2.02}$$

Photon density rate equation

Now, we describe a rate equation for the *photon density,* N_p, which includes the photon generation and loss terms. The photon generation process includes spontaneous recombination (R_{sp}) and stimulated recombination (R_{st}), and the main photon generation term of laser above

threshold is R_{st}. Every time an electron-hole pairs is stimulated to recombine, another photon is generated. Since, the cavity volume occupied by photons, V_p, is usually larger than the active region volume occupied by electrons, V, the photon density generation rate will be $[V/V_p]R_{st}$ not just R_{st}. This electron-photon overlap factor, V/V_p, is generally referred to as the *confinement factor*, Γ. Sometimes it is convenient to introduce an effective thickness (d_{eff}), width (w_{eff}), and length (L_{eff}) that contains the photons. That is, $V_p=d_{eff}w_{eff}L_{eff}$. Then, if the active region has dimensions, d, w, and L_a, the confinement factor can be expressed as, $\Gamma=\Gamma_x\Gamma_y\Gamma_z$, where$\Gamma_x = d/d_{eff}$, $\Gamma_y = w/w_{eff}$, $\Gamma_z = L_a/L_{eff}$. Photon loss occurs within the cavity due to optical absorption and scatting out of the mode, and it also occurs at the output coupling mirror where a portion of the resonant mode is usually couple to some output medium. These net losses can be characterized by a *photon (or cavity) lifetime*, τ_p. Hence, the photon density rate equation takes the form

$$\frac{dN_p}{dt} = \Gamma R_{st} + \Gamma\beta_{sp}R_{sp} - \frac{N_p}{\tau_p} \tag{2.03}$$

where β_{sp} is the *spontaneous emission factor*. As to R_{st}, it represents the photon-stimulated net electron-hole recombination which generates more photons. This is a gain process for photons. It is given by

$$\left(\frac{dN_p}{dt}\right)_{gen} = R_{st} = \frac{\Delta N_p}{\Delta t} = v_g g N_p \tag{2.04}$$

where v_g is the group velocity and g is the gain per unit length.

Now, we rewrite the carrier and photon density rate equations

$$\frac{dN}{dt} = \frac{\eta_i I}{qV} - \frac{N}{\tau} - v_g g N_p \tag{2.05}$$

$$\frac{dN_p}{dt} = \Gamma v_g g N_p + \Gamma\beta_{sp}R_{sp} - \frac{N_p}{\tau_p} \tag{2.06}$$

Threshold gain

In order for a mode of the laser to reach threshold, the gain in the active section must be increased to the point when all the propagation and mirror losses are compensated. Most laser cavities can be divided into two general sections: an active section of length L_a and a passive section of length L_p. For a laser, at the threshold, the gain is equal whole loss in the cavity, which includes cavity absorption and mirror loss. For convenience the mirror loss term is sometimes abbreviated as, $\alpha_m \equiv (1/2L)\ \ln(1/R_1R_2)$. Noting that the cavity life time (photon decay rate) is given by the optical loss in the cavity, $1/\tau_p = 1/\tau_i + 1/\tau_m = v_g(\alpha_i + \alpha_m)$. Thus, the threshold gain in the steady state can be expressed with following equation

$$\Gamma g_{th} = \alpha_i + \alpha_m = \frac{1}{v_g \tau_p} = \alpha_i + \frac{1}{2L} \ln\left(\frac{1}{R_1 R_2}\right) \tag{2.07}$$

where α_i is the average internal loss which is defined by $(\alpha_{ia}L_a + \alpha_{ip}L_p)/L$ (i.e.,$\alpha_{ia}L_a$ and $\alpha_{ip}L_p$ are loss of active region and passive section, respectively), and R_1 and R_2 is the reflectivity of top and bottom mirror of the laser cavity, respectively.

Output power versus driving current

The characteristic of output power versus driving current (L-I characteristic) in a laser diode can be realized by using the rate equation Eq. (2.05) and (2.06). Consider the below threshold (almost threshold) steady-state (dN/dt = 0) carrier rate equation, the Eq. (2.05) is given by $\frac{\eta_i I_{th}}{qV} = \frac{N_{th}}{\tau}$. While the driving current is above the threshold, the carrier rate equation will be

$$\frac{dN}{dt} = \eta_i \frac{(I - I_{th})}{qV} - v_g g N_p \tag{2.08}$$

From Eq. (2.08), the steady-state photon density above threshold where $g = g_{th}$ can be calculated as

$$N_p = \frac{\eta_i (I - I_{th})}{q v_g g_{th} V} \tag{2.09}$$

The optical energy stored in the cavity, E_{os}, is constructed by multiplying the photon density, N_p, by the energy per photon, $h\nu$, and the cavity volume, V_p. That is $E_{os} = N_p h\nu V_p$. Then, we multiple this by the energy loss rate through the mirrors, $v_g\alpha_m = 1/\tau_m$, to get the optical power output from the mirrors, $P_0 = v_g\alpha_m N_p h\nu V_p$. By using Eq. (2.07) and (2.09), and $\Gamma=V/V_p$, we can write the output power as the following equation

$$P_O = \eta_i \left(\frac{\alpha_m}{\alpha_i + \alpha_m} \right) \frac{h\nu}{q} (I - I_{th}) \tag{2.10}$$

Now, by defining $\eta_d = \frac{\eta_i \alpha_m}{\alpha_i \alpha_m}$, the Eq. (2.10) can be simplified as

$$P_O = \eta_d \frac{h\nu}{q} (I - I_{th}) \qquad (I > I_{th}) \tag{2.11}$$

Thus, the η_d can be expressed as

$$\eta_d = \left[\frac{q}{h\nu} \right] \frac{dP_O}{dI} \qquad (I > I_{th}) \tag{2.12}$$

In fact, η_d is the *differential quantum efficiency*, defined as number of photons out per electron. Besides, dP_o/dI is defined as the *slope efficiency*, S_d, equal to the ratio of output power and injection current. Figure 2.1 shows the illustration of output power vs. current for a diode laser. Below threshold only spontaneous emission is important; above threshold the stimulated emission power increase linearly with the injection current, while the spontaneous emission is clamped at its threshold value.

2-2 Penetration Depth of Distributed Bragg Reflectors [8-13]

Distributed Bragg reflectors (DBRs) served as high reflecting mirror in numerous optoelectronic and photonic devices such as VCSEL. It is a periodic structure formed by stacking several pairs of two 1/4-lamda-thick layers with different refractive index. Consider a distributed Bragg reflector consisting of m pairs of two dielectric, lossless materials with

high- and low- refractive index n_H and n_L, as shown in figure 2.2. The thickness of the two layers is assumed to be a quarter wave, that is, $L_1 = \lambda_B/4n_H$ and $L_2 = \lambda_B/4n_L$, where the λ_B is the Bragg wavelength.

Multiple reflections at the interface of the DBR and constructive interference of the multiple reflected waves increase the reflectivity with increasing number of pairs. The reflectivity has a maximum at the Bragg wavelength λ_B. The reflectivity of a DBR with m quarter wave pairs at the Bragg wavelength is given by

$$R = \left(\frac{1 - \frac{n_s}{n_o}\left(\frac{n_L}{n_H}\right)^{2p}}{1 + \frac{n_s}{n_o}\left(\frac{n_L}{n_H}\right)^{2p}} \right) \tag{2.13}$$

where the n_o and n_s are the refractive index of incident medium and substrate.

The high-reflectivity or stop band of a DBR depends on the difference in refractive index of the two constituent materials, $\triangle n$ (n_H-n_L). The spectral width of the stop band is given by

$$\Delta\lambda_{stopband} = \frac{2\lambda_B \Delta n}{\pi n_{eff}} \tag{2.14}$$

where n_{eff} is the effective refractive index of the mirror. It can be calculated by requiring the same optical path length normal to the layers for the DBR and the effective medium. The effective refractive index is then given by

$$n_{eff} = 2\left(\frac{1}{n_H} + \frac{1}{n_L}\right)^{-1} \tag{2.15}$$

The length of a cavity consisting of two metal mirrors is the physical distance between the two mirrors. For DBRs, the optical wave penetrates into the reflector by one or several quarter-wave pairs. Only a finite number out of the total number of quarter-wave pairs are effective in reflecting the optical wave. The effective number of pairs seen by the wave electric field is given by

$$m_{eff} \approx \frac{1}{2}\frac{n_H + n_L}{n_H - n_L 21}\tanh\left(2m\frac{n_H - n_L}{n_H + n_L}\right) \tag{2.16}$$

For very thick DBRs (m→∞) the tanh function approaches unity and one obtains

$$m_{eff} \approx \frac{1}{2}\frac{n_H + n_L}{n_H - n_L} \tag{2.17}$$

Also, the penetration depth is given by

$$L_{pen} = \frac{L_1 + L_2}{4r}\tanh(2mr) \tag{2.18}$$

where $r = (n_1-n_2)/(n_1+n_2)$ is the amplitude reflection coefficient.

For a large number of pairs (m→∞), the penetration depth is given by

$$L_{pen} \approx \frac{L_1 + L_2}{4r} = \frac{L_1 + L_2}{4}\frac{n_H + n_L}{n_H - n_L} \tag{2.19}$$

Comparison of Eqs. (2.17) and (2.19) yields that

$$L_{pen} = \frac{1}{2}m_{eff}(L_1 + L_2) \tag{2.20}$$

The factor of (1/2) in Eq. (2.20) is due to the fact that m_{eff} applies to effective number of periods seen by the electric field whereas L_{pen} applies to the optical power. The optical power is equal to the square of the electric field. The effective length of a cavity consisting of two DBRs is thus given by the sum of the thickness of the center region plus the two penetration depths into the DBRs.

2-3 Coupling Efficiency of Spontaneous Emission into a Lasing Mode [14]

In a conventional semiconductor laser, only a very small part of the spontaneous emission is coupled into a single-lasing mode. That is because the radiation pattern of spontaneous emission is isotropic, a substantial part of the spontaneous emission is not coupled to the guided modes in an active waveguide with a small acceptance angle. Furthermore, the spontaneous emission spectral linewidth is broader than the linewith of the

longitudinal mode; therefore, a substantial part of the spontaneous emission is not coupled to a lasing mode. That is, the coupling efficiency of spontaneous emission (β) usually is considerably small for typical laser diodes.

Suppose an active volume V of semiconductor laser, which is much larger than thecubic of optical length, is enclosed by "perfect reflector". The number of modes per unit frequency interval is given by $8\pi v^2 V\varepsilon^{3/2}/c^3$. If we assume the active dipoles are distributed uniformly in the volume V and are randomly oriented, the coupling efficiency of spontaneous emission into each mode is identical. The total spontaneous emission rate is given by

$$R_{sp} \equiv N_c\gamma = \int \frac{8\pi v^2 V\varepsilon^{3/2}}{c^3}|g|^2 \frac{2\Gamma N_c}{4\pi^2(v-v_0)^2+\Gamma^2}dv = \frac{8\pi v^2 V\varepsilon^{3/2}|g|^2 N_c}{c^3} \qquad (2.21)$$

Here $|g|^2$ is the electric dipole coupling constant and a Lorentzian line shape is assumed, 2Γ is the spontaneous emission linewidth in rad/s (FWHM), γ is the spontaneous decay rate, and N_c is total minority-carrier number. If the lasing frequency is coincident with gain center $v = v_0$, the spontaneous emission rate E_{cv} into one lasing mode is

$$E_{cv} = \frac{2|g|^2 N_c}{\Gamma} \qquad (2.22)$$

From Eqs. (2.21) and (2.22), the coupling efficiency β of spontaneous emission into the lasing mode (spontaneous emission coefficient) is calculated as [15]

$$\beta \equiv \frac{E_{cv}}{R_{sp}} = \frac{c^3}{4\pi v^2\varepsilon^{3/2}V\Gamma} = \frac{\lambda^4}{4\pi^2 V\Delta\lambda\varepsilon^{3/2}} \approx 0.025\frac{\lambda^4}{\varepsilon^{3/2}\Delta\lambda V} \qquad (2.23)$$

Here $\Delta\lambda = \lambda^2\Gamma/c\pi$ is the spontaneous emission linewidth in meters (FWHM). If we use the numerical parameters of a typical GaN semiconductor laser, assuming $\lambda = 4\times10^{-7}$ m, $\varepsilon^{1/2} = 2.5$, $\Delta\lambda = 2\times10^{-8}$ m, and $V = 10^{-15}$ m^3, the spontaneous emission coefficient β is on the order of 10^{-5}. This means that only one photon of 10^5 spontaneously emitted photons could couple into a lasing mode.

Besides equation Eq. (2.23), β also could be written as [16]:

$$\beta = F_p /(1+F_p)$$
$$F_p = \frac{3}{4\pi^2}\frac{Q}{V_c /(\lambda/\bar{n})^3} \tag{2.24}$$

where F_p is the Purcell factor, Q is the cavity quality factor, λ is the wavelength of laser mode, V_c is the effective optical volume of the laser mode, and $\bar{n}$ is the refractive index.

2-4 Characteristics of Microcavity Semiconductor Lasers [14]

As discussed already, the coupling efficiency of spontaneous emission into a lasing mode can be increased to a value close to 1 for a microcavity semiconductor laser from 10^{-5} for a conventional semiconductor laser. The characteristics of such a microcavity semiconductor laser would be very different from a conventional semiconductor laser.

The quantum Langevin equation for the (total) electron number operator $\hat{N}_c$ is written as [17]

$$\frac{d}{dt}\hat{N}_c = P - \left[\frac{1-\beta}{\tau_{sp}} + \frac{\beta}{\tau_{sp}}\right]\hat{N}c - (\hat{E}_{cv} - \hat{E}_{vc})\hat{n} + \hat{\Gamma}_p + \hat{\Gamma}_{sp} + \hat{\Gamma}, \tag{2.25}$$

where P is the pump rate, $\beta < \hat{N}_c > / \tau_{sp}$ is the spontaneous emission rate into a lasing mode, $(1-\beta) < \hat{N}_c > / \tau_{sp}$ is the spontaneous emission rate into all other modes except the lasing mode, $< \hat{E}_{cv} >$ and $< \hat{E}_{vc} >$ are the stimulated emission and absorption rates per photon, $(< \hat{E}_{cv} > - < \hat{E}_{vc} >)$ is a population inversion parameter, $\hat{n}$ is the (total) photon number operator, $\hat{\Gamma}_p$, $\hat{\Gamma}_{sp}$, and $\hat{\Gamma}$ are the noise operators associated with the pump process, the spontaneous emission process and stimulated emission or absorption process.

The spontaneous emission rate into the lasing mode and the stimulated emission rate per photon should be equal by the Einstein's relation, so that we have

$$\frac{\beta}{\tau_{sp}} < \hat{N}_c >=< \hat{E}_{cv} > \tag{2.26}$$

The quantum Langevin equations for (total) photon number operator $\hat{n}$ is written as

$$\frac{d}{dt}\hat{n} = -\left[\frac{\omega}{Q} - (\hat{E}_{cv} - \hat{E}_{vc})\right]\hat{n} + \frac{\beta}{\tau_{sp}}\hat{N}_c + \hat{F} + \hat{F}_e \tag{2.27}$$

where ω/Q is the photon decay rate, $\hat{F}$, and $\hat{F}_e$ are the noise operators associated with the stimulated emission processes, and the photon decay process.

Let us consider the steady-state (average) solutions of Eqs. (2.25) and (2.27). Using the linearized solutions, $\hat{N}_c = N_{c0} + \Delta\hat{N}_c$ and $\hat{n} = n_0 + \Delta\hat{n}$, in Eqs. (2.25) and (2.27), we obtain

$$P - \frac{N_{c0}}{\tau_{sp}} - \frac{\beta}{\tau_{sp} n_{sp}} n_0 = 0 \tag{2.28}$$

$$-\left[\frac{\omega}{Q} - \frac{\beta N_{c0}}{\tau_{sp} n_{sp}}\right] n_0 + \frac{\beta N_{c0}}{\tau_{sp}} = 0 \tag{2.29}$$

At pump rates above the threshold, the photon decay rate ω/Q is equal to the net gain $\hat{E}_{cv} - \hat{E}_{vc}$ (i.e., the stimulated emission gain-stimulated absorption loss). Thus,

$$\frac{\omega}{Q} = \frac{\beta N_{c0,th}}{\tau_{sp} n_{sp}} \tag{2.30}$$

Where $N_{c0,th}$ is the threshold (total) electron number, which is approached by real electron number N_{c0} only when the pump rate is well above the threshold.

At the threshold pump rate, all the pump electrons recombine via spontaneous emission ($P_{th} = N_{c0,th}/\tau_{sp}$). The stimulated emission rate E_{cv} by one photon is equal to the spontaneous emission so that

$$E_{cv} = \beta P_{th} \tag{2.31}$$

From Eq. (2.30), the threshold pump rate can be calculated as

$$P_{th} = \frac{N_{c0,th}}{\tau_{sp}} = \frac{(\omega/Q)n_{sp}}{\beta} \tag{2.32}$$

This is an important result suggests that the threshold pump rate can be decreased by increasing β.

From Eq. (2.29), the average photon number n_0 is

$$n_0 = \frac{\beta N_{c0}/\tau_{sp}}{\omega/Q - \beta N_{c0}/\tau_{sp} n_{sp}} \tag{2.33}$$

It is obvious from this equation that the real electron number N_{c0} never reaches the threshold value $N_{c0,th}$ as long as the spontaneous emission coefficient β is nonzero. From Eq. (2.29), the average electron number N_{c0} is given by

$$N_{c0} = \begin{cases} N_{c0,th}\dfrac{(r+1)-[(r+1)^2-4(1-\beta)r]^{1/2}}{2(1-\beta)}, & \beta \neq 1 \\ N_{c0,th}\dfrac{r}{1+r}, & \beta = 1 \end{cases} \tag{2.34}$$

where $r = P/P_{th}$ is the normalized pump rate and $N_{c0,th} = \omega\tau_{sp} n_{sp}/Q\beta$. Using Eq. (2.33) in Eq. (2.34), the average photon number n_0 is

$$n_0 = \begin{cases} n_{sp}\dfrac{(r+1)-[(r+1)^2-4(1-\beta)r]^{1/2}}{2(1-\beta)} \Big/ \left[1 - \dfrac{(r+1)-[(r+1)^2-4(1-\beta)r]^{1/2}}{2(1-\beta)}\right], & \beta \neq 1 \\ n_{sp} r, & \beta = 1 \end{cases} \tag{2.35}$$

If the photon number n_0 is larger than one before the carrier density exceeds a transparency point, the stimulated emission rate into the lasing mode, even though the net gain is still negative. The threshold condition Eq. (2.32) holds when the photon number n_0 is much smaller than one at the transparency point. Figure 2.3 shows the internal photon number n_0 versus the pump rate P as a function of the spontaneous emission coefficient β, assuming that $n_{sp} = 1$ and βP_{th} is the same for each curve with different β value. It is clear the jump of photon nember at near threshold is smaller and smaller as the value of β is larger. As the

β=1, the increase of photon number with the increasing of pump rate becomes a linear increasing.

2-5 Band Edge Laser in a 2-D Triangular-Lattice Photonic Crystal [18, 19]

Figure 2.4(A) shows a band diagram of a triangular-lattice photonic crystal. The points I, II, and III are the points Γ_1, M_1, and K_1, respectively. The reciprocal space of the structure is a space combined by hexagons. Figure 2.4(B) shows a schematic diagram of a reciprocal space. The $\mathbf{K_1}$ and $\mathbf{K_2}$ are the Bragg vectors with the same magnitude, $|K|=2\pi/a$, where a is the lattice constant of the photonic crystal. Consider the TE modes in the 2-D photonic crystal structure, the diffracted light wave from the structure must satisfy the relationship:

$$k_d = k_i + q_1 K_1 + q_2 K_2, \qquad q_{1,2} = 0, \pm 1, \pm 2, \ldots \tag{2.21}$$

$$\omega_d = \omega_i \tag{2.22}$$

where k_d is xy-component wave vector of diffracted light wave, k_i is xy-component wave vector of incident light wave, $q_{1,2}$ is order of coupling, ω_d is the frequency of diffracted light wave, and ω_i is the frequency of incident light wave.

It is expected lasing occurs at specific points on the Brillouin-zone boundary (Γ, M, and K) and at the points at which bands cross and split. At these lasing points, waves propagating in different directions couple to significantly increase the mode density. It is particularly interesting that each of these points exhibits a different type of wave coupling. For example, as shown in figure 2.5(A), the coupling at point I only involves two waves, propagating in the forward and backward directions. This coupling is similar to that of a conventional DFB laser. However, there can be six equivalent Γ-M directions in the structure; that is, the cavity can exist independently in each of the three different directions to form three independent lasers. Point II has a unique coupling characteristic unachievable in conventional DFB lasers, the coupling of waves propagating in three different directions as shown in figure 2.5(B). This

means the cavity is a triangular. In fact, there can also be six Γ-K directions in the structure; therefore, two different lasing cavities in different Γ-K directions coexist independently. At point III the coupling includes waves in in-plane all six directions; 0°, 60°, 120°, -60°, -120°, and 180° as shown in figure 2.5(C). In addition, the coupled light can be emitted perpendicular from the surface according to first order Bragg diffraction, as shown in figure 2.6. This is the same phenomenon that occurs in conventional grating-coupled surface-emitting lasers.

References

1. H. E. Li and K. Iga, Vertical-Cavity Surface –Emitting Laser Devices, *Springer-Verlag, Berlin*, (2003)
2. C. W. Wilmsen, H. Temkin, L. A. Coldren, Vertical-Cavity Surface-Emitting Lasers, *Cambridge University Press* (1999)
3. J. Cheng and N. K. Dutta, Vertical-Cavity Surface-Emitting Lasers: Technology and Applications, *Gordon and Breach Science Publishers* (2000)
4. K. Iga and S. Kinoshita, Process Technology for Semiconductor Lasers, *Springer-Verlag, Berlin*, (1996)
5. L. A. Coldren and S. W. Corzine, Diode Lasers and Photonic Integrated Circuits, *John Wiley & Sons, Inc* (1995)
6. W. W. Chow and S. W. Koch, Semiconductor-Laser Fundamentals, *Springer-Verlag, Berlin*, (1999)
7. S. L. Chuang, Physics of Optoelectronic Devices, *John Wiley & Sons, Inc* (1995)
8. H. E. Li and K. Iga, Vertical-Cavity Surface –Emitting Laser Devices, *Springer-Verlag, Berlin*, (2003)
9. C. W. Wilmsen, H. Temkin, L. A. Coldren, Vertical-Cavity Surface-Emitting Lasers, *Cambridge University Press* (1999)
10. D. I. Babic and S. W. Corzine, *IEEE J. Quantum Electron.*, 28, 514 (1992)
11. H. Benisty, H. D. Neve, and C. Weisbuch, *IEEE J. Quantum Electron.*, 34, 1612 (1998)
12. H. Benisty, H. D. Neve, and C. Weisbuch, *IEEE J. Quantum Electron.*, 34, 1632 (1998)
13. D. Delbeke, R. Bockstaele, P. Bienstman, R. Baets, and H. Benisty, *J. Select. Topics Quantum Electron.*, 8, 189 (2002)
14. Y. Yamamoto, S. Machida, and G. Bj*o*rk, *Phys. Rev. A*, **44**, 657 (1991)
15. Y. Suematsu and K. Furuya, *Trans Inst. Electron. Commun. Eng. Jpn.*, **E-60**, 467 (1969)
16. S. Kako, T. Someya, and Y. Arakawa, *Appl. Phys. Lett.*, **80**, 722 (2002)

17. H. Haug, *Phys. Rev.*, **184**, 338 (1969)

18. M. Imada, A. Chutinan, S. Noda, M. Mochizuki, *Phy. Rev. B*, 65, 195306 (2002)

19. M. Notomi, H. Suzuki, and T. Tamamura, *Appl. Phys. Lett.*, **78**, 1325 (2001)

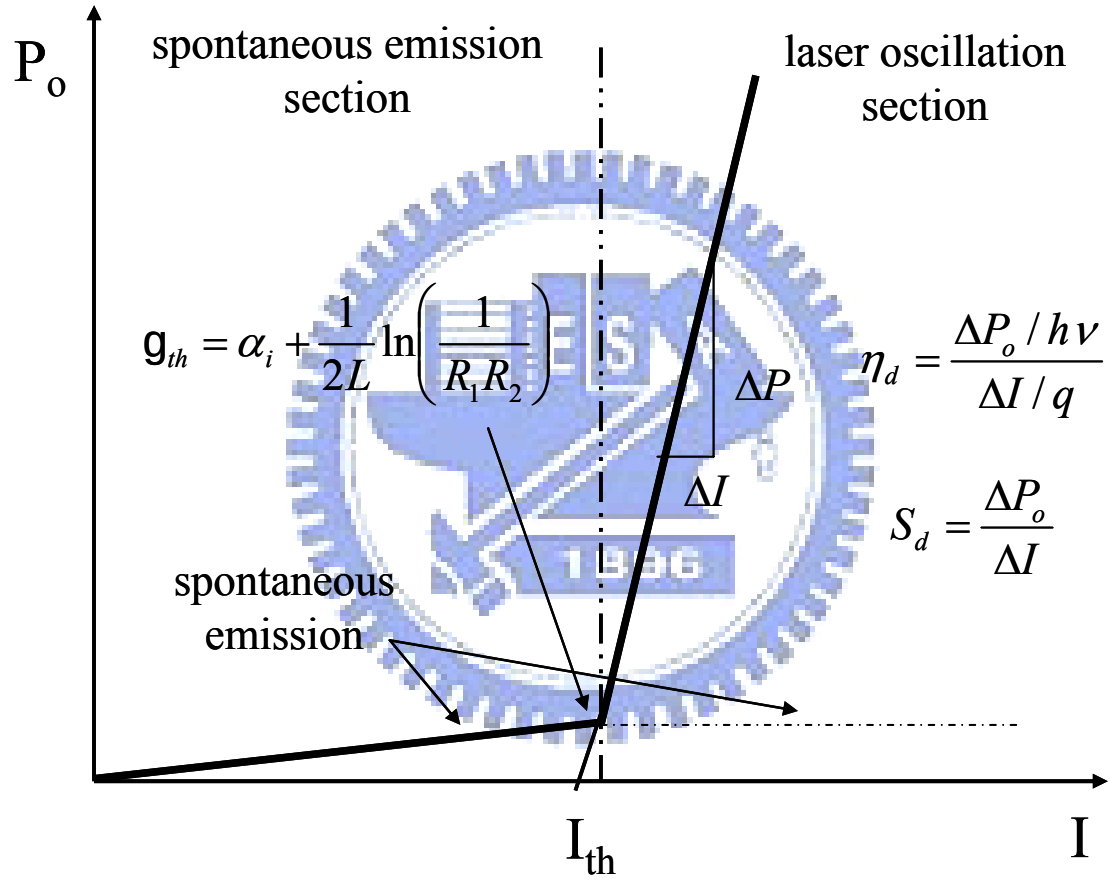

Figure 2.1 An illustration of output power vs. current for a diode laser.

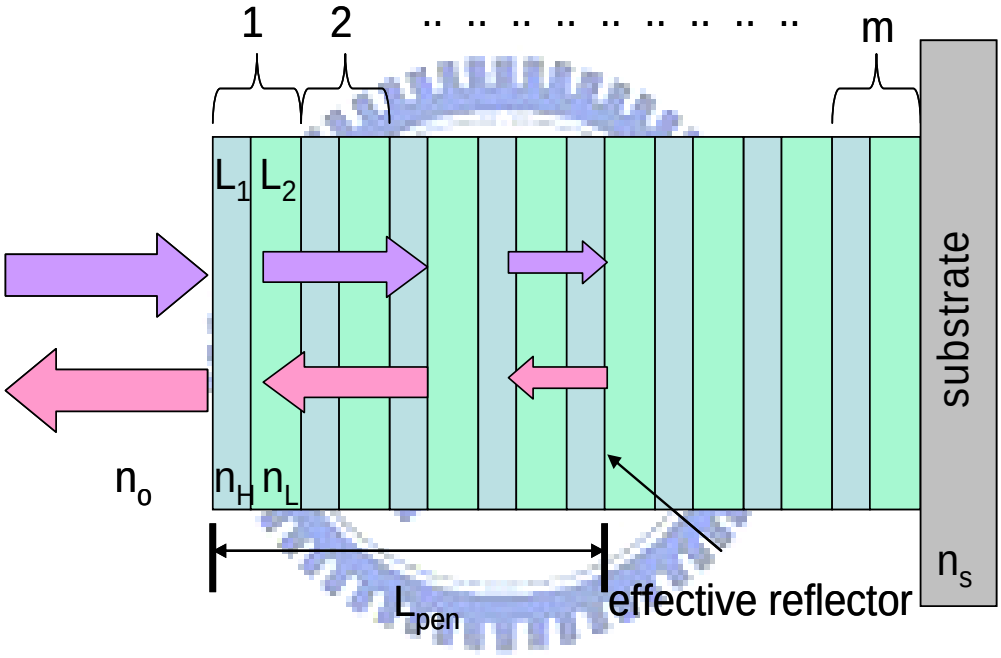

Figure 2.2 A schematic diagram of DBRs.

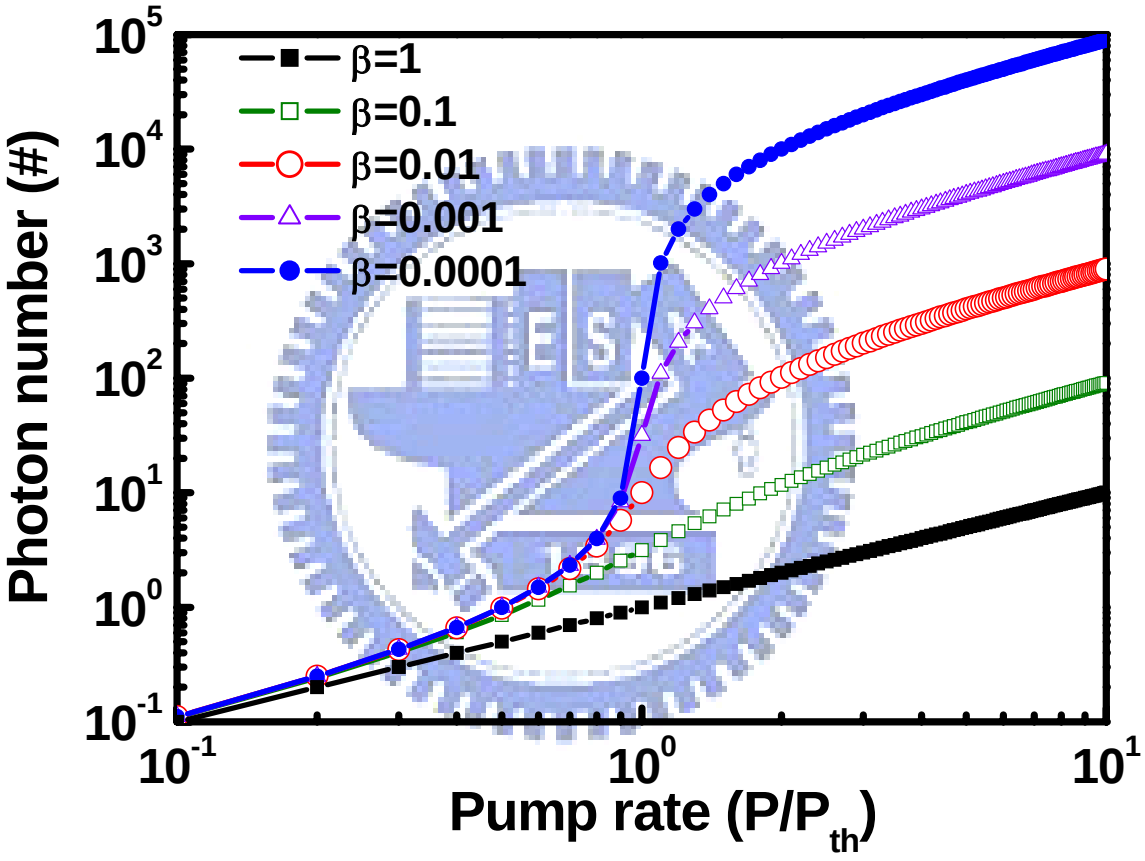

Figure 2.3 The internal photon number n_0 versus the pump rate P as a function of the spontaneous emission coefficient β.

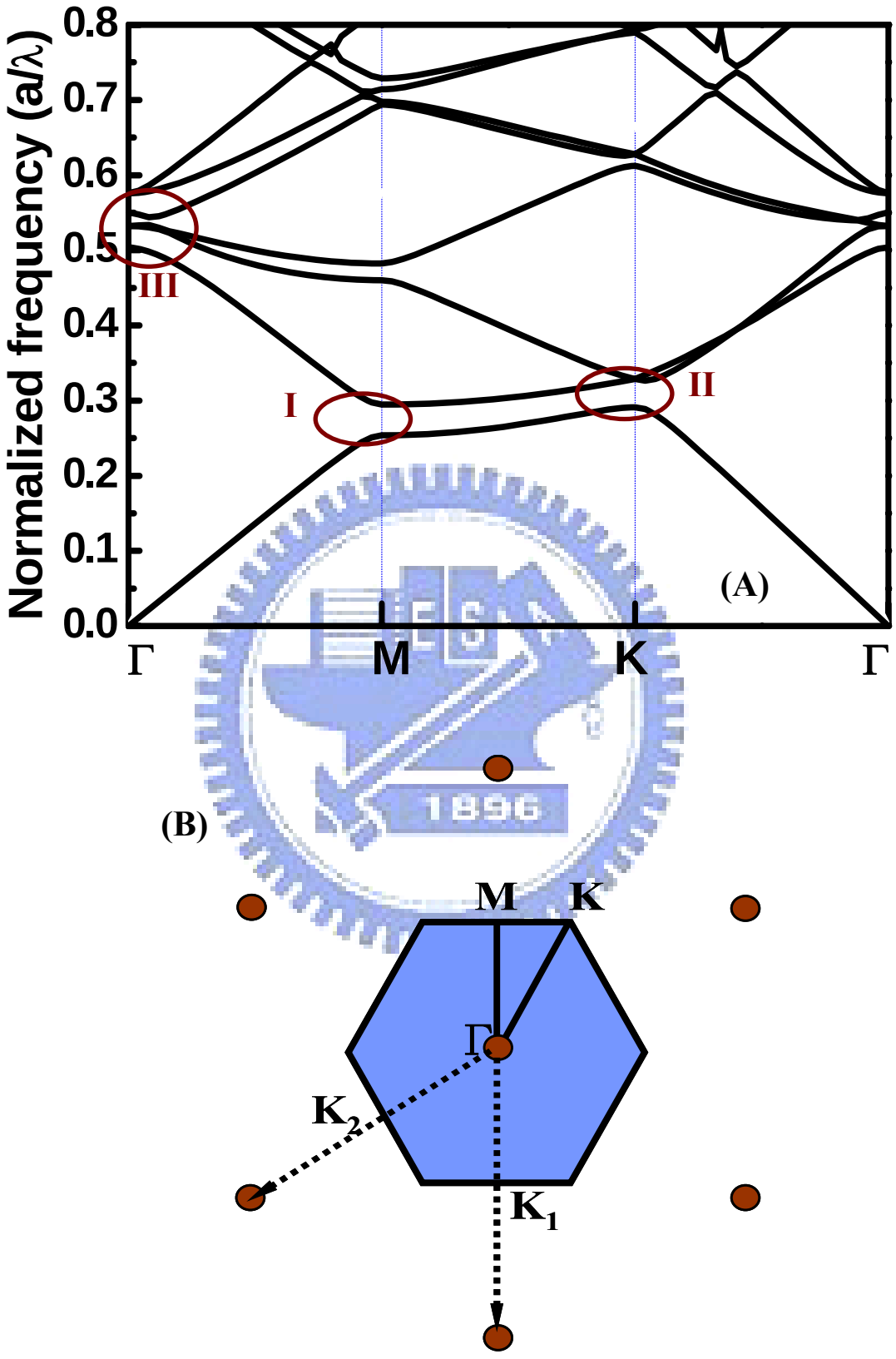

Figure 2.4 (A) The band diagram of a triangular-lattice photonic crystal.

(B) The schematic diagram of a reciprocal space.

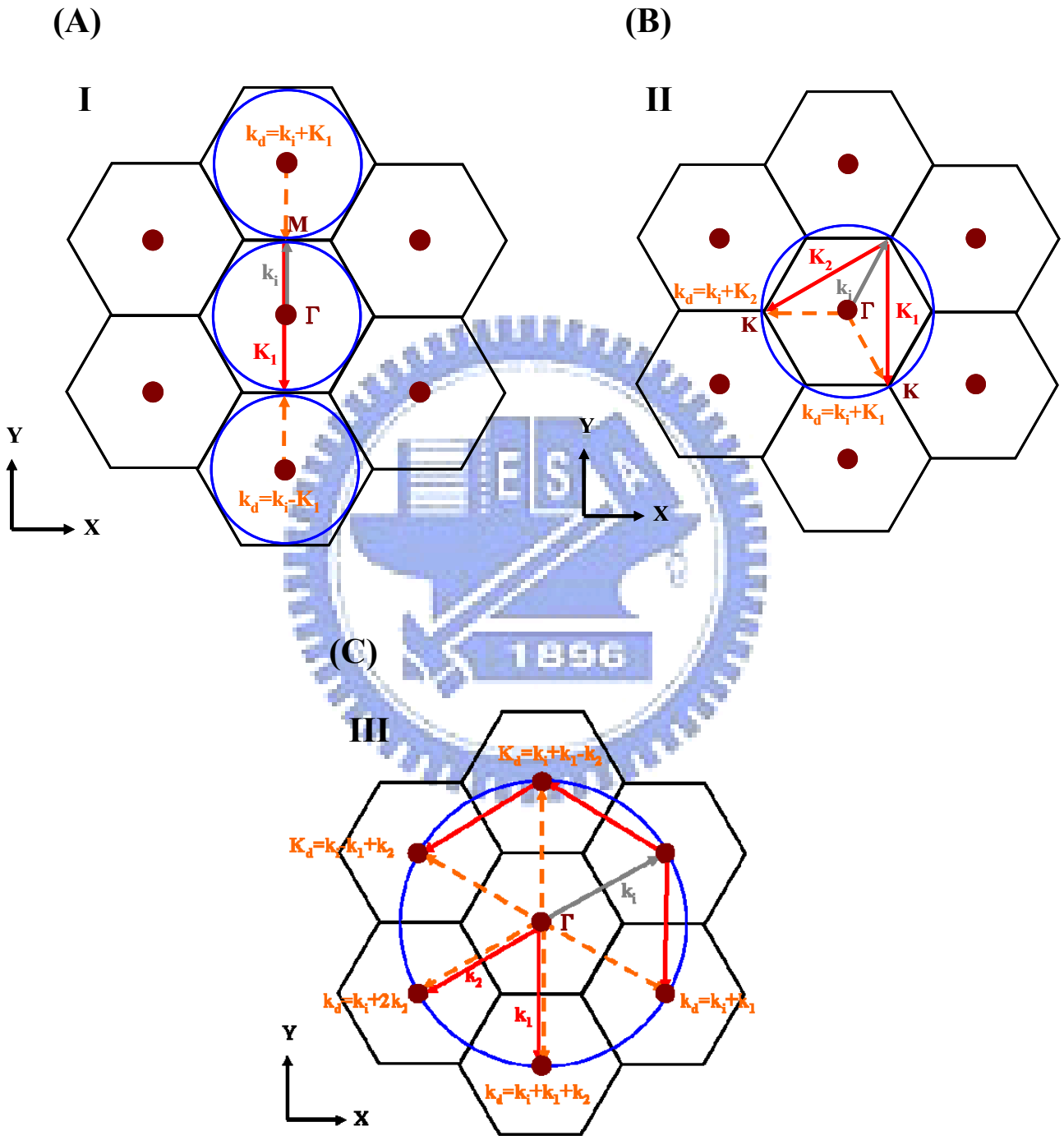

Figure 2.5 Wave-vector diagrams at (A) point I, (B) point II, and (C) point III. k_i and k_d indicate incident and diffracted wave vector.

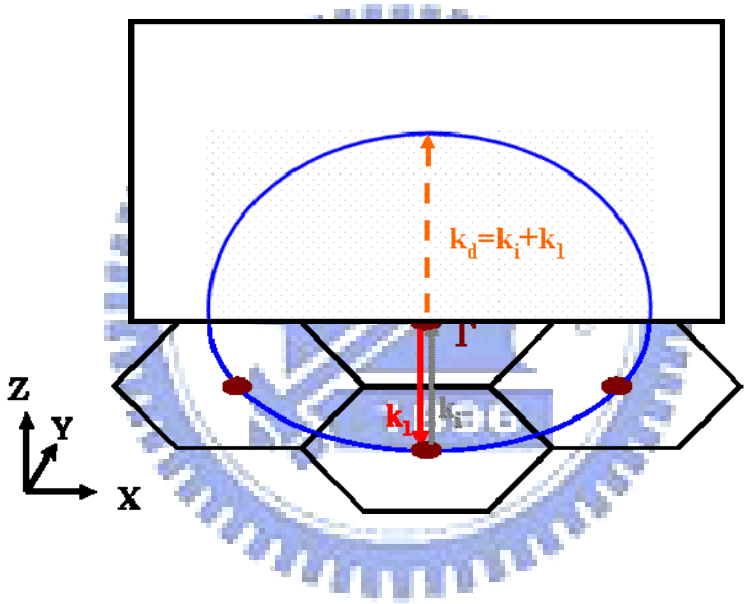

Figure 2.6 The wave-vector diagram at point III in vertical direction.

Chapter3

Fabrication and Characteristics of an Optically Pumped Nitride-Based VCSEL

Owing to the increasing demand of nitride laser diodes, researches on nitride-based VCSELs have been gradually growing. Optically pumped nitride-based VCSELs have been developed and investigated in recent years. Someya et al. [1] used 43 pairs of $Al_{0.34}Ga_{0.66}N$/GaN as the bottom DBR and reported the lasing action at ~400 nm. Zhou et al [2] employed a bottom DBR of 60 pairs $Al_{0.25}Ga_{0.75}N$/GaN and observed the lasing action at 383.2 nm. All these AlGaN/GaN DBR structures required large numbers of pairs due to the relatively low refractive index contrast between $Al_xGa_{1-x}N$ and GaN. Compared to those DBRs, the DBR structure using AlN/GaN has higher refractive index contrast ($\Delta n/n=0.16$) [3] that can achieve high reflectivity with relatively less numbers of pairs. It also has wide stop band that can easily align with the active layer emission peak to achieve lasing action. Therefore, the AlN/GaN is attractive for application in nitride VCSEL. However, the AlN/GaN combination has relatively large lattice mismatch (~2.4%) and the difference in thermal expansion coefficients between GaN (5.59×10^{-6}/K) and AlN (4.2×10^{-6}/K) that tends to cause cracks in the epitaxial film during the growth of the AlN/GaN DBR structure and could result in the reduction of reflectivity and increase in scattering loss. Fortunately, with the improvement of epitaxy, the growth of high-reflectivity AlN/GaN DBR has become possible.

In this chapter, we report the design and fabrication of GaN-based VCSEL using the AlN/GaN DBRs as the bottom mirror and a Ta_2O_5/SiO_2 dielectric multiple layer structure as

the top DBR mirror, and demonstration of the laser operation under optical pumping at room temperature.

3-1 Design of a Nitride-based VCSEL [4-6]

The design of a typical VCSEL structure should consider three dominant components: the micro-cavity length, the location of active region, and how many pairs of DBR layers we should coated. To achieve lasing action of VCSEL, a careful evaluation and design for the active region and the DBRs are quite important. In this section, we discuss the design of nitride-based VCSEL with hybrid cavity. The hybrid cavity is a cavity sandwiched by an epitaxial grown AlN/GaN DBR and a Ta_2O_5/SiO_2 dielectric DBR. The design for each component in our VCSEL structure is determined by considering the analysis of the reflectance of DBRs and the electric field distribution inside our structure. The cavity length was designed to be five-lambda in optical length (λ~450 nm).

3-1.1 Reflectance Simulation of Ta_2O_5/SiO_2 and Nitride-based DBRs

The simulation of nitride-based DBRs [7]

To determine how many pairs DBRs are required for a VCSEL, the realization of reflectivity spectra of DBR is inevitable and necessary. In the following, we simulate and discuss the reflectance of bottom and top reflectors we used, AlN/GaN and Ta_2O_5/SiO_2 DBRs, to understand the DBR pairs we required at least to deposit for a VCSEL. Reflectivity spectra of DBR structures here were simulated using the transfer matrix method. The incident angle of illumination and wavelength of the reference light were set to be 0^o (the direction normal to the sample surface) and 450nm, respectively.

AlN/GaN DBRs

The refractive index of GaN and AlN at wavelength of 450 nm, used as the parameters in the simulation, were n_{GaN} = 2.45 and n_{AlN} = 2.05. Figure 3.1 shows the reflectance spectrum

of 5, 10, 15, and 25 pairs of AlN/GaN DBR. The reflectivity value at center wavelength rapidly rises with the increasing of used pairs. As the pairs of DBR were 25 pairs, AlN/GaN DBR could theoretically achieve a high reflectivity of 99% at 450 nm and a wide stop-band about 46nm. The superiority of the AlN/GaN DBR also could be further confirmed using the simulation. Figure 3.2 shows the reflectivity spectra of three different nitride-based DBRs, AlN/GaN DBR, $Al_{0.25}Ga_{0.75}N$/GaN DBR, and $Al_{0.35}Ga_{0.65}N$/GaN DBR, with high reflectivity larger than 99% at 450 nm. Other two DBRs with low aluminum contents both show large required pairs (>50 pairs) and small stop-band (<20 nm). Compared to those nitride reflectors, the AlN/GaN DBR obviously reveals relatively wide stop-band and high reflectivity with relatively few pairs.

Ta_2O_5/SiO_2 DBRs [8, 9]

Dielectric mirror has the advantage of the large refractive index contrast between two different dielectric materials so it only needs a few pairs of DBR to form high reflectivity mirror. In most dielectric DBRs, SiO_2 is usually used as the low refractive index material due to its some advantaged characteristics such as relative low refractive index than many other dielectric materials. It is easy and cheap to get, hard to decompose, and high transparent window from the wavelength of 180 nm to 8 μm. As to the high refractive index material, Ta_2O_5 is a proper selection owing to benefits of low absorption and high transparency in visible to IR ray. The refractive index of SiO_2 and Ta_2O_5 at wavelength of 450 nm, used as the parameters in the simulation, are $n_{SiO2} = 1.463$ and $n_{Ta2O5} = 2.15$. Figure 3.3 shows the reflectance spectrum of 3, 5, and 8 pairs of Ta_2O_5/SiO_2 DBR. The 8 pairs of Ta_2O_5/SiO_2 mirror can have a high reflectivity of 99% and the wide stop band about 128 nm. Therefore, we use at least 8 pairs of Ta_2O_5/SiO_2 DBR as the top mirror in the following experiments.

3-1.2 Optimization of Location of the Active Region in a VCSEL

In addition to the consideration of high-reflectivity mirror, the location of active region,

usually in the form of MQWs, is also an important issue to the fabrication of GaN-based VCSEL. The active region plays a role of the gain medium. How to effectively make photons to oscillate with active medium is an important consideration. If we put the gain medium at the node of optical field, the interaction between light and electrons would be very weak, therefore, the gain medium couldn't efficiently provide gain for lasing action. On the contrary, the lasing threshold would be significantly lowered if the active region was put at anti-node of optical field. For a typical VCSEL, the cavity length is designed to be 1/2 lambda or 1 lambda, so the antinode of optical field and active region could be easily designed to match each other. However, in our design, the cavity length has been determined to be five-λ (optical length), which correspond to a geometric thickness of about 880 nm, due to the consideration of device fabrication. The structure should compose of a p-type GaN, MQWs, an n-type GaN, and a bottom nitride-based reflector. We set the thickness of the p-type GaN to be about 100 nm, of MQWs to be about 100 nm, and of the n-type GaN to be about 680 nm as initial design, and slightly modified these thicknesses to make the center of MQWs at the anti-node of optical field. Figure 3.4 shows the electric field intensity (EFI) and the refractive index as the functions of the distance from top layer. The optimal thickness of the p-type GaN, n-type GaN, and MQWs are about 120 nm, 660 nm, and 100 nm (ten pairs $In_{0.2}Ga_{0.8}N$/GaN MQWs (3 nm/7 nm)). From the figure, it can be observed that a pronounced resonant enhancement of the electric field was built up in the active region. It suggests that the light could be amplified inside the resonant cavity and the more opportunity could be obtained to achieve laser operation.

3-2 Fabrication of the Nitride-Based VCSEL Structure

The nitride-based structures including micro-cavity and bottom reflector in the experiments were grown in a vertical-type MOCVD system (EMCORE D-75) with a fast rotating disk, which can hold one 2-inch wafer. The polished optical-grade C-face (0001)

2-inch-diameter sapphire was used as substrate. Trimethylindium (TMIn), Trimethylgallium (TMGa), Trimethylaluminum (TMAl), and ammonia (NH_3) were used as the In, Ga, Al, and N sources, respectively. In this section, the fabrication of the nitride-based VCSEL is divided into two parts: (1) Growth of nitride-based reflectors and micro-cavity. (2) Deposition of dielectric mirror.

3-2.1 Growth of Nitride-Based Reflectors and Micro-Cavity

The nitride-based DBR used in the experiment is the stacks of 29-pair AlN/GaN layers with insertion of the AlN/GaN super-lattice (SL). The super-lattice in structure is inserted for releasing strain during the growth of AlN/GaN DBR to further improve interface and raise reflectivity of the DBR. The growths and characteristics of the DBR and micro-cavity are described as following:

This grown DBR structure is consist of a 30-nm-thick GaN nucleation layer grown at 500 °C, a 2-μm-thick GaN bulk layer grown at 1100 °C, and 29 pairs of quarter-wave GaN/AlN layers with AlN/GaN SLs grown at 1100 °C. For the DBR structure, six sets of a half-wave layer consisting of 5.5 periods of GaN/AlN SL and GaN layer were inserted in every five pairs of the 29-pair GaN/AlN DBR structure. The thicknesses of AlN and GaN layers are ~3–5 nm in SL. The ambient gas was changed from hydrogen into nitrogen before the DBR layers were grown. The center wavelengths of these DBRs was designed to be around 450 nm. The detail of the growth was reported elsewhere [10]. Figure 3.5(A) shows cross-sectional transmission electron microscopy (TEM) images of the SL sample. The lighter layers represent AlN layers while the darker layers represent GaN layers. In figure 3.5(A), no cracks can be observed in the TEM image. However, some V-shaped defects dark spots were still observed on the interfaces of GaN or AlN layers in figure 3.5(A). These V-shaped defects have been reported earlier to be due to various origins such as stacking mismatch boundaries and surface undulation [11]. Figure 3.5(B) shows the cross section of one set of 5.5 pairs of

GaN/AlN SL insertion layers. The interface between GaN and AlN is sharp and abrupt. Figure 3.6 shows the AFM image of the DBR. The surface is lumpy, and the drop in height is within the range of 10-30 nm. The reflectivity spectrum of the AlN/GaN DBR is shown in figure 3.7 shows the highest reflectivity of the DBR is about 99% at 460 nm. The stop-band of the DBR is as wide as about 30 nm.

Then, a micro-cavity formed by a p-n junction was grown following the growth of the DBR structure. The micro-cavity composed of a 660-nm-thick n-type GaN, a ten pairs $In_{0.2}Ga_{0.8}N$/GaN (3 nm/7 nm) MQW, and a 120-nm-thick p-type GaN. The cavity length is 5-λ in optical length. Figure 3.8 (A) and (B) shows optical microscopy (OM) and the cross-sectional TEM images of the as-grown sample, respectively.

3-2.2 Deposition of the Dielectric Mirror

The final process to complete a VCSEL is the deposition of a dielectric mirror. The dielectric mirror in the experiment, an eight pairs Ta_2O_5/SiO_2 DBR, was deposited using the electron beam evaporation. The dielectric mirror was coated onto as-grown sample surface in an O_2 ambient at the controlled temperature below 170°C. The reflectivity spectrum of the dielectric mirror was measured as shown in figure 3.9. The Ta_2O_5/SiO_2 DBR shows a very high reflectivity as high as 99% centered at 450 nm with a wide stop-band of about 100 nm. The schematic diagram of the overall VCSEL structure is shown in Fig. 3.10 (A). The scanning electron microscopy (SEM) and OM images of the overall VCSEL structure are also shown in the figure 3.10(B) and (C), respectively.

3-3 Measurement and characteristics of nitride-based VCSELs

3-3.1 Photoluminescence and Quality Factor of Nitride-based VCSELs

Photoluminescence of the VCSEL structure

The photoluminescence (PL) emission was excited by a 325 nm He-Cd laser with a spot

size of about 2-μm-diameter. By using the microscopy system (WITec, alpha snom), the emission was collected into a spectrometer/CCD (Jobin-Yvon Triax 320 Spectrometer) with a spectral resolution of ~0.15 nm for spectral output measurement. Figure 3.11 shows the PL emission of the as-grown structure and the VCSEL structure, and the reflectivity spectrum of the VCSEL structure. The PL emission peak wavelength and the FWHM of emission spectrum of MOCVD grown structure were 465 nm and 10.5 nm, respectively. After the coverage of top reflector, the PL emission of and the FWHM of emission spectrum of overall VCSEL structure became 464 nm and 0.6 nm, respectively. It is obvious that the PL emission peak wavelength of overall VCSEL structure was modified by cavity mode, which could be seen from the reflectivity spectrum of full structure (the dip in stop-band), and centered at 464 nm. The narrow FWHM of 0.6 nm is an evidence of the strong Febry-Perot cavity effect existing in our VCSEL sample.

Quality factor of the VCSEL structure

A narrow PL emission with full width at half maximum of 0.6 nm corresponds to the cavity resonant mode at 464 nm was observed. It indicates the spontaneous emission generated from MQWs was well-aligned the narrow vertical-cavity mode resulting from the high reflectivity of AlN/GaN DBR and dielectric mirror. The cavity quality factor is a value usually used to evaluate how good a cavity is. Generally, the cavity quality factor is defined as $Q = \frac{\lambda}{\Delta\lambda}$, where λ is the wavelength emitted form cavity and $\Delta\lambda$ is the FWHM of the emission peak. Therefore, we could obtain the Q value of our VCSEL structure to be about 777. This value was further confirmed and roughly consistent with the theoretical estimation using the following equations:

$$Q = \frac{2nL}{\lambda} \frac{\pi}{1 - \sqrt{R_1 R_2} e^{-\alpha L}}$$

where R_1, R_2 are the reflectivity of bottom and top reflectors, L is the cavity length, α is absorption coefficient of GaN, and n is refractive index of GaN. Here we consider the

absorption loss in GaN at 460 nm is 1 - 200 cm^{-1} at 460 nm [12], and the high reflectivity of top and bottom reflectors are both 99% at 460 nm.

Optical pumping setup

The optical pumping of the sample was performed using a frequency-tripled Nd:YVO_4 355-nm pulsed laser with a pulse width of ~ 0.5 ns at a repetition rate of 1 kHz. The pumping laser beam with a spot size of 60 μm was incident normal to the VCSEL sample surface. The light emission from the VCSEL sample was collected using an imaging optic into a spectrometer/CCD (Jobin-Yvon Triax 320 Spectrometer) with a spectral resolution of ~0.15 nm for spectral output measurement. Figure 3.12 shows the schematic diagram of the setup.

3-3.2 Characteristics of Nitride-based VCSELs

Threshold characteristics

The light emission intensity from the VCSEL as a function of the pumping energy is shown in figure 3.13. A distinct threshold characteristic was observed at the threshold pumping energy (E_{th}) of about 180 nJ corresponding to an energy density of 6.4 mJ/cm^2 (threshold energy density is 2.56 mJ/cm^2 if considering some energy loss due to reflectivity of DBR). Then the laser output increased linearly with the pumping energy beyond the threshold. The carrier density at the threshold is estimated to be about 2×10^{19} cm^{-3}, assuming the reflectivity of the top mirror at pumping wavelength of 355 nm was 40%, the absorption coefficient of the GaN was about 10^5 cm^{-1} at 355 nm [12] and the quantum efficiency was 10% [1]. We estimated the threshold gain (g_{th}) of the VCSEL cavity using the equation:

$$g_{th} = (L_c / N_w L_w)\alpha_i + (\mathbf{1}/\mathbf{2}N_w L_w)\ln(\mathbf{1}/R_1 R_2)$$

where L_c is effective cavity length (including penetration depth of DBR, which could be estimated using Eq. (2. 20), α_i is absorption coefficient of GaN at lasing wavelength, N_w is the number of quantum wells, L_w is the width of each quantum well and R_1, R_2 are the reflectivity of the top and bottom mirrors, respectively. We obtained the required threshold

gain is about 8.7×10^3 cm^{-1}. The parameters used in the estimations of carrier density at threshold and threshold gain are listed in the Table 3.1. The threshold gain value at the threshold carrier density is slightly lower than the gain value of Park's report [13].

Figure 3.14 shows the variation of emission spectrum with the increasing pumping energy. A dominant laser emission line at 456 nm appears above the threshold pumping energy. The laser emission spectral linewidth reduces with the pumping energy above the threshold energy and approaches 0.2 nm above the pumping energy of $1.3E_{th}$.

The emission images under different pumping energy were shown in figure 3.15. The blue spontaneous emission could be seen as the pumping energy was below threshold. With the pumping energy increasing above threshold, a laser spot with relatively strong intensity appears, and the intensity of the spot rapidly increases. This result shows the nitride-based VCSEL is a spot-type laser.

Laser polarization

The contrast of laser emission intensity between two orthogonal polarizations was measured by rotating a polarizer in front of the laser beam. Figure 3.16 shows the laser emission intensity as a function of the angle of the polarizer at the pumping energy of $1.71E_{th}$. The variation of intensity with the angle of the polarizer shows nearly a cosine square variation. The degree of polarization (P) is defined as $P = \frac{I_{max} - I_{min}}{I_{max} + I_{min}}$, where I_{max} and I_{min} are the maximum and minimum intensity of the nearly cosine square variation, respectively. The result showed the laser beam has a degree of polarization of about 84% suggesting strong polarization property of the laser emission.

Near field pattern (NFP) and far field pattern (FFP)

The near-field pattern (NFP) and far-field pattern (FFP) of the laser were detected by the CCD and were plotted as shown in figure 3.17(A) and (B). Figure 3.17(A) shows the near-field emission intensity as a function of the spatial position. From the figure, we could

obtain the spot size defined by the FWHM and $1/e^2$ of the intensity profile to be about 1.3 μm and 3 μm, respectively. Figure 3.17(B) shows the far-field emission intensity as a function of the angle between the light direction and the axial perpendicular to the surface. The divergence angle determined by the FWHM could be estimated from the far-field profile to be as small as about 7.6°. Furthermore, both NFP and FFP show that the intensity distributions along two cross axes are almost the same. That is, the laser is actually a vertically emitted single-mode and circular-shape emission beam.

Characteristic Temperature

Figure 3.18 shows the semi natural-logarithm plot of the dependence of the threshold pumping energy ($\ln E_{th}$) on the operation temperature (T). The threshold energy gradually increased as the operation temperature rose from 120 K to 300 K. The relationship between the threshold energy and the operation temperature could be characterized by the equation $E_{th}=E_0\times e^{T/T_0}$, where T_0 is the characteristic temperature and E_0 is a constant. Therefore, we obtain a high characteristic temperature of about 244 K by linear fitting the experiment data. This high T_0 could be understood by some temperature-dependent properties of the components in the nitride structure, active region and DBR. The lasing wavelength shows a slight red shift about 1.6 nm as the temperature rose from 120 K to 300 K as shown in figure 3.19. The PL emission of the MQW was also measured and shows a red shift about 2.9 nm over the same temperature range. It should mean the gain peak moves somewhat faster than the cavity mode about 1.3 nm over the temperature range of 170 K. This shift is so small that the gain peak almost keeps aligning the cavity mode. In fact, the reflectivity of nitride-based DBR is also almost independent with the variation of temperature as shown in the figure 3.20. That is, the slightly shifted gain peak actually could keep meeting the highest reflectivity although temperature was varied. Therefore, the superior high temperature performance of the GaN-based VCSEL structure could be attributed to the almost invariant reflectivity spectrum of AlN/GaN DBR, and less shift of the gain peak and cavity mode as the temperature rises,

and the ten-pair $In_{0.2}Ga_{0.8}N$/GaN MQW structure which could suppress the carrier leakage from the MQW active layers to the cladding layers and) the thick GaN cavity (880 nm in thickness) providing a good heat dissipation path during the high carrier injection and high temperature conditions [14].

The coupling efficiency of spontaneous emission (β)

In order to understand the β of this cavity, we normalized the scales of figure 3. 13 and re-plotted it in a logarithm scale as shown in figure 3.21. Furthermore, we used the Eq. (2. 35) to fit our data, and the fitting result shows the β value of our VCSEL is about 2×10^{-2}. we also estimated the β value based on the approximation equation (2. 24):

$$F_p = \frac{3}{4\pi^2} \frac{Q}{V_c/(\lambda/n)^3}$$

$$\beta = \frac{F_p}{1+F_p}$$

where F_p is the Purcell factor, Q is the cavity quality factor, λ is the laser wavelength, V_c is the optical volume of laser emission, and n is the refractive index. As we have mentioned earlier, the photoluminescence spectrum of our GaN-based VCSEL showed a narrow emission peak with full width at half maximum of 0.6 nm, which corresponds to a cavity quality factor of 777. The refractive index is 2.45 for the GaN cavity. For the estimation of the optical volume, we used the laser spot size (at $1/e^2$ of near-field intensity profile) shown in figure 3. 17(a) which is about 3 μm and the cavity length of about 7λ with considering the penetration depth of the DBRs to estimate the V_c to be about 4×10^{-11} cm^3. By using these parameters, the Purcell factor of about 2.8×10^{-2} was obtained, and we estimated the β value to be about 2.2×10^{-2}, which is consistant with the above β value estimated from figure 3.21. This β value of the VCSEL is three order of magnitude higher than that of the typical edge emitting semiconductor lasers (normally about 10^{-5}) [1, 15] indicating the enhancement of the spontaneous emission into a lasing mode by the high quality factor microcavity effect in the VCSEL structure.

References

1.T. Someya, R.Werner, A. Forchel, M. Catalano, R. Cingolani and Y.Arakawa, *Science*, 285, 1905 (1999)

2. H. Zhou, M. Diagne, E. Makarona, A. V. Nurmikko, J. Han, K. E. Waldrip and J. J. Figiel, *Electron. Lett.*, 36,1777 (2000)

3. T. Ive, O. Brandt, H. Kostial, T. Hesjedal, M. Ramsteiner, and K. H. Ploog, *Appl. Phys. Lett*., 85, 1970 (2004)

4. P. Mackowwiak and W. Nakwaski, *J. Physics D: Applied Physics* 33, 642 (2000)

5. P. Mackowwiak and W. Nakwaski, *J. Physics D: Applied Physics* 34, 954 (2001)

6. P. Mackowwiak, T. Czyszanowski, R. P. Sarzala, M. Wasiak, and W. Nakwaski, *Opto-Electron. Rev.,* 11, 119 (2003)

7. G. W. Wood, U. Ozgur, H. O. Everitt, F. Yun, and H. Morkoc, *phys. stat. sol. (a)*, 188, 793 (2001)

8. 李正中, 薄膜光學與鍍膜技術, (1999)

9. E. D. Palik, Handbook of Optical Constants of Solids, *Academic Press Inc* (1985)

10. G. S. Huang, T. C. Lu, H. H. Yao, H. C. Kuo, S. C. Wang, C. W. Lin and L. Chang, *Appl. Phys. Lett.*, **88**, 061904 (2006)

11. H. K. Cho, J. Y. Lee, and G. M. Yang, *Appl. Phys. Lett.*, **80**, 1370 _2002_.

12. G. Yu, G. Wang, H. Ishikawa, and M. Umeno, T. Soga, T. Egawa, J. Watanabe, and T. Jimbo, *Appl. Phys. Lett.*, **70,** 3209 (1997)

13. S. H. PARK, *Jpn. J. Appl. Phys.*, **42**, L 170 (2003)

14. M. Ortsiefer, R. Shau, G. Bohm, F. Kohler, J. Rosskopf, and M. C. Amann, *Phys. Stat. Sol.* (a)**188**, No. 3, 913-919 (2001)

15. T. Tawara, H. Gotoh, T. Akasaka, N. Kobayashi, and T. Saitoh, *Appl. Phys. Lett*., **83**, 830 (2003)

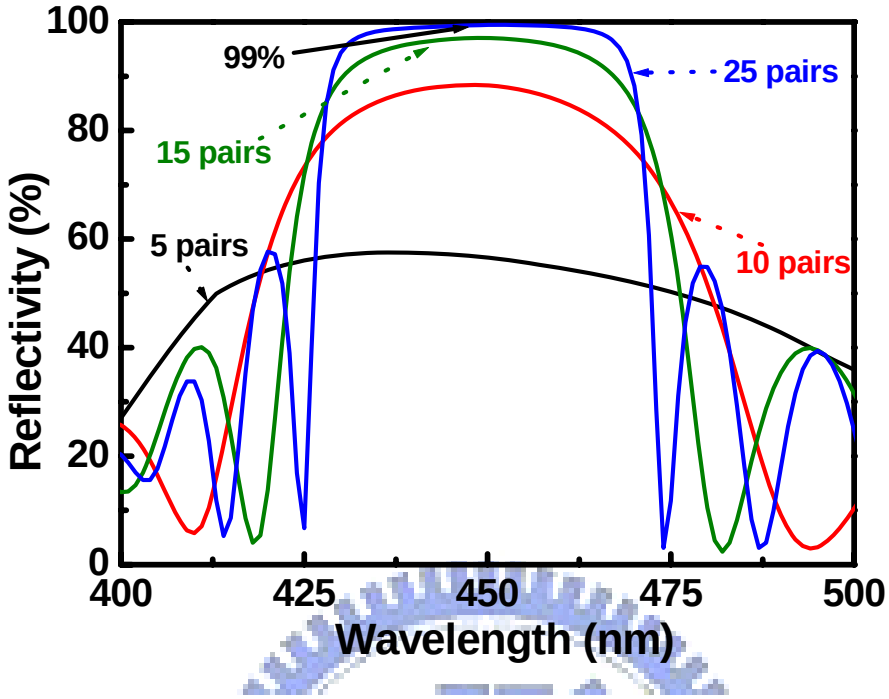

Figure 3.1 Simulated reflectivity spectra of 5, 10, 15, and 25 pairs of AlN/GaN DBR.

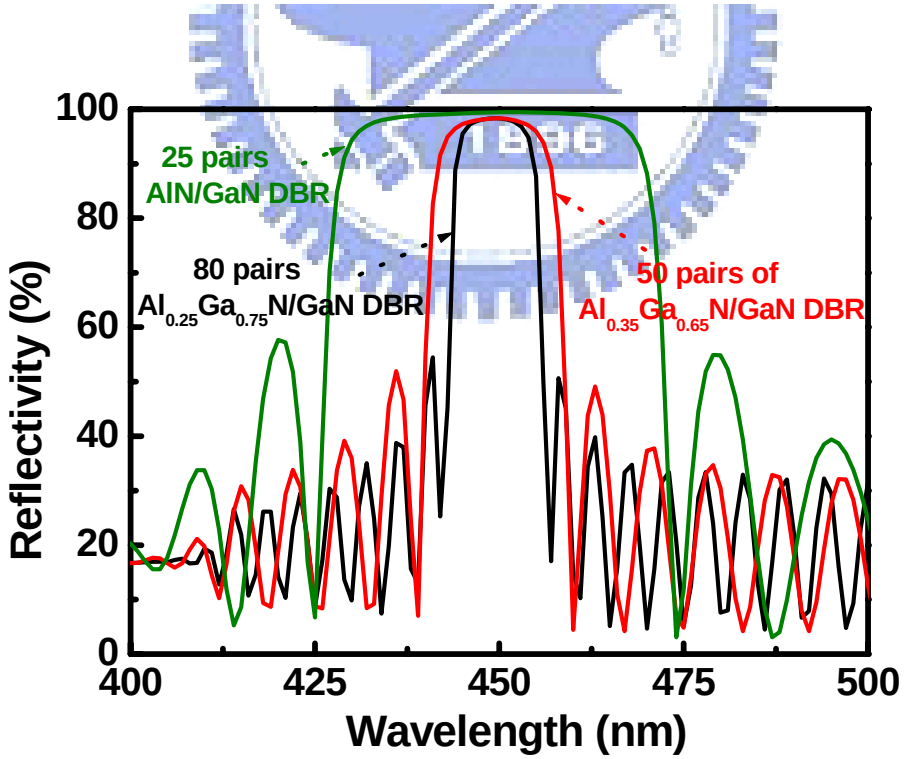

Figure 3.2 Simulated reflectivity spectra of three different nitride-based DBRs with high reflectivity.

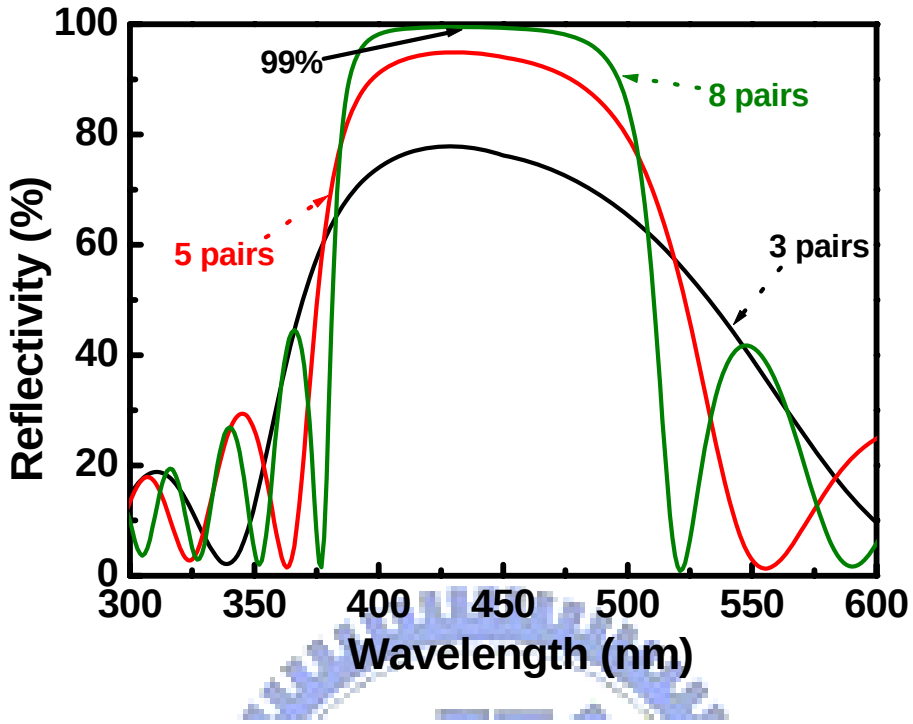

Figure 3.3 Simulated reflectivity spectra of 3, 5, and 8 pairs of Ta_2O_5/SiO_2 DBR.

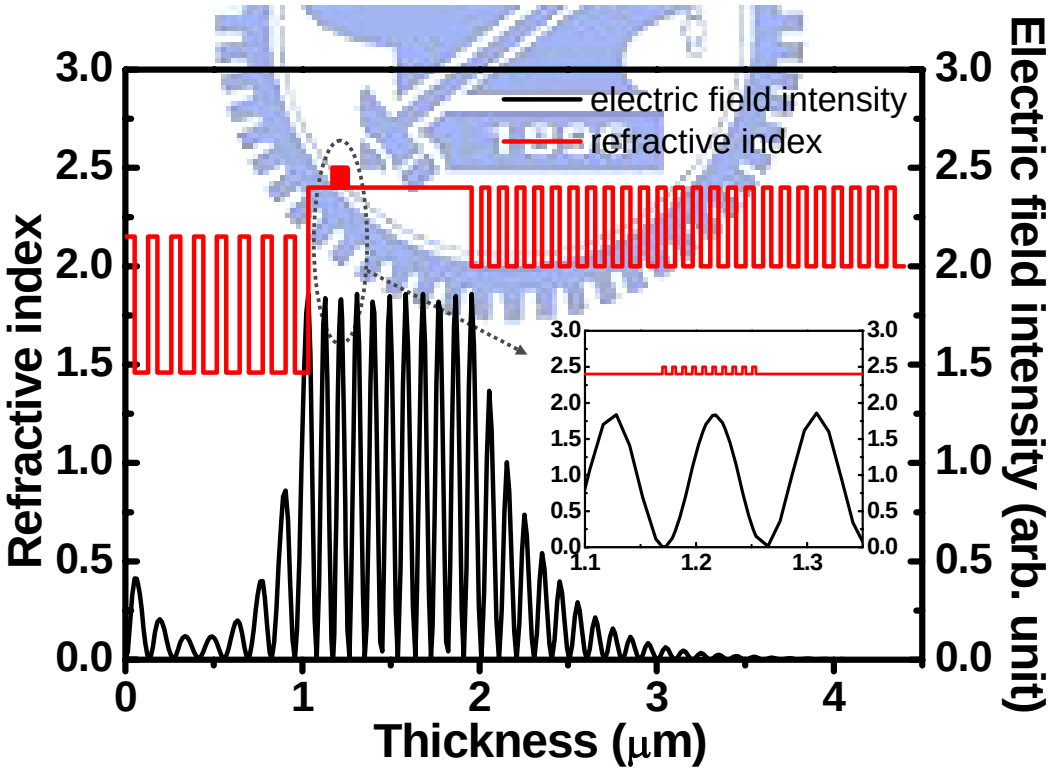

Figure 3.4 Electric field intensity and refractive index as a function of the distance from top layer.

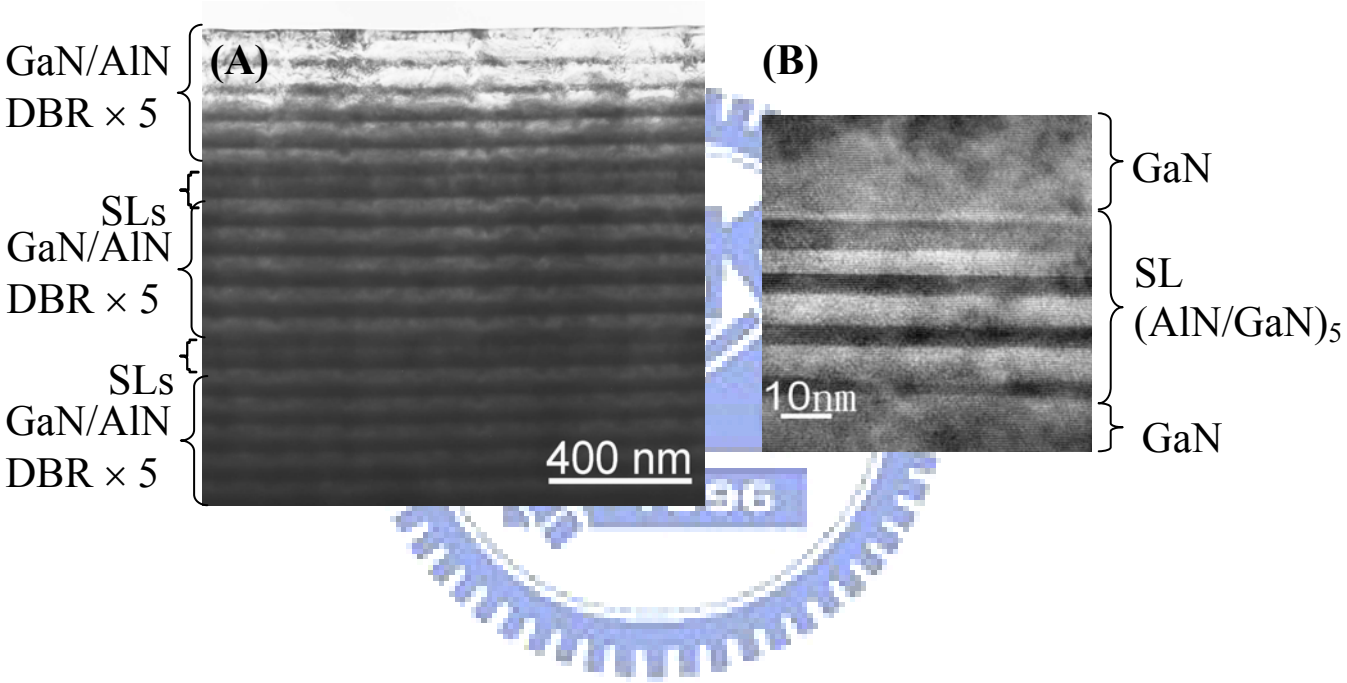

Figure 3.5 Cross-sectional TEM images of (A) the DBR sample and (B) one set of 5.5 pairs of GaN/AlN SL insertion layers.

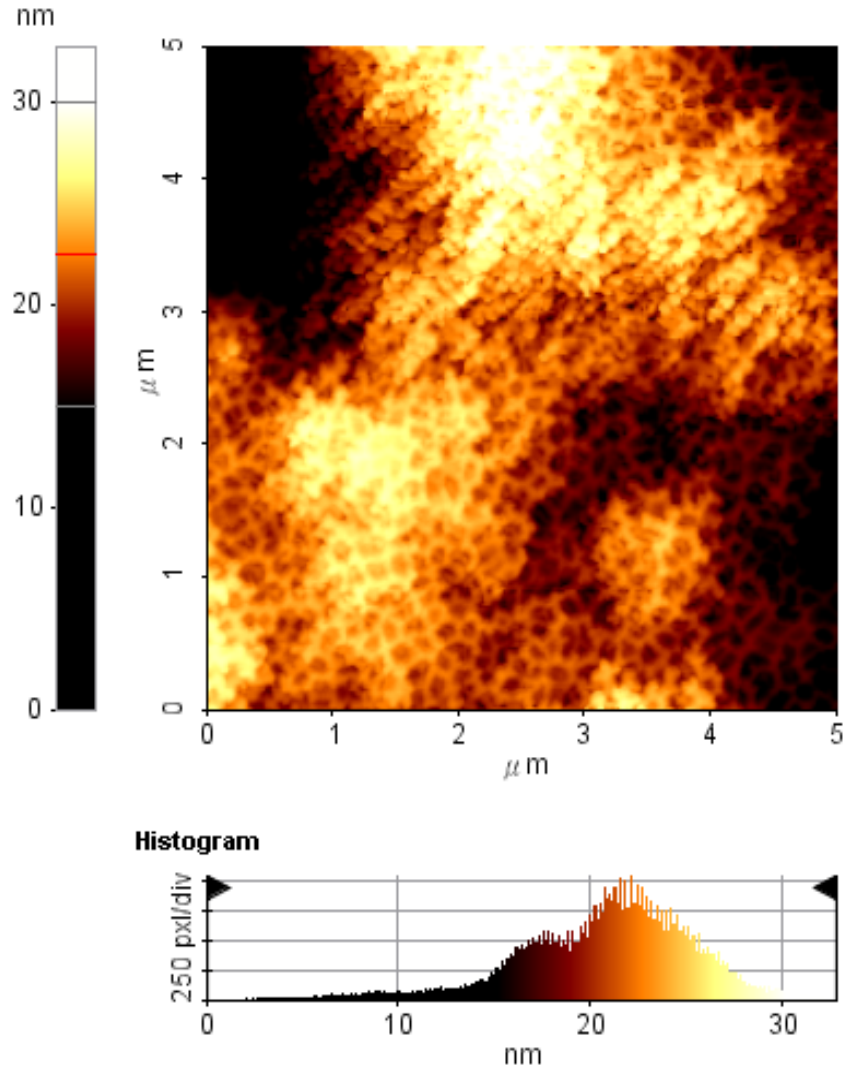

Figure 3.6 AFM image of the DBR sample.

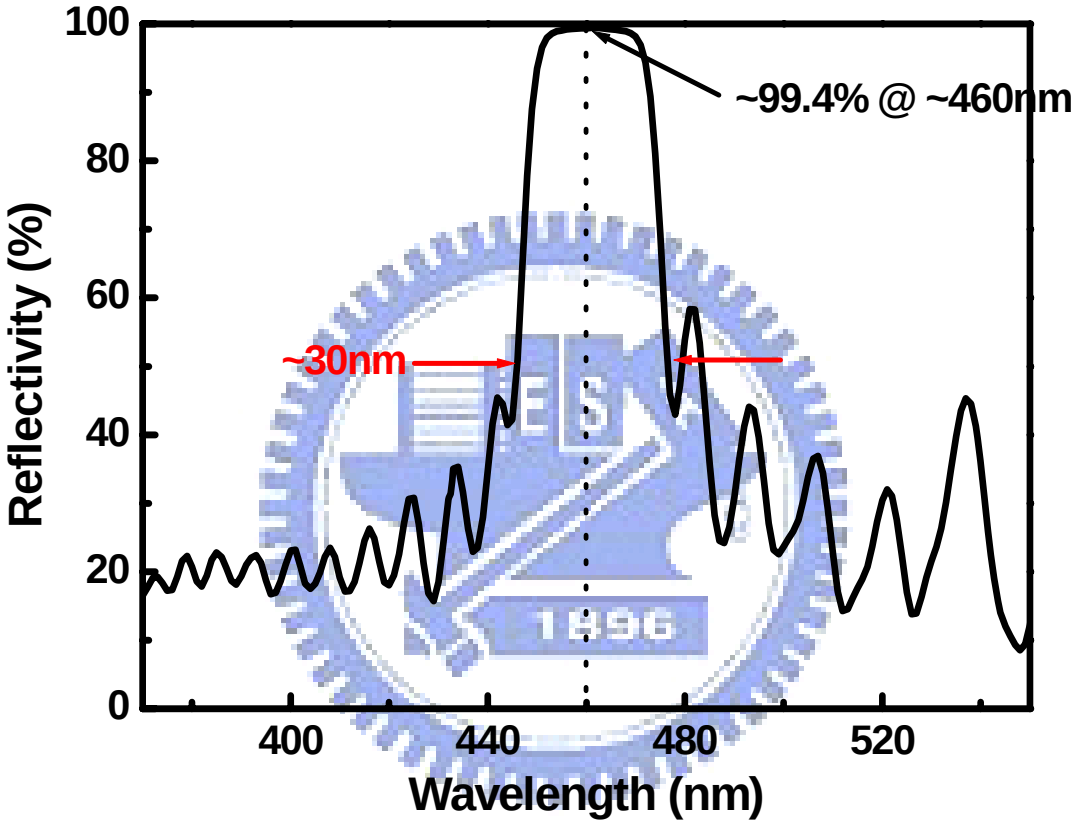

Figure 3.7 The reflectivity spectrum of the AlN/GaN DBR.

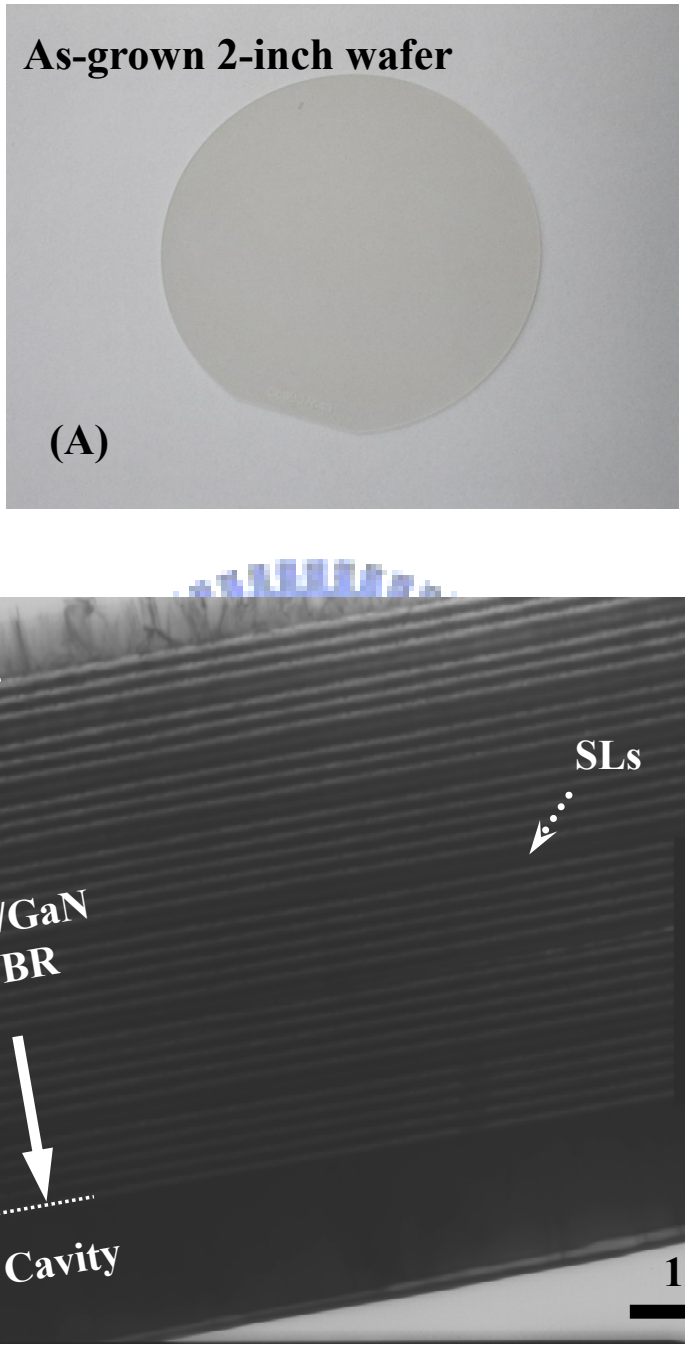

Figure 3.8 (A) OM and (B) cross-sectional TEM images of the as-grown micro-cavity sample.

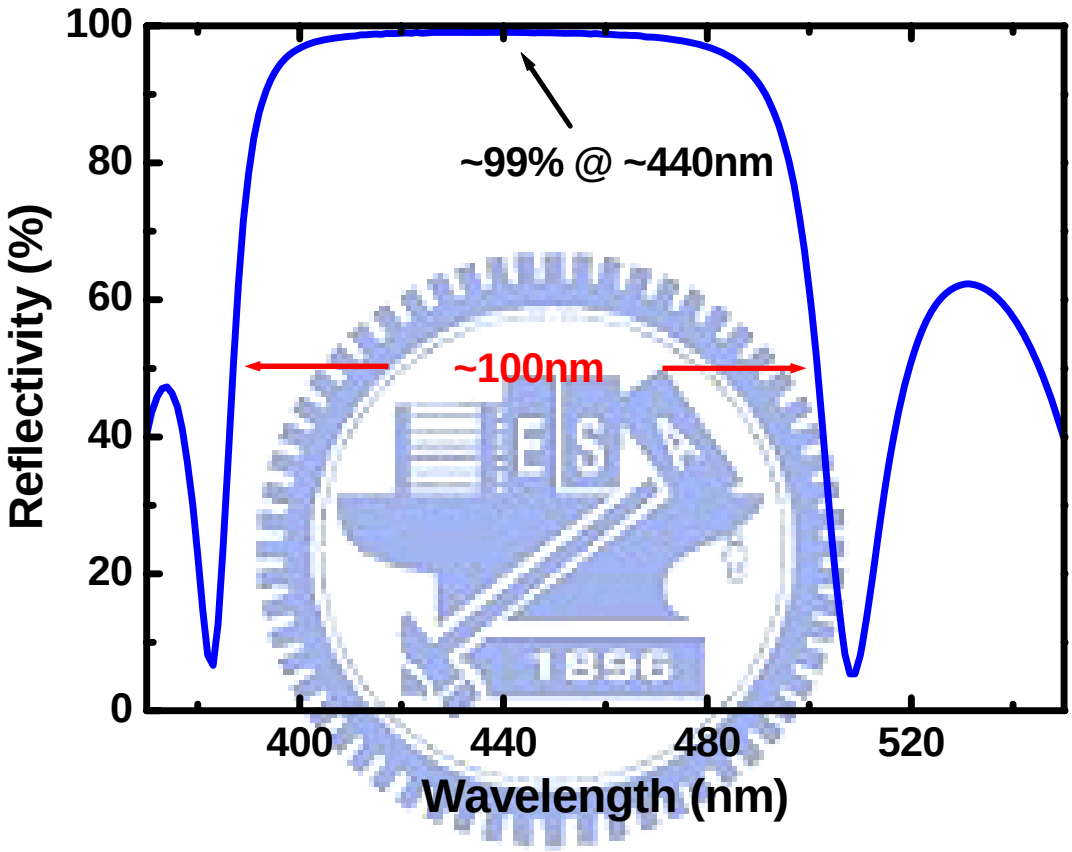

Figure 3.9 The reflectivity spectrum of the Ta_2O_5/SiO_2 DBR.

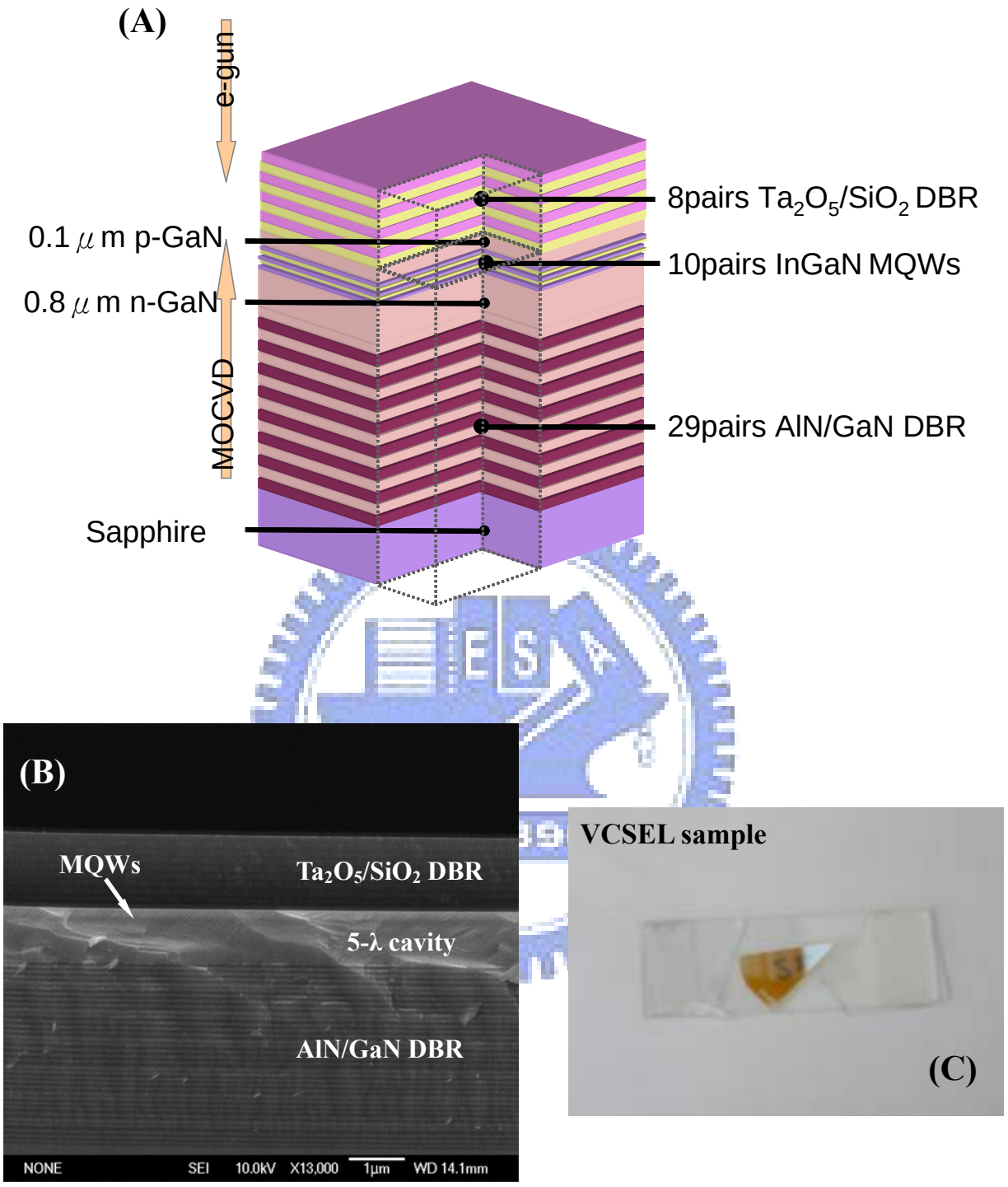

Figure 3.10 (A) Schematic diagram, (B) SEM image, and (C) OM images of the VCSEL structure.

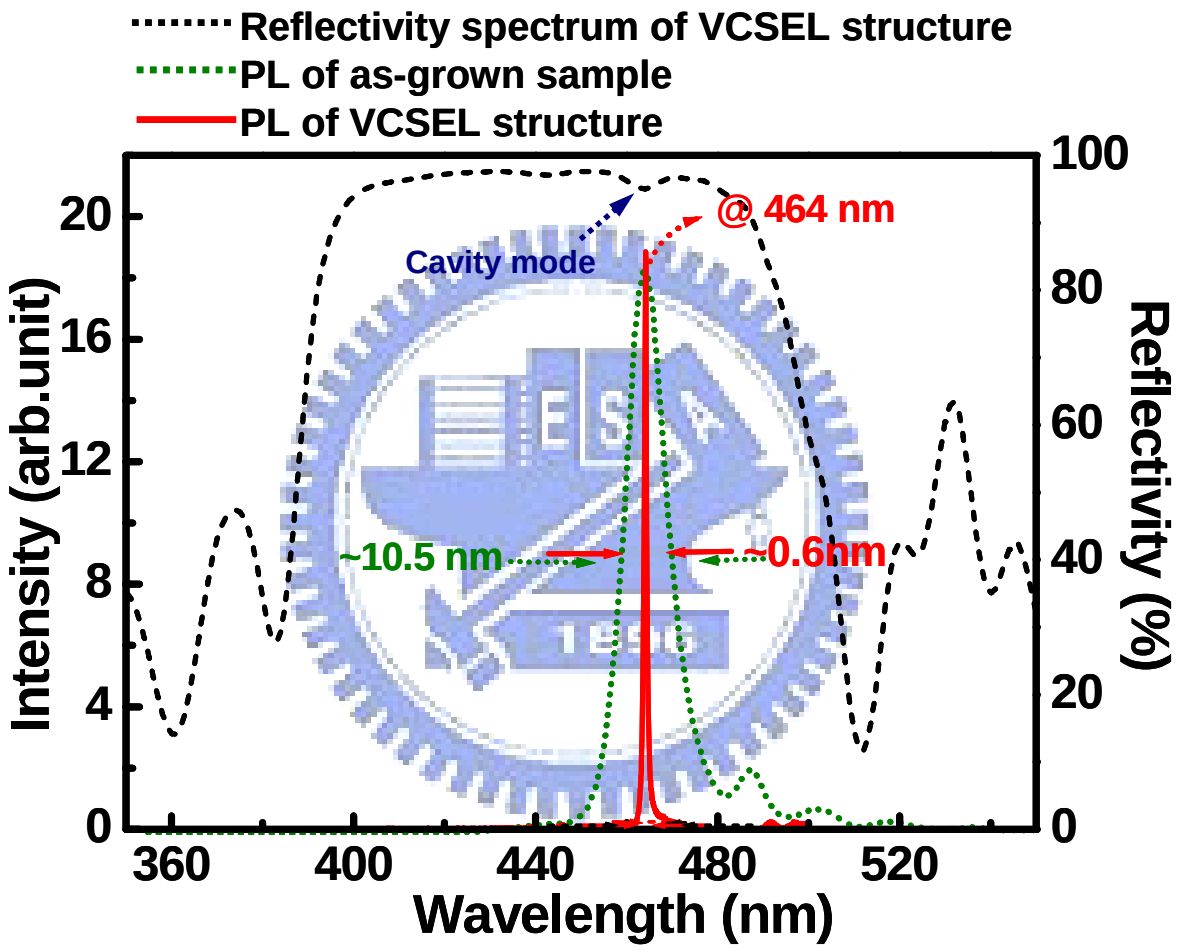

Figure 3.11 PL emission spectra of as-grown structure and VCSEL structure, and the reflectivity spectrum of VCSEL structure.

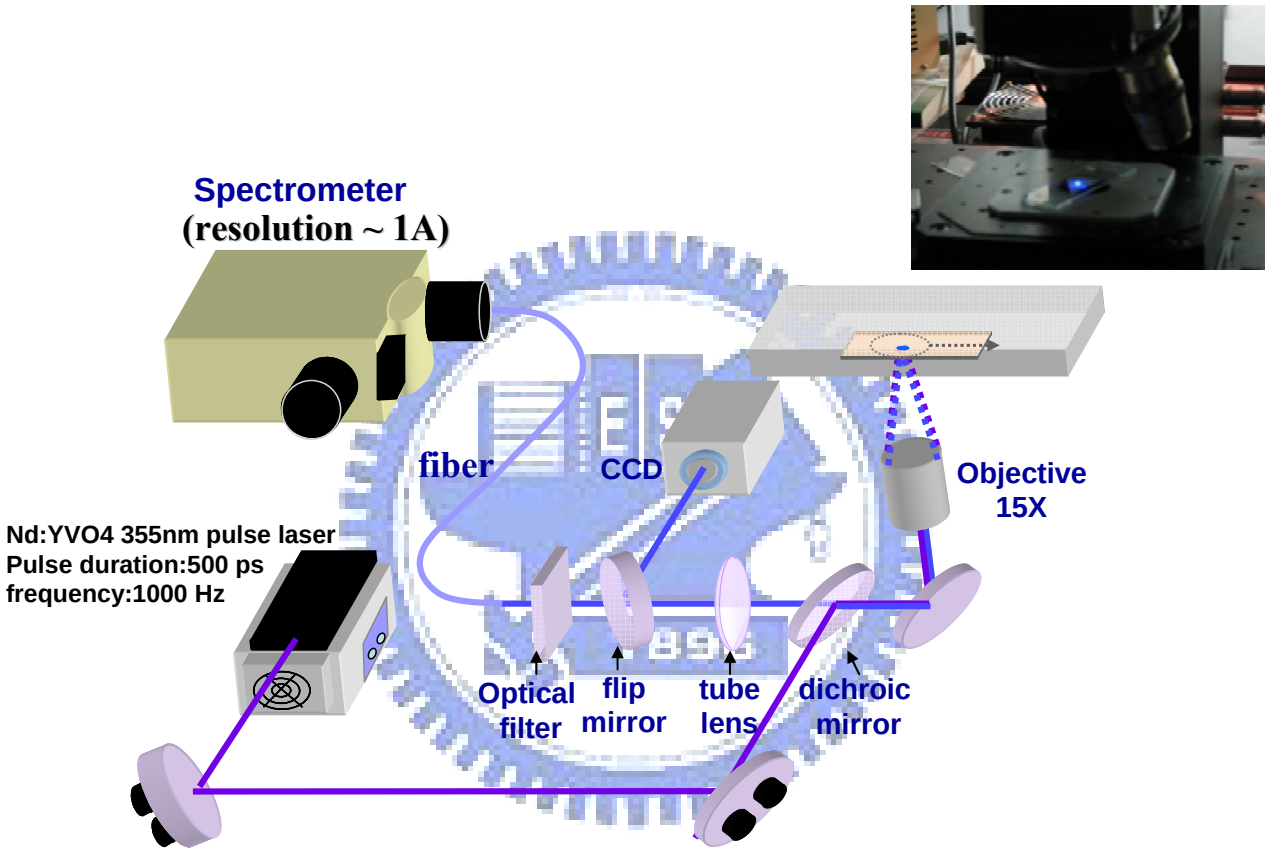

Figure 3.12 The optical pumping setup.

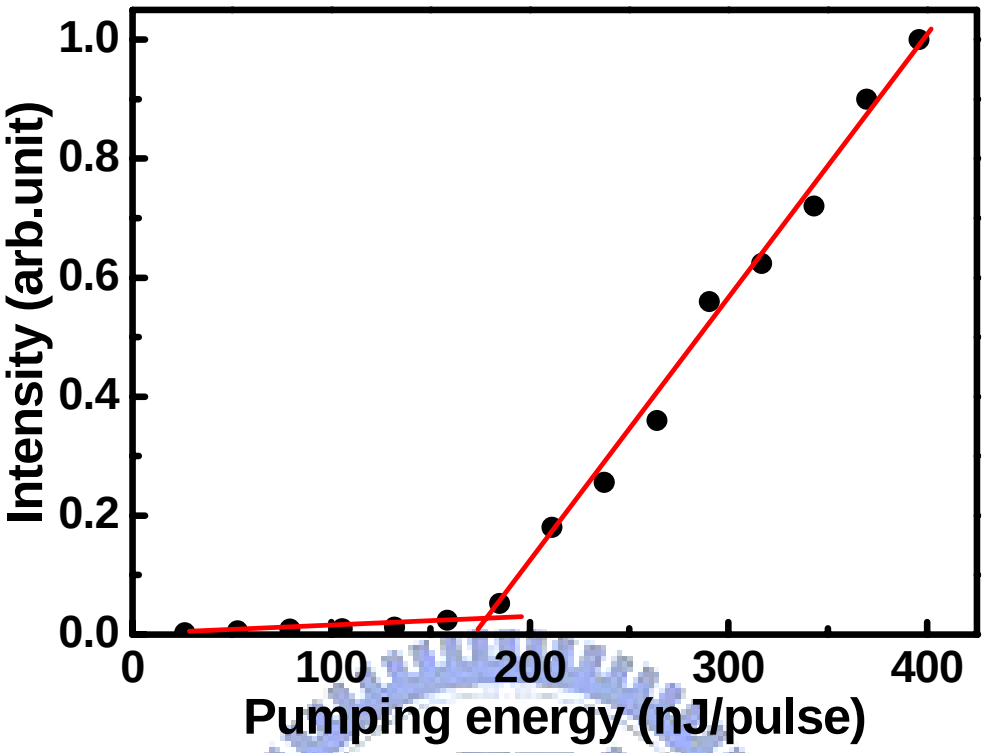

Figure 3.13 The light emission intensity of VCSEL as a function of the pumping energy.

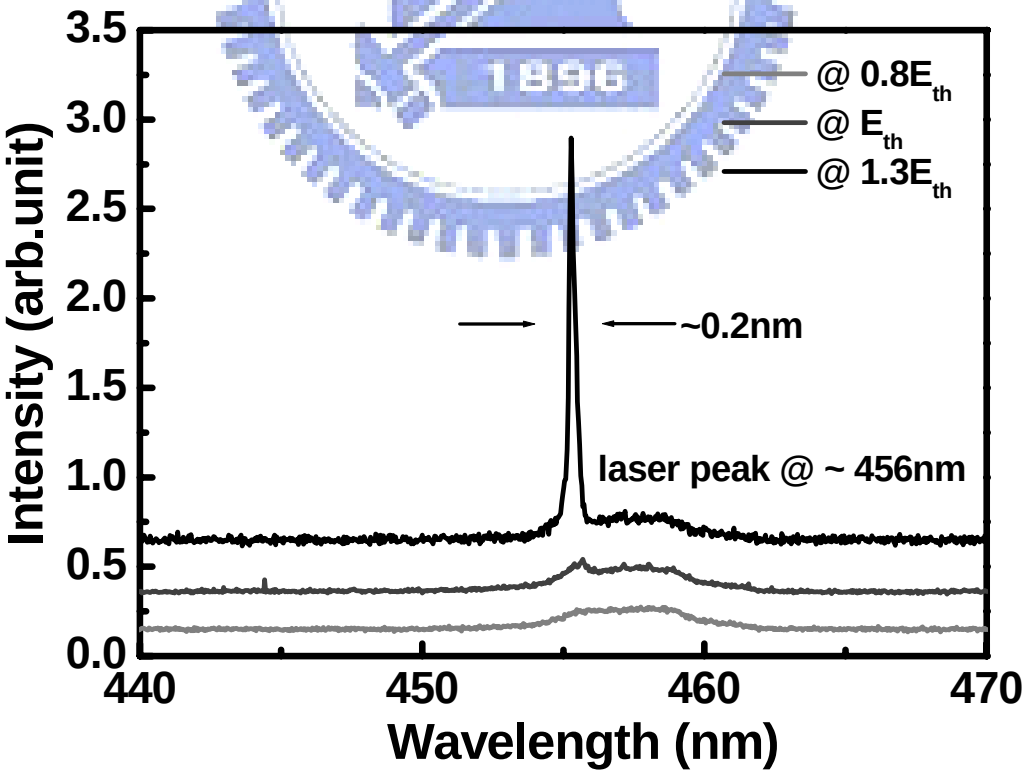

Figure 3.14 Emission spectra of VCSEL under different pumping energy.

Threshold energy density $\mathbf{E_{th}}$	6.4 mJ/cm^2
The reflectivity of the top mirror at 355nm $\mathbf{R_{355}}$	40%
The absorption (coefficient) of the p-GaN at 355 nm $\mathbf{A_{355}}$ ($\boldsymbol{\alpha_{GaN}}$)	86.5% (10^5 cm^{-1})
The quantum efficiency $\boldsymbol{\eta}$	10% [Science, **285**, 1905]
The effective cavity length $\mathbf{L_c}$	1.6μm
The absorption coefficient of GaN at lasing wavelength $\boldsymbol{\alpha_i}$	100 cm^{-1}
The number of quantum wells $\mathbf{N_w}$	10
The width of each quantum well $\mathbf{L_w}$	3 nm
The reflectivity of the top mirrors $\mathbf{R_1}$	99%
The reflectivity of the bottom mirrors $\mathbf{R_2}$	99%

Table 3.1 Parameters for the estimation of material gain.

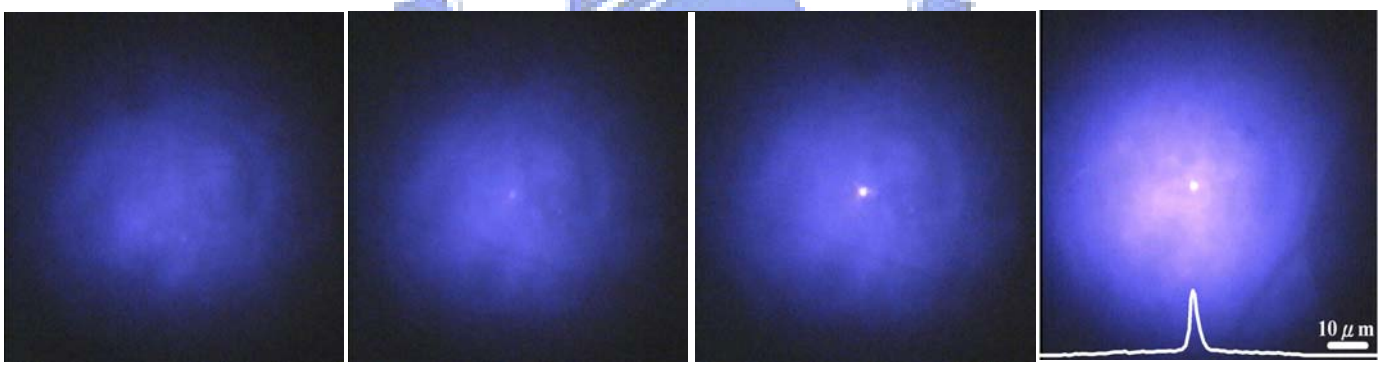

Figure 3.15 Emission images of nitride-based VCSEL under different pumping energy.

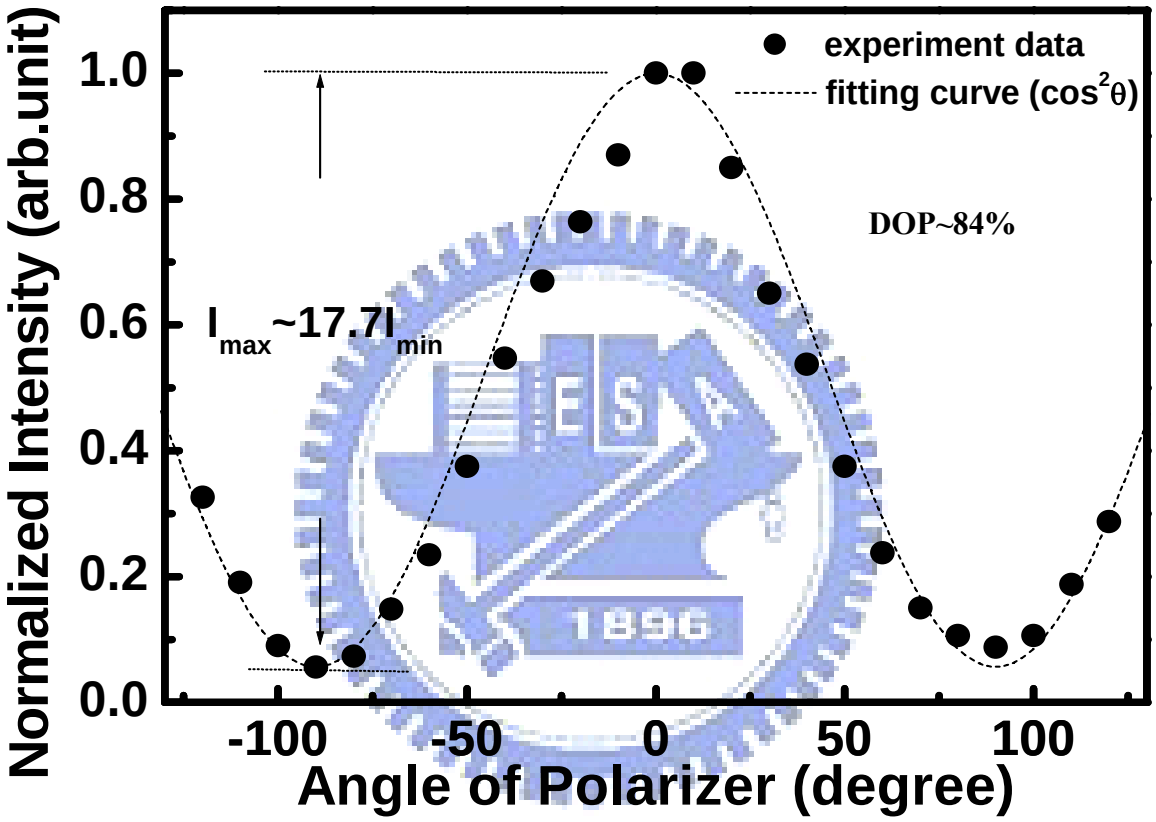

Figure 3.16 The laser emission intensity of VCSEL as a function of the angle of the polarizer at the pumping energy of $1.71E_{th}$.

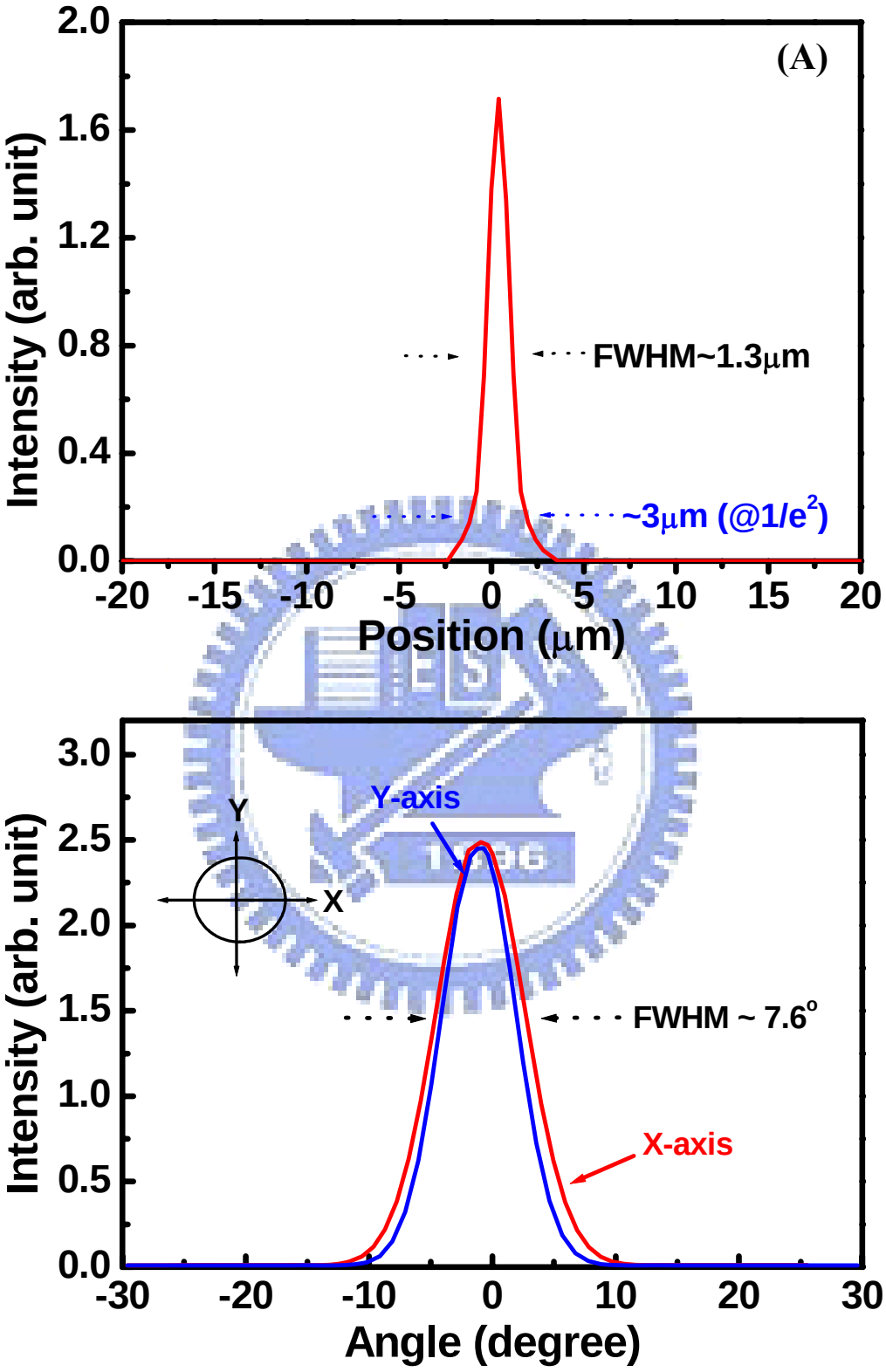

Figure 3.17 (A) Near-field intensity distribution and (B) Far-field emission pattern of the laser spot.

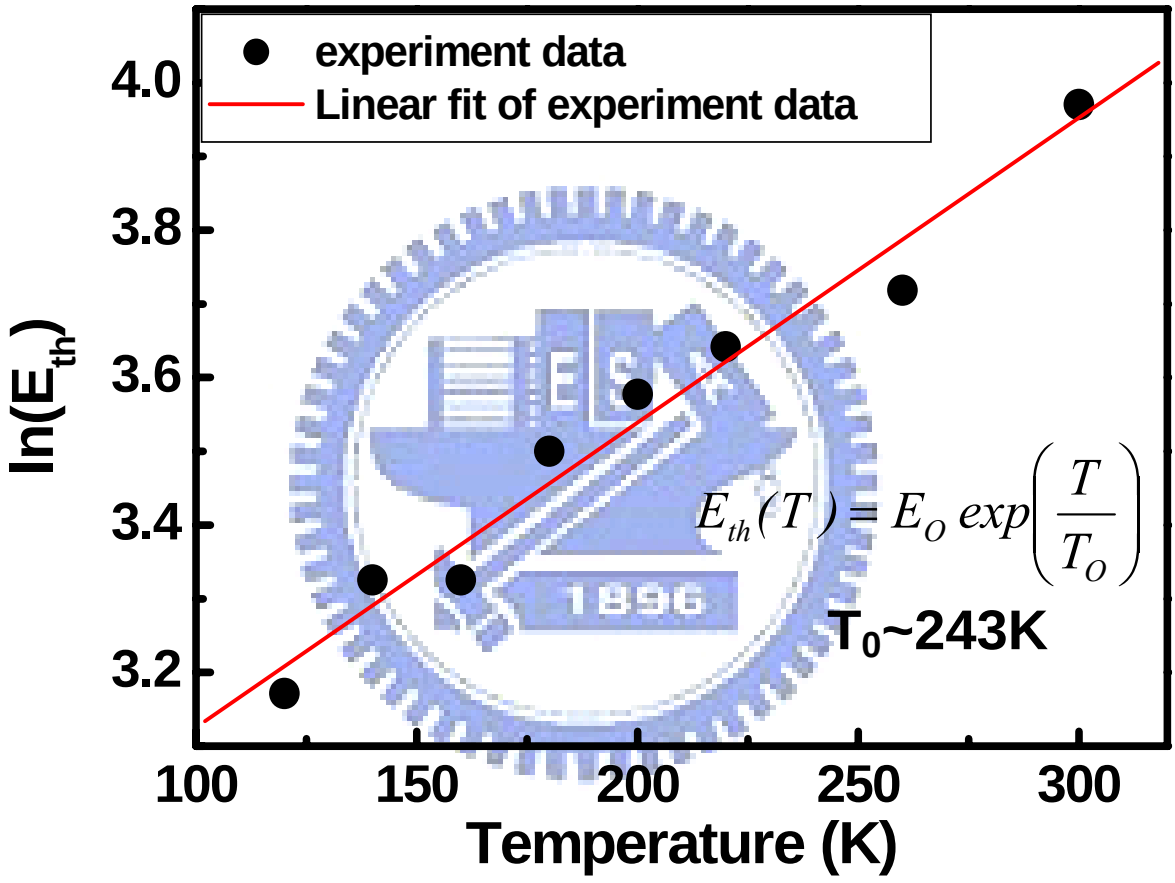

Figure 3.18 Semi natural-logarithm plot of the dependence of the threshold pumping energy (lnE_{th}) on the operation temperature.

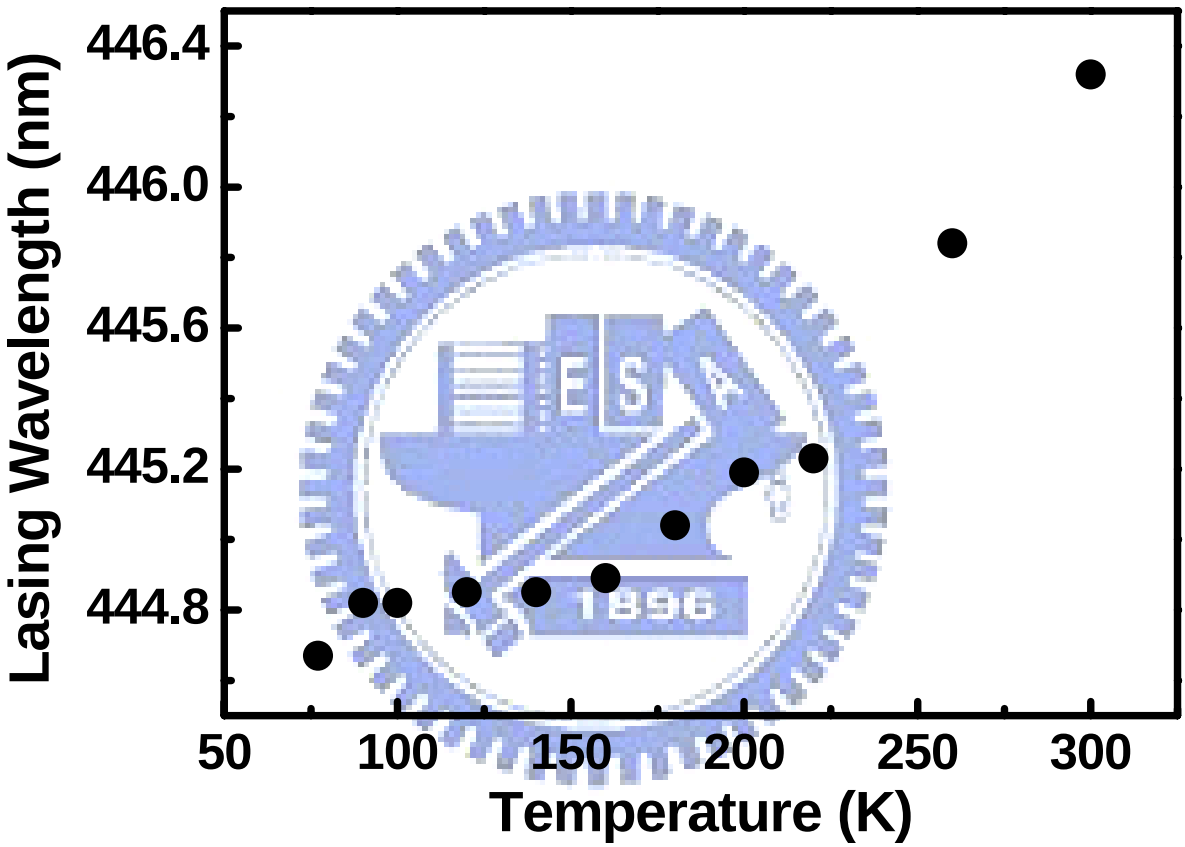

Figure 3.19 The lasing wavelength of nitride-based VCSEL as a function of temperature.

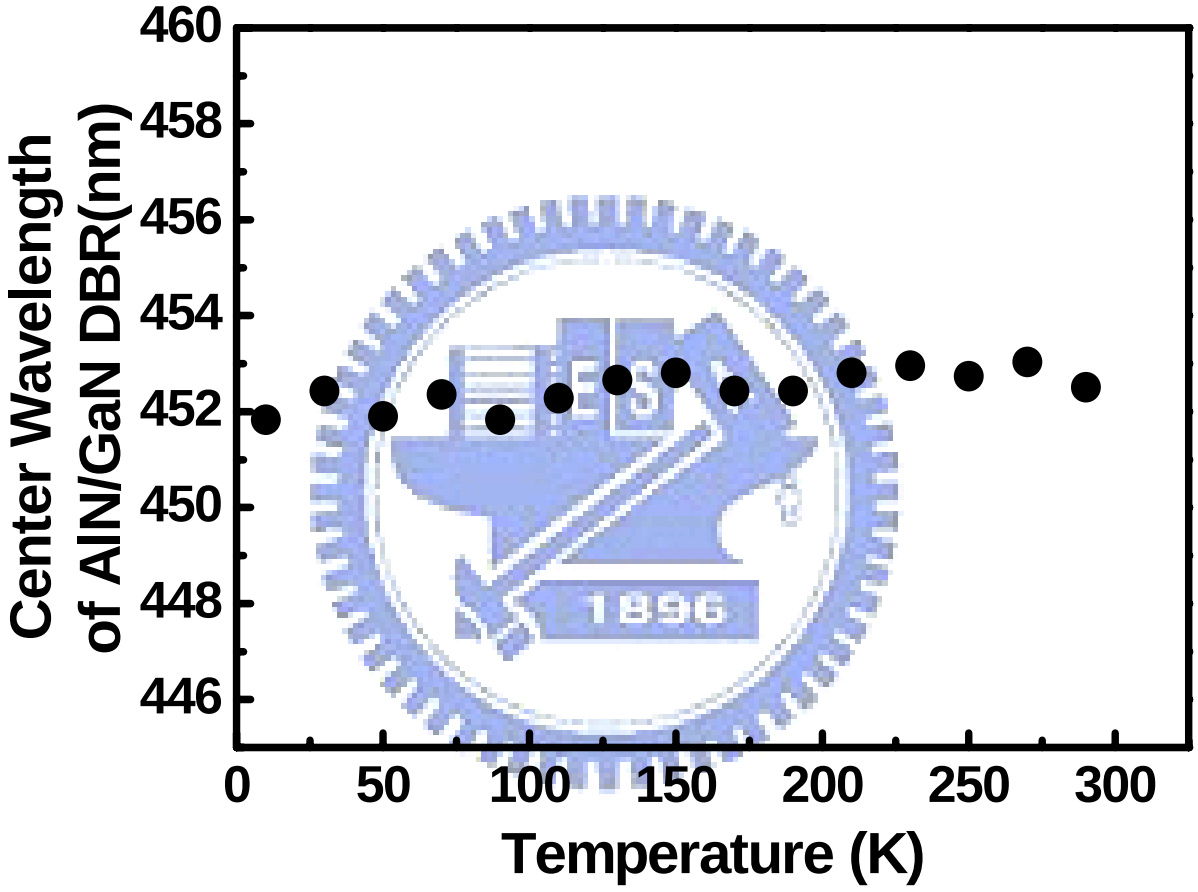

Figure 3.20 The center wavelength of AlN/GaN DBR as a function of temperature.

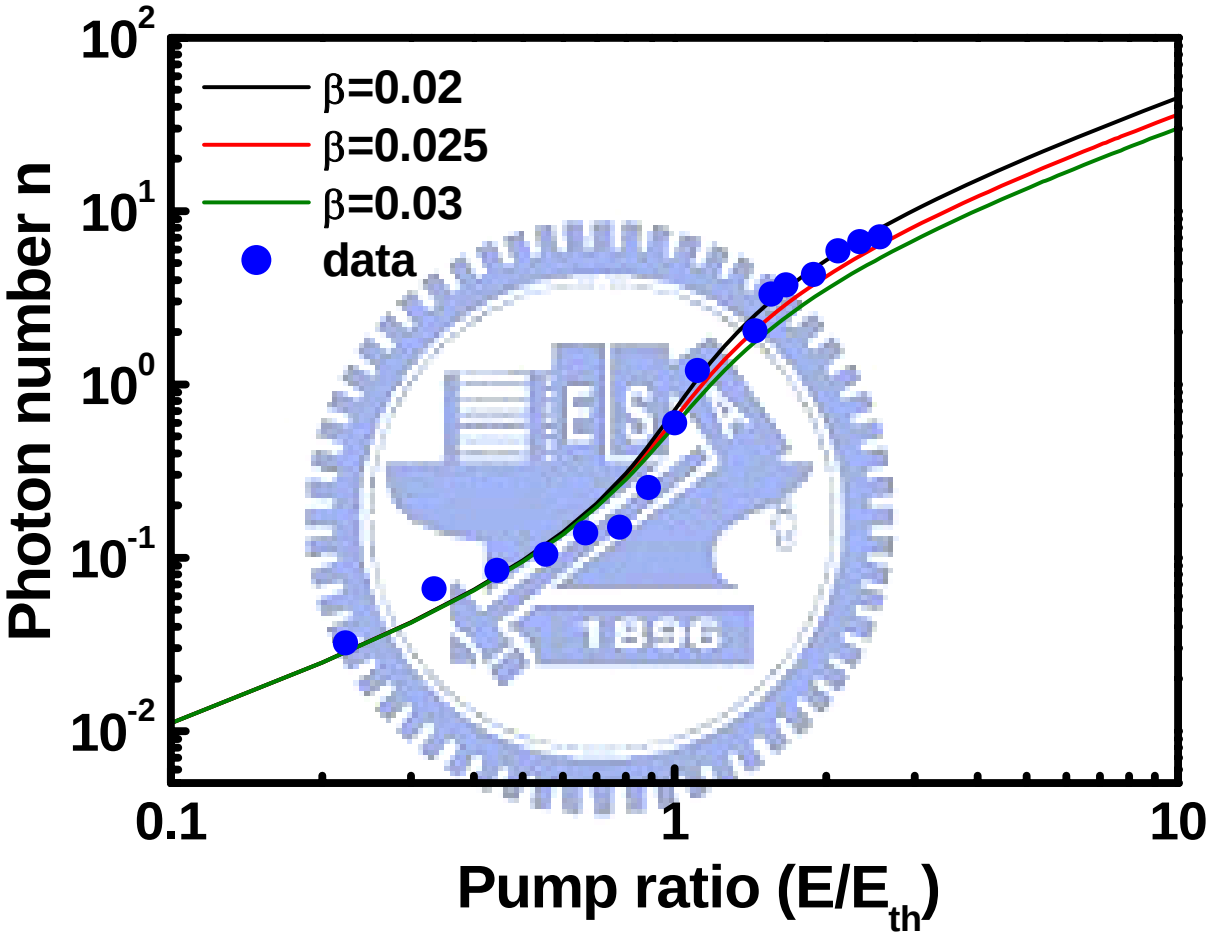

Figure 3.21 Photon numbers as a function of pump ratio. The solid lines are fitting curves with β values of 0.02, 0.025, and 0.03, and the dots are experiment data.

Chapter 4

Effects of Inhomogeneous Gain on Lasing Action of Nitride-based VCSELs

In chapter 3, we discussed the lasing properties of the optically pumped nitride-based VCSEL. We observed the laser was a spot with few micro-meters. This hinted the inhomogeneous gain actually exists in our structure and causes some effects. Therefore, in this chapter, we further discuss and investigate the specific lasing conditions happening on nitride-based VCSEL using optical pumping. We observe multiple lasing spots and stable transverse modes.

4-1 Inhomogeneous Spontaneous Emission Intensity of Nitride-Based VCSELs

Figure 4.1 shows the spontaneous emission intensity distribution of the as-grown sample (as shown in figure 3.8) excited by a He-Cd laser and measured using a scanning optical microscopy system. From the figure, we could observe non-uniform intensity distribution and several bright areas with a size of several micro-meters in the scanning area of 20×20 μm^2. Figure 4.2(A) and (B) shows the wavelength distribution corresponding to figure 4.1 and the emission spectrum of the dotted circle marked in figure 4.2(A), respectively. The emission wavelength distribution was also non-uniform, and the largest difference of emission wavelength at different areas in the figure could be as larger as around 4 nm. The emission spectrum of the dotted circle marked in figure 4.2(A) was centered at around 440.2 nm with a linewidth of around 7 nm. The linewidth is smaller than that of a typical nitride light emitting diode, which is about 20 nm. This means the micro-cavity resonant effect has affected the

emission spectrum emitted from our sample. The cavity mode was also been seen in the measured reflectivity spectrum shown in figure 4.2(B). Therefore, both the intensity and wavelength distribution should include the cavity effect. The inhomogeneous intensity and wavelength distribution hinted the carrier gain and cavity mode are considerably inhomogeneous. The inhomogeneity of cavity modes could be seen from the inhomogeneous emission peak wavelength determined by cavity. To compare figure 4.1 and 4.2(A), the inhomogeneous gain also could be confirmed from those regions emitting the same wavelength but the different intensity. In fact, the inhomogeneous cavity and the inhomogeneous indium composition of InGaN MQWs both were reported [1-3]. The emission intensity from the structure would be higher if the detuning between light emission generated from MQWs and the cavity mode is smaller. In other words, the spontaneous emission of InGaN MQWs at the region with a strong intensity aligns the cavity mode there well. That means those regions with strong intensity would have high gain in strong resonant modes at them.

4-2 Multiple Laser spots phenomenon of Nitride-Based VCSELs

Figure 4.3 shows the emission images of the multiple laser spots. Below threshold, the spontaneous emission was uniform in the pumping region. Then, a lasing spot appeared after the pumping energy was increased above threshold. With the pumping energy increasing, the laser kept brightening and the second laser spot appeared at the center of pumping region above the pumping energy of $1.3E_{th}$ (E_{th} is the threshold energy). The third laser spot was found at the pumping energy of $1.4E_{th}$. The emission spectra under four different pumping energy are shown in figure 4.4. The first lasing emission occurred as the laser spot was observed from the emission image and was centered at 445.2 nm. Then, the second and third laser emission emerged at 446.6 nm and 447.3 nm, respectively. From the section 4-1, we have understood high gain regions in nitride-based VCSEL are dispersive with sizes of just

several micro-meters. These dispersive high-gain regions are responsible to the spot type lasing phenomenon. Besides, the inhomogeneous gain distribution in the nitride-based VCSEL could also cause different lasing thresholds in different regions. This specific property further results in the multiple laser spots phenomenon of nitride-based VCSEL.

4-3 Well-Organized Mode Patterns of Nitride-Based VCSELs

Besides the phenomenon of multiple laser spots, we also found well-organized mode behaviors in nitride-based VCSEL. Figure 4.5 shows the observed lasing emission images and their intensity distributions in the four different regions. Above the threshold energy, the four different mode patterns similar to TEM_{00}, TEM_{01}, TEM_{02} and TEM_{11} were observed in these four regions, respectively. From the light intensity distribution, we could clearly define the mode size of each transverse mode pattern. The size of fundamental mode was about 1.05μm. Compared to the fundamental mode, the size of other mode patterns was larger. As shown in the figure, the size of mode patterns similar to TEM_{01}, TEM_{02}, and TEM_{11} was about 4.4, 4.4, and 6.5μm, respectively. It is interesting these modes patterns individually occurred at different regions. The different preference for emitted mode pattern in different regions should be very special compared to other laser diodes. In the following, we mainly discuss the behaviors of fundamental mode (TEM_{00}) (region I) and TEM_{01} (region II) mode patterns because the behaviors of other mode patterns were similar to those of TEM_{01}.

Figure 4.6 and 4.7 shows the threshold characteristics of pumping region I and II on GaN VCSEL sample, respectively. The intensities of both regions rapidly increase as the pumping energy density was increased. The inserted photos describe the transverse mode patterns from these two regions of GaN VCSEL. As shown in figure 4.6, a lower pumping threshold could be obtained in region I on GaN VCSEL sample compared to that of another. In this region, the distribution of emission intensity in pumping region was uniform below threshold energy. As the pumping energy density was increased above threshold energy density of about 2.8mJ/cm^2,

one single emission spot was observed in the center of the pumping region. This single-spot lasing phenomenon has been discussed in the previous chapter and could be characterized as the fundamental mode. However, in another pumping region (region II), we could observe an obviously different emission pattern above pumping energy density of about 6 mJ / cm^2 (see figure 4.7). The emission pattern exhibited two separated intense peaks, which could be characterized as TEM_{01} mode. The mode pattern stably existed and its intensity significantly increased over the range of pumping energy density from 6 to 8 mJ / cm^2. The stable transverse mode pattern with pumping energy increasing is a peculiar phenomenon. The results show that as the photons oscillated with specific gain distribution there would be only some transverse mode to appear and keep intensifying at high pumping energy. This stable mode emission could be attributed the short carrier diffusion length that nitride-based matrials have. The carrier diffusion lengths of GaN and InGaN were reported to be around 200 nm [4, 5]. This short carrier diffusion length would cause the carrier not easy to flow away and be shared by other high order modes.

Figure 4.8 and 4.9 shows the emission spectra of the pumping region I and II under different pumping energy, respectively. At pumping region I, a laser emission peak located at 411.77 nm was found above the pumping energy density of 2.8 mJ / cm^2. With the increasing of pumping energy, the intensity of the laser emission rapidly increased. At another region, we also observed an emission peak supposed to be fundamental laser emission located at 412.9nm as the pumping energy was around 3 mJ/cm^2. However, as energy density was beyond 3 mJ / cm^2, another laser emission peak located at 411.73 nm appeared and its spectra intensity was gradually increased to compete with the peak at 412.9 nm within the pumping energy density of 3 and 6 mJ / cm^2. As the pumping energy was above 6 mJ / cm^2, the emission intensity of TEM_{01} mode suddenly shows a dramatic increase and the mode pattern became clear. It might imply the gain in this lasing area was shared and competed by two transverse modes between the pumping energy density of 3 and 6 mJ / cm^2 and then TEM_{01}

mode became dominant lasing mode beyond the pumping energy density of 6 mJ / cm^2. The gain sharing and competition could further increase the threshold pumping energy. The mode competition also could be seen at other regions on our sample. Figure 4.10 shows the emission spectra of nitride-based VCSEL emitting two kinds of transverse mode patterns, TEM_{01} and TEM_{11}, at the same region with the same pumping energy. As the image of mode pattern was TEM_{01}, two emission peaks were observed in the emission spectrum. The stronger emission peak was at 413.9 nm and another was at 413.3 nm. As the mode pattern became to be TEM_{11}, the emission peak at 413.3 nm suddenly became dominant. It means the emitting wavelengths of co-existing TEM_{01} and TEM_{11} were about 413.3 nm and 413.9 nm, respectively.

To understand the origin of the mode behavior of nitride-based VCSEL, we further measured the PL emission intensity distribution to realize the gain distribution of our sample. Figure 4.11 shows the intensity distribution of photoluminescence at four different regions shown in figure 4.5. The PL intensity distributions at these four different regions were very different but similar to the laser mode patterns they emitted. The light intensity of the bright spot was about two times stronger than that of the neighborhood. As discussed in the section 4-1, these bright regions should embed high gain at corresponding cavity modes. Figure 4.12 shows the PL spectra of three places marked in the photo shown in the inset. Obviously, two bright spots both show similar emission wavelength of around 412nm with linewidth of around 1.6nm (the quality factor is 257.5). On the contrary, the neighbor place (place 3) shows a shorter wavelength of around 409.5nm with a broader linewidth of around 3nm (the quality factor is 136.5). This further confirmed there should be higher gain or lower loss in these bright spots, and they could result from the well alignment of the cavity mode and the gain profile and the higher reflectivity of DBR. In fact, the gain distributions at these four lasing regions are quite similar to their mode patterns. This suggests the lasing modes should have high gain and low threshold at these regions due to the highly overlap between gain

profiles and mode patterns.

Furthermore, for an almost planar resonator, such as VCSEL with DBRs, the mode spaceing is given by[10, 11]

$$\Delta\nu = \frac{c\lambda_0}{2\pi^2 n_{eff}^2 w_0^2} \qquad (1)$$

where n_{eff} is the effective refractive index, and w_0 is the minimum spot size. Considering the mode spacing between TEM_{00} and TEM_{01}, we could estimate the spot size of fundamental mode to be 1.15 μm with n_{eff}=2.0 and λ_0=0.413 μm. Here the effective index is estimated by considering our resonant wavelength and the effective cavity length included 3 λ cavity and DBR penetration depth. Our measured result shows the spot size of fundamental mode is 1.05 μm. This value is almost consistent with the estimated value. However, typically, the higher-order mode size should roughly follows the equation: $w_n = \sqrt{n} w_0$, where n is the mode number. That means the mode size of TEM_{01} would be about 1.6 μm, which is smaller than the measured value. It implies the probability that these mode patterns were just a specific phenomenon resulting from the inhomogeneous gain.

References

1.K. Okamoto, A. Kaneta, Y. Kawakami, S. Fujita, J. Choi, M. Terazima, and T. Mukai, *J. Appl. Phys.*, **98**, 064503 (2005)

2. F. Bertram, S. Srinivasan, L. Geng, F. A. Ponce, T. Riemann, and J. Christen, *Appl. Phys. Lett.*, **80**, 3524 (2002)

3. G. Christmann, D. Simeonov, R. Butté, E. Feltin, J.-F. Carlin, and N. Grandjean, *Appl. Phys. Lett.*, **89**, 261101 (2006)

4. S. J. Rosner,a) E. C. Carr, M. J. Ludowise, G. Girolami, and H. I. Erikson, *Appl. Phys. Lett.*, **70**, 420 (1997)

5. J.S. Speck and S.J. Rosner, *Physica B*, **273-274**, 24 (1999)

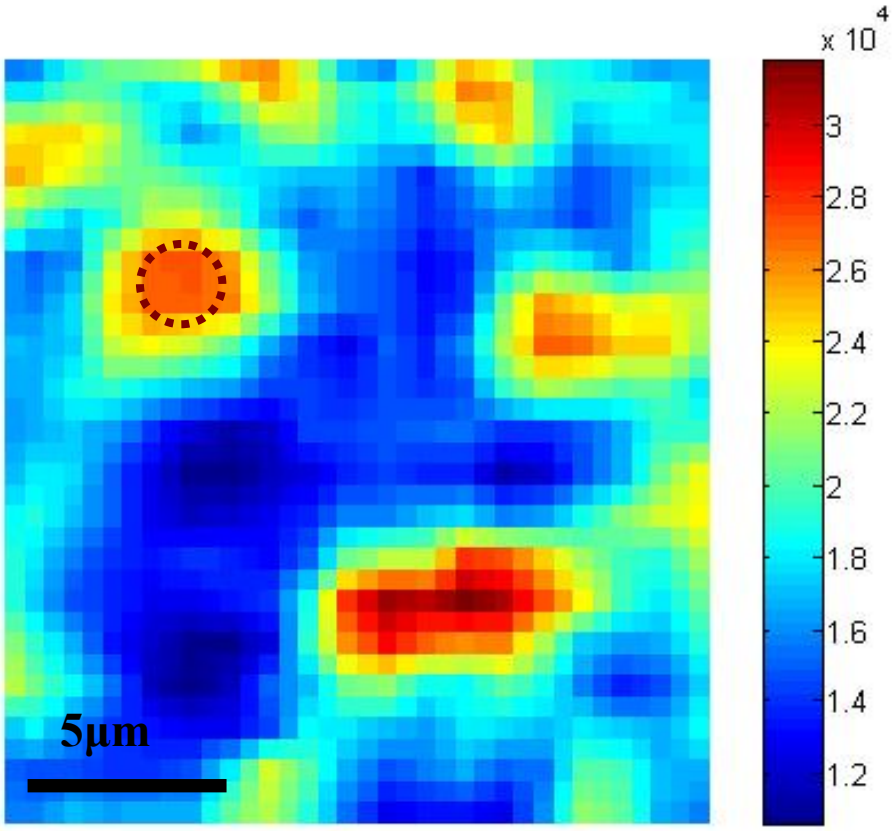

Figure 4.1 The PL intensity distribution of one region on the as-grown sample with a scanning area of 20×20 μm^2.

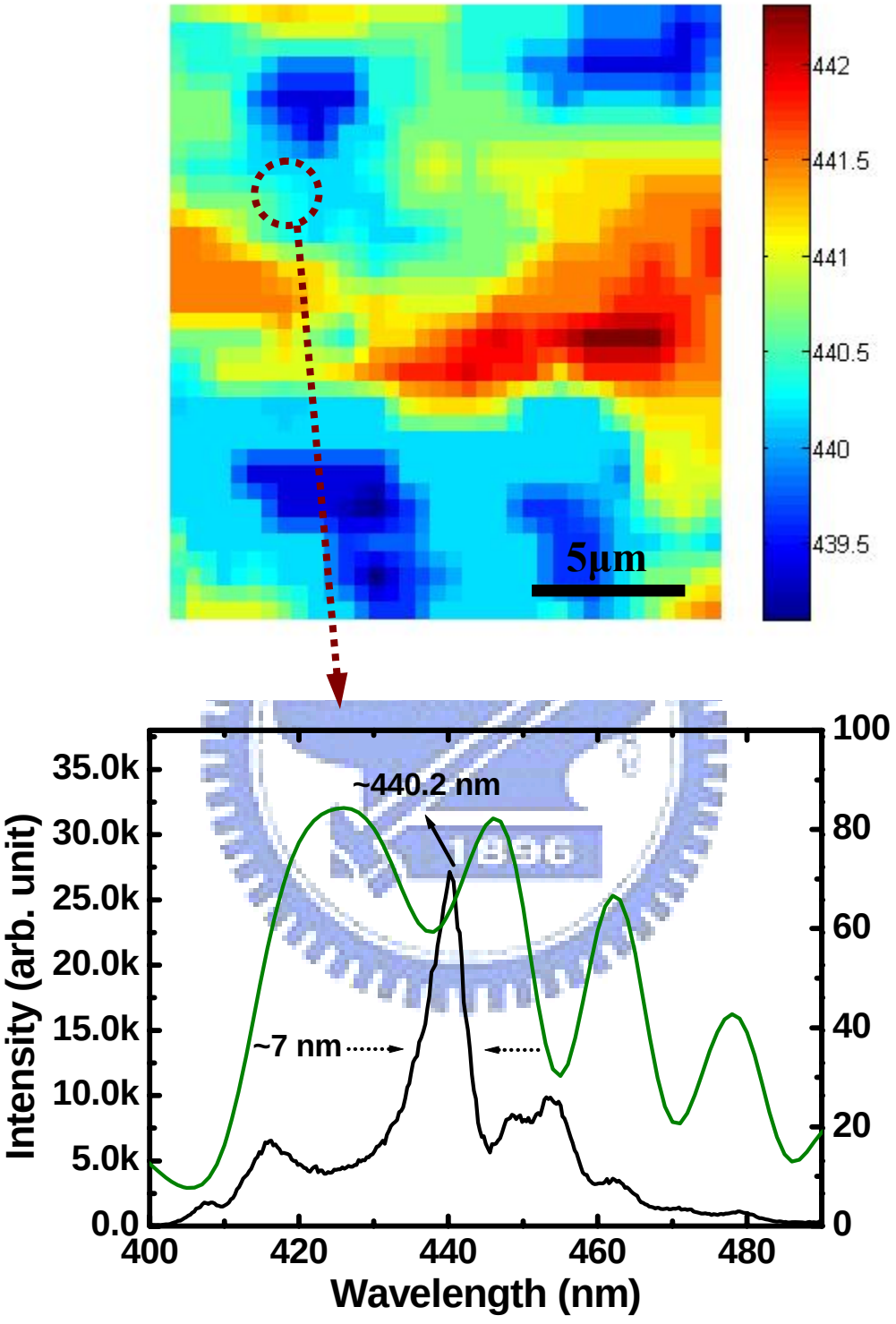

Figure 4.2 (A) The wavelength distribution of the region shown in figure 4.1. (B) The PL spectrum of the dotted circle and the reflectivity spectrum of the region.

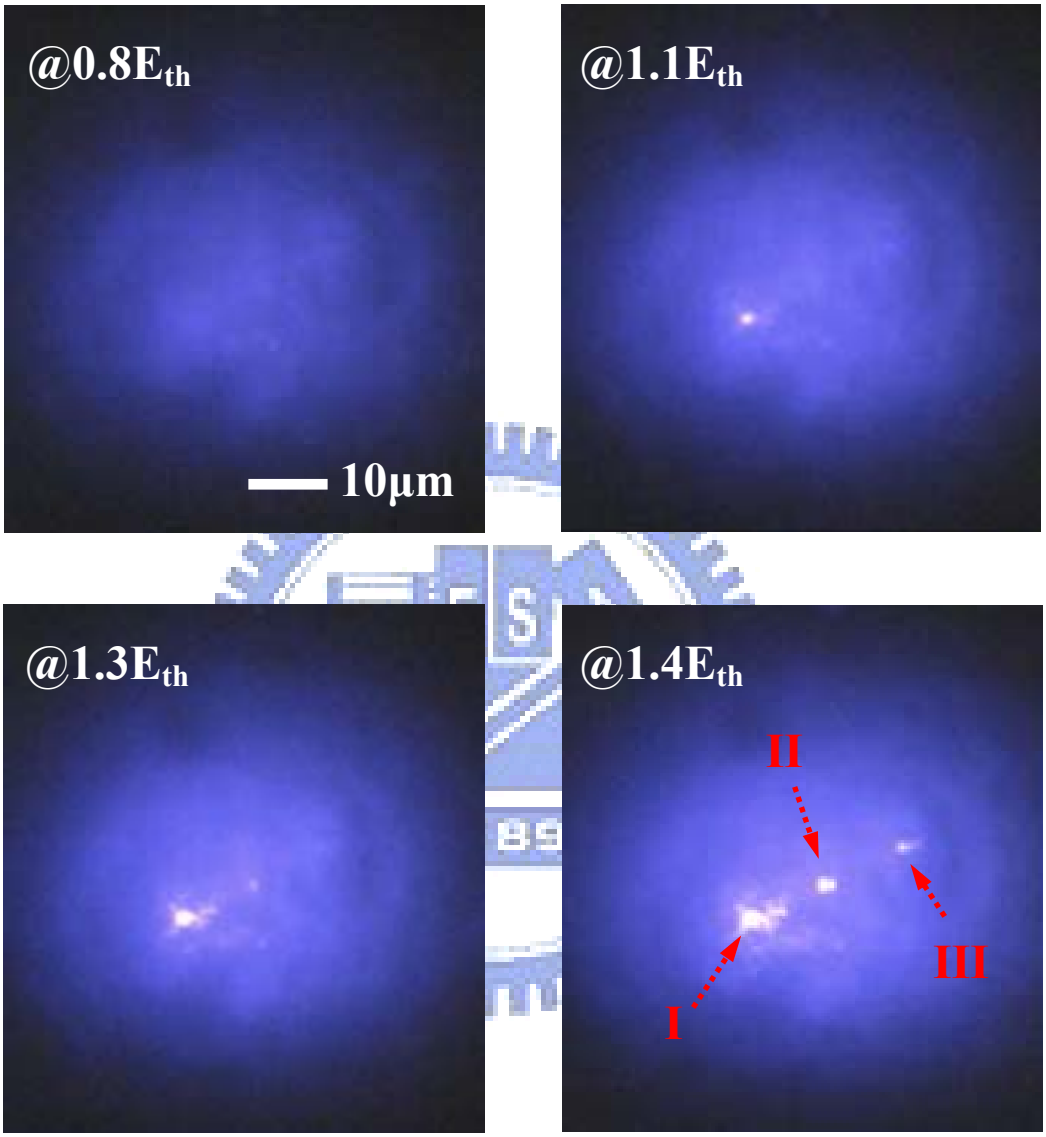

Figure 4.3 Emission images of multiple laser spots under four different pumping energy of 0.8 E_{th}, 1.1E_{th}, 1.3E_{th}, and 1.4E_{th}.

(I)

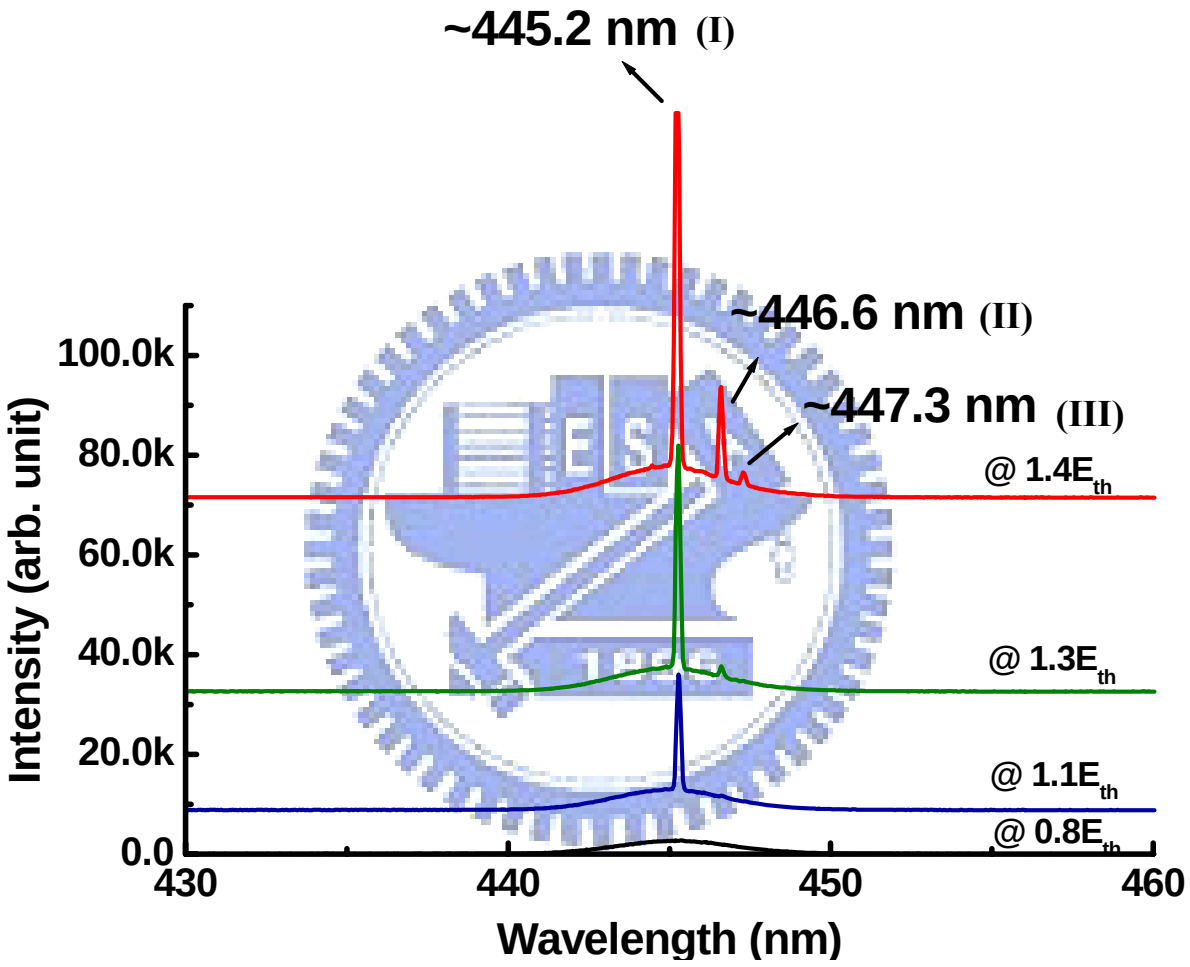

Figure 4.4 Emission spectra of multiple laser spots under four different pumping energy of 0.8 E_{th}, 1.1E_{th}, 1.3E_{th}, and 1.4E_{th}.

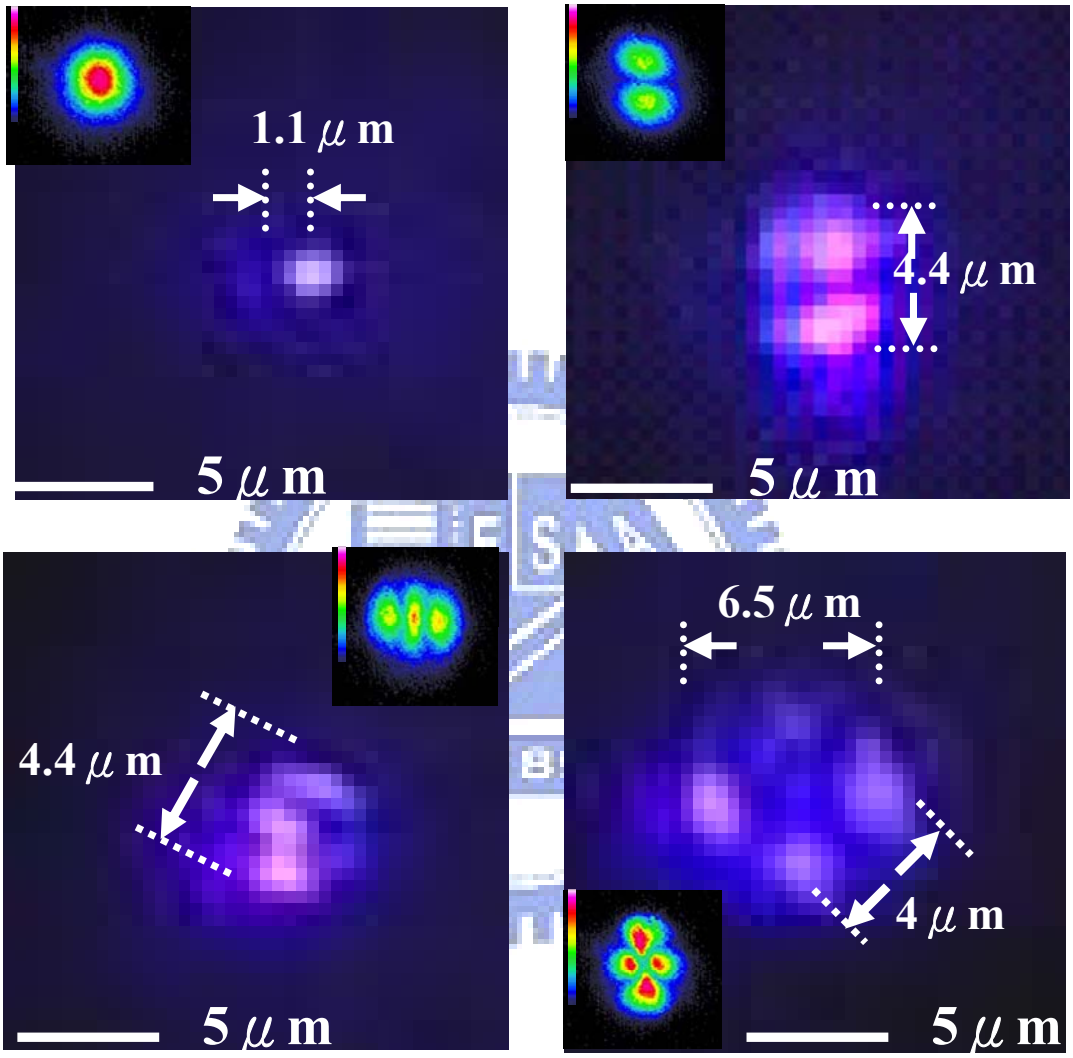

Figure 4.5 Four observed lasing emission images and intensity distributions simialr to TEM_{00}, TEM_{01}, TEM_{02} and TEM_{11} in the four different regions.

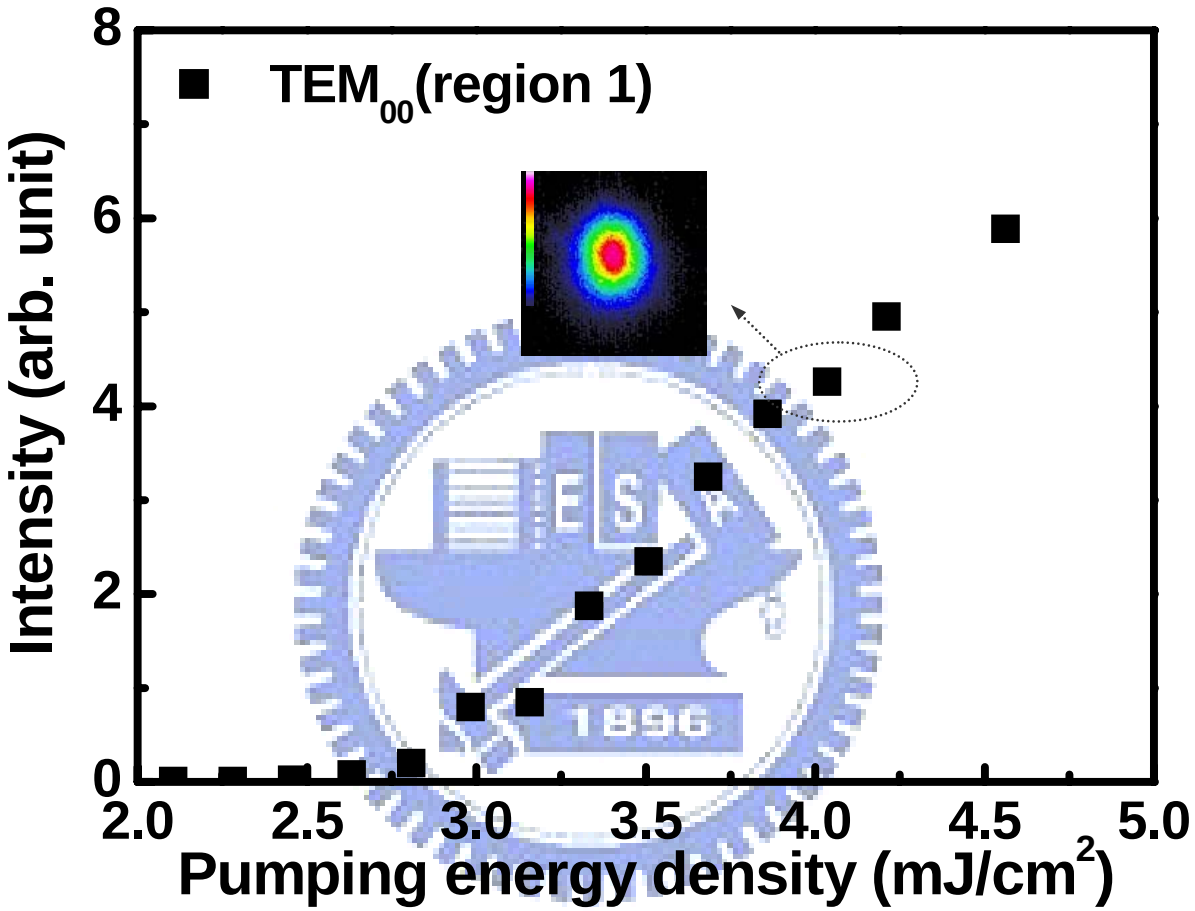

Figure 4.6 The threshold characteristic of pumping region I on GaN VCSEL sample.

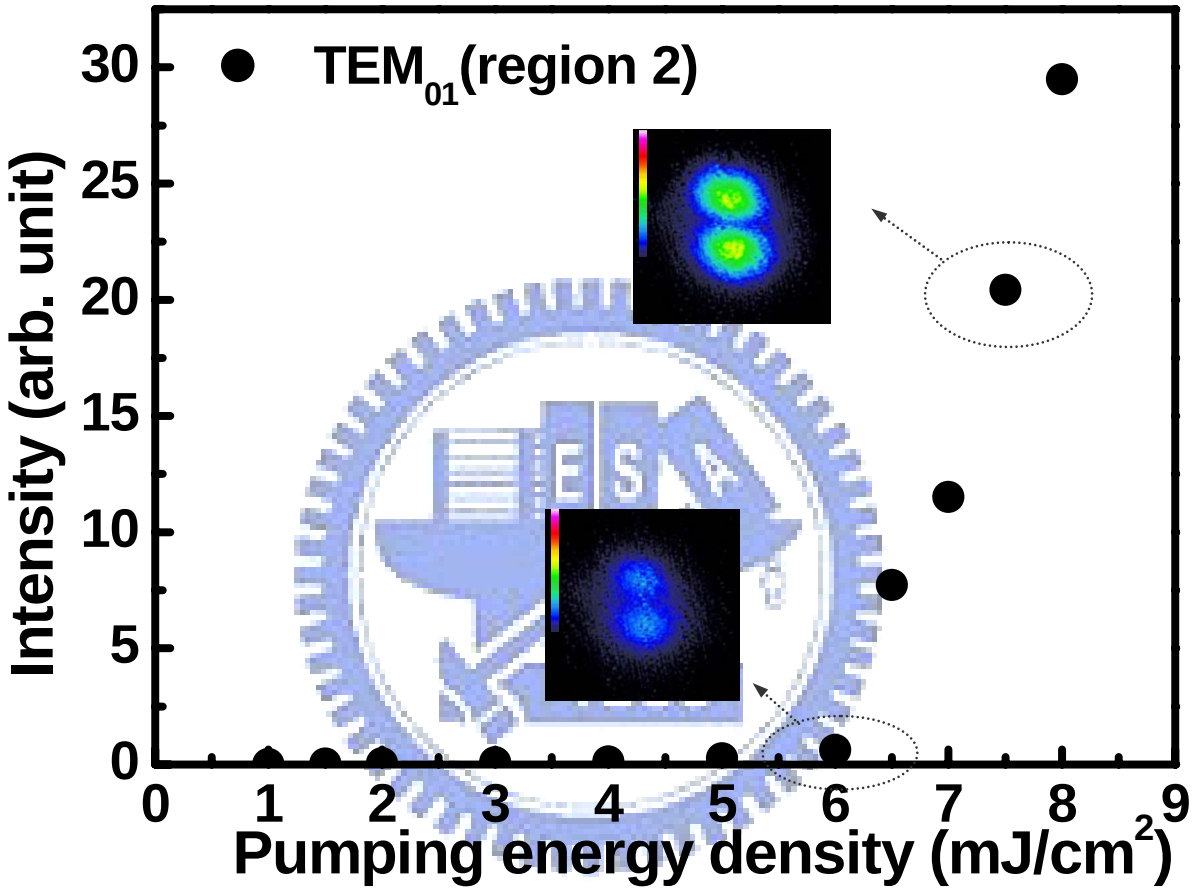

Figure 4.7 The threshold characteristic of pumping region II on GaN VCSEL sample.

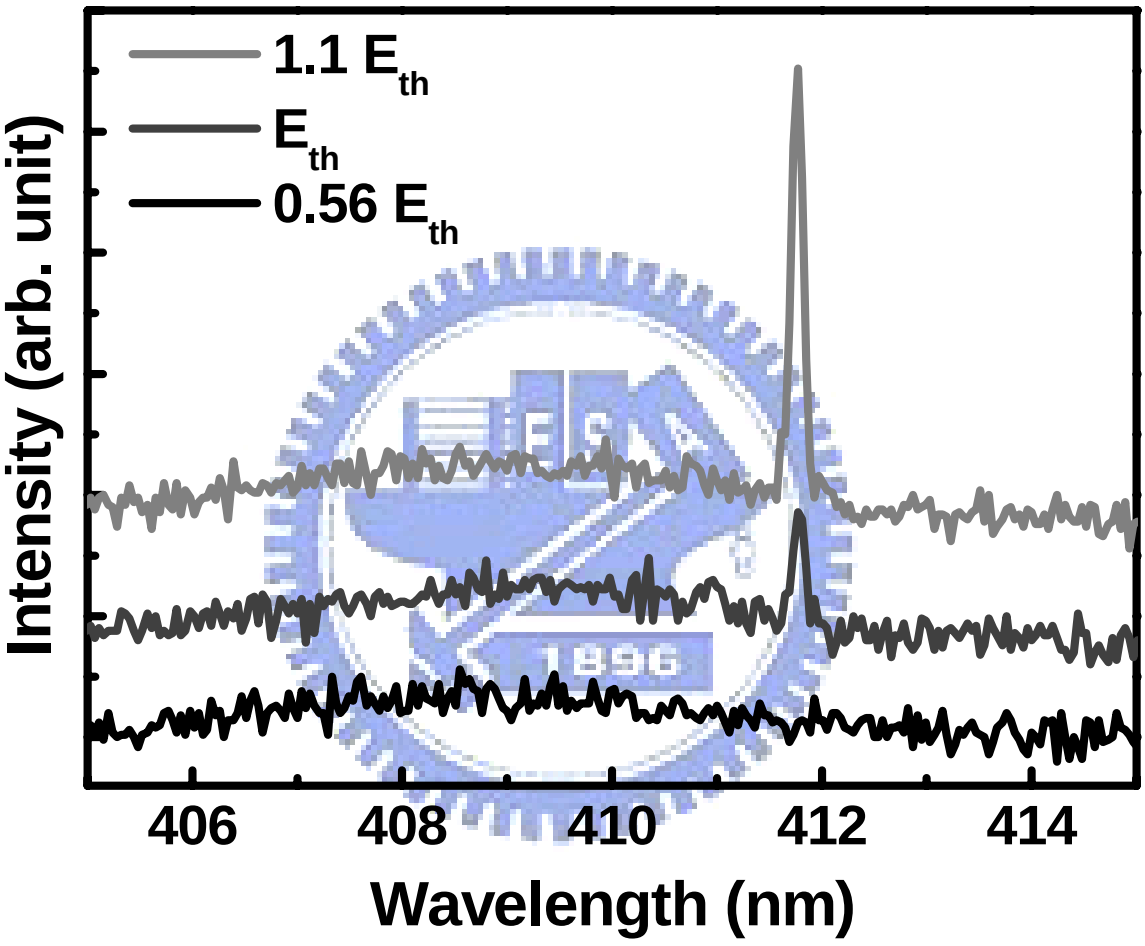

Figure 4.8 Emission spectra of the pumping region I under different pumping energy.

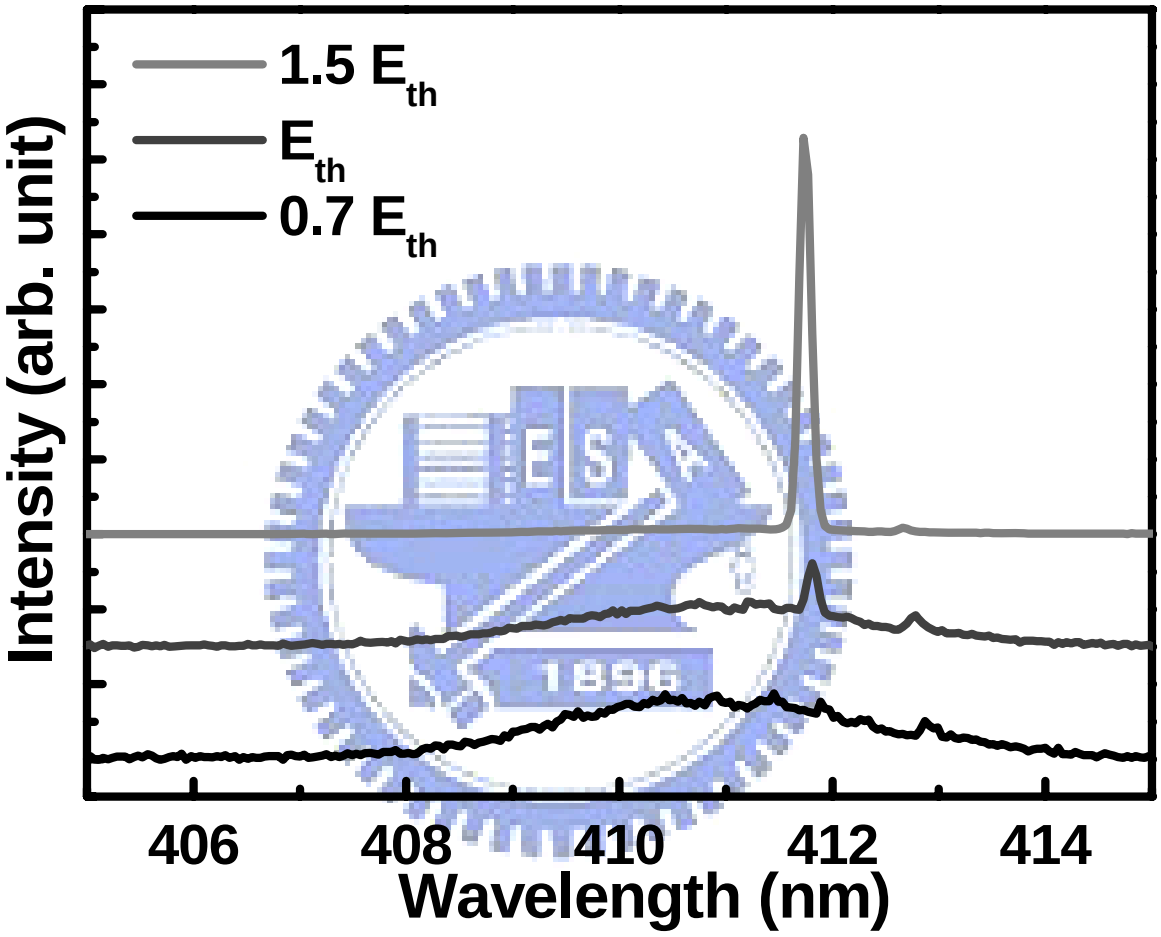

Figure 4.9 Emission spectra of the pumping region II under different pumping energy.

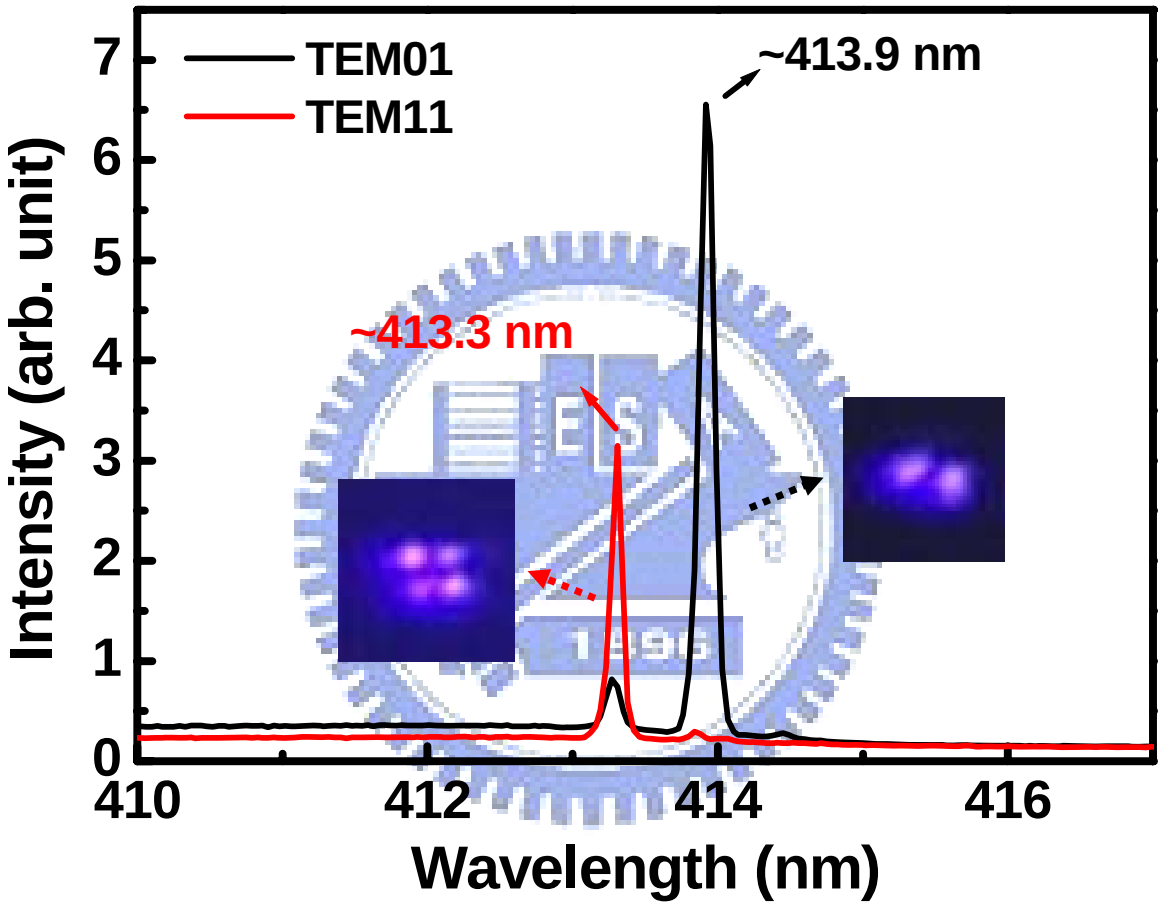

Figure 4.10 Emission spectra of nitride-based VCSEL emitting two kinds of mode patterns, similar to TEM_{01} and TEM_{11}, at the same region with the same pumping energy.

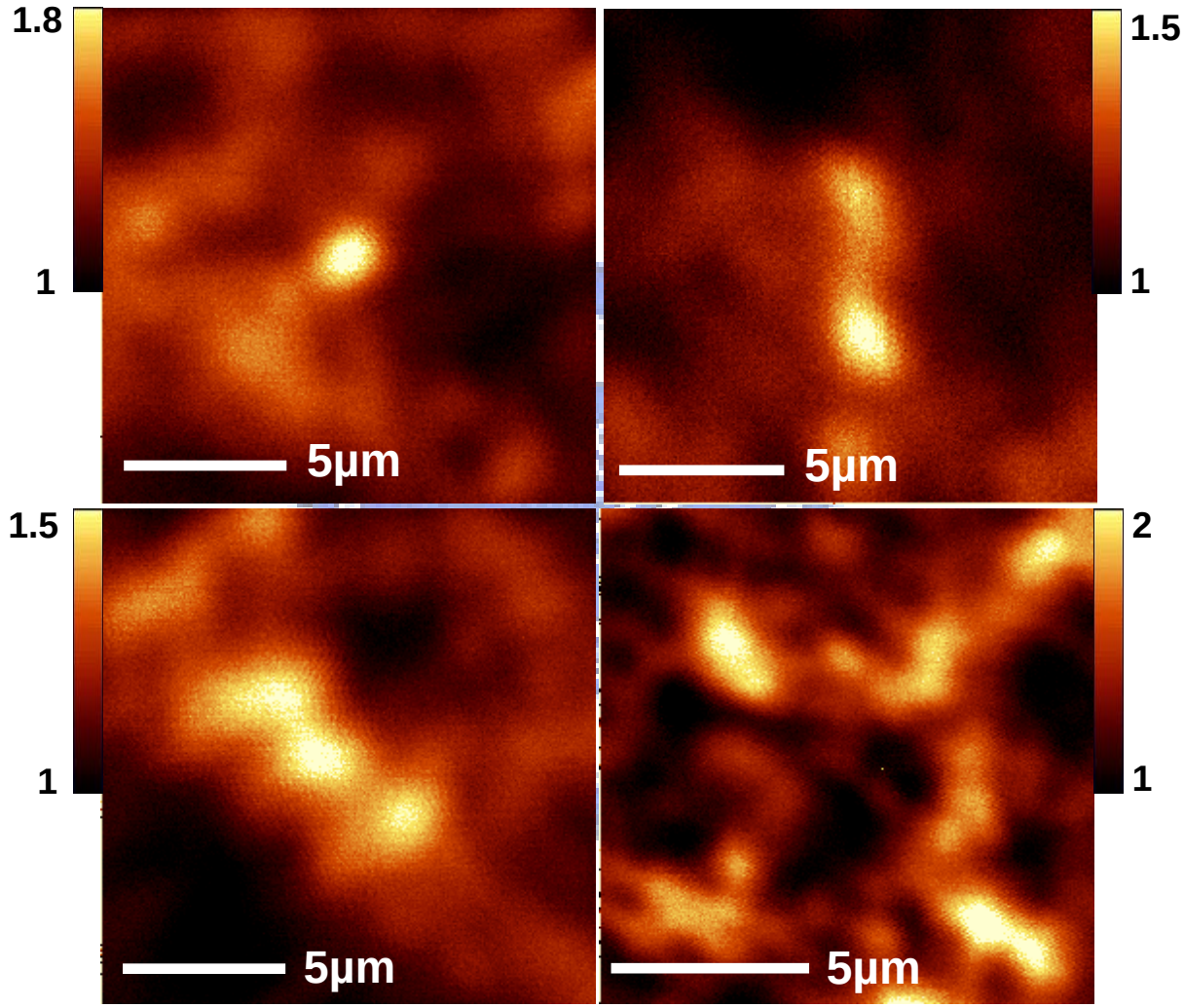

Figure 4.11 PL Emission intensity distributions of four pumping regions shown in figure 4.5.

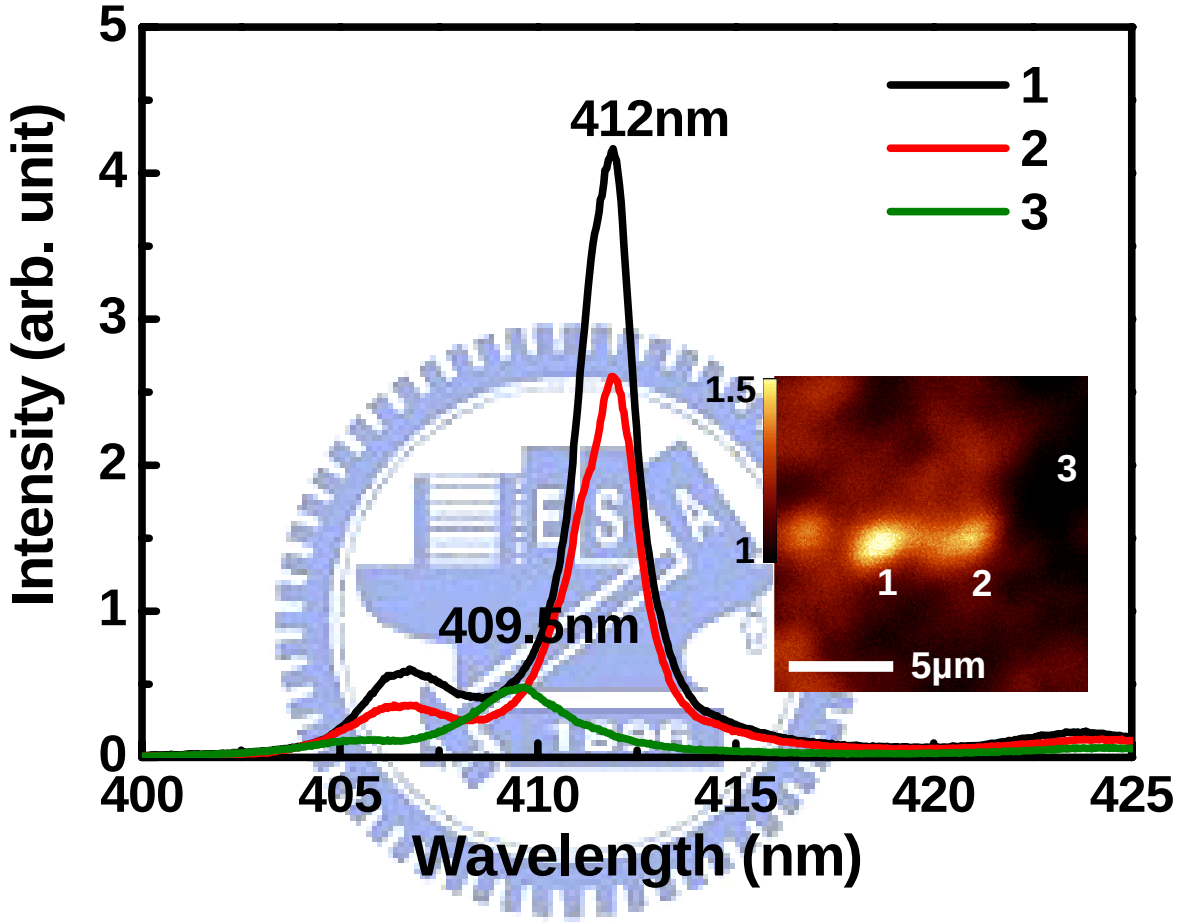

Figure 4.12 PL spectra of three places marked in the photo shown in the inset. The inset is PL emission image of the region emitting TEM_{01}.

Chapter 5

Fabrication and Characteristics of High-Q Micro-Cavity Light Emitting Diodes

With the achievement of optically-pumped nitride-based VCSEL, it has become very hopeful to realize an electron-injected nitride-based VCSEL. In fact, the road toward the electron-injected of nitride-based VCSEL is very rugged. In recent years, some groups started to try to develop nitride-based VCSEL devices and demonstrated a novel device similar to VCSELs, the micro-cavity light emitting diode (MCLED) [1-8]. Song *et al.* demonstrated a vertical-cavity light emitting diode (VCLED) with high-reflectivity dielectric DBRs, using lift-off technique to separate an InGaN *pn*-junction thin film from a sapphire substrate, which led to a complex fabrication process [1]. Diagne *et al.* fabricated a VCLED with a 60-pair $GaN/Al_{0.25}Ga_{0.75}N$ DBR and obtained a narrow linewidth (0.6 nm) emission [2]. This kind of device has several advantages similar to VCSELs, such as circular beam shape, light emission in vertical direction, fully monolithic test and two dimensional arrays. In order to further achieve electron-injected VCSEL, Mackowiak et al. [9] reported the design of possible structures of nitride-based VCSELs, which is a hybrid structure, composed of 4 pairs of the dielectric SiO_2/TiO_2 DBR as upper mirror and 24 pairs of the $AlN/Al_{0.15}Ga_{0.85}N$ DBR as the bottom mirror. This also reveals the hybrid cavity with AlN-based DBR is a strong candidate to realize the laser action of an electron-injected VCSEL.

In this chapter, we establish the fabrication process for an electron-injected nitride-based VCSEL and demonstrate a high-Q nitride-based micro-cavity light emitting diode using the sample described in chapter 3. The fabrication techniques were further improved for reducing the absorption inside cavity and bettering the current confinement. The use of

indium-tin-oxide to substitute Ni/Au as transparent contact effectively reduces the cavity absorption and raises the quality factor of the cavity. The characteristics of the high-Q nitride-based micro-cavity light emitting diode have been also investigated. Furthermore, we use Mg^{+}-implantation to isolate lateral current flow and improve the current confinement.

5-1 Fabrication Processes for nitride-based VCSELs

The processes for a nitride-based hybrid-cavity VCSEL include steps: (1) definition of mesa area, (2) definition of current aperture, (3) coating of transparent contact, (4) deposition of p, n contact, and (4) deposition of top DBR. The transparent contact coated on p-type GaN is currently a commonly-utilized technique in nitride light emitting devices and is important and inevitable for uniform spreading current. However, for a nitride-based hybrid-cavity VCSEL, the transparent contact acts not only a current spreading layer but also an absorption layer because it becomes a part of cavity. This additional absorption would result in a lowering of quality factor of cavity to further increase the required threshold. Therefore, a superior transparent contact for a nitride-based VCSEL must have two important key characteristics, high transparency (low absorption) and low resistivity. The common transparent contacts are nickel (Ni)/gold (Au) and indium-tin-oxide (ITO). Figure 5.1 shows the transmission (T) and reflectivity (R) versus wavelength of Ni/Au (5/5nm) and ITO (300nm) films deposited on glass substrate. These two films were both thermally treated to achieve high reflectivity. The annealing condition of ITO and Ni/Au is 525°C for 10 min and 500°C for 30 min under N_2 ambient, respectively. In terms of the energy conservation theory, the absorption loss of films could be obtained from the equation: A=1-R-T, where A is absorption, R is reflectivity, and T is transmission. From the figure, we could find ITO film has a relatively high R+T (97%) compared with that (80%) of Ni/Au thin film at 460nm. That means the corresponding absorption coefficient of ITO and Ni/Au is about 1015 (cm^{-1}) and 7.5×10^{3} (cm^{-1}), respectively. Obviously, ITO shows a low-absorption performance, only one

seventh of absorption coefficient of Ni/Au, and should be more suitable for the VCSEL than Ni/Au.

The thickness of ITO, which is a part of cavity length, should also be carefully designed to make the cavity in well resonance. In general, the cavity length for photons being in oscillation should be a few 1/2-lambda. It means the thickness of the ITO should be 1/2-lambda or one lambda in optical length. The 1/4-lambda ITO, which could be seen as one layer of DBR, also could be an option. However, the experiment result seems to show the thinner ITO is, the higher sheet resistance it has (sheet resistance of 1/2-lambda ITO is 27.5 ohm/cm^2 and that of one-lambda ITO is 12.65 ohm/cm^2). Accordingly, we choose one-lamda ITO as the transparent contact for the VCSEL, one of micro-cavity light emitters. We used the measured index value (1.93) and calculated geometrical thickness (240nm) of the ITO to simulate the reflectivity spectrum of the full device structure and electric field distribution inside the cavity. The simulation result further confirms the device could be in resonance; moreover, electrons and photons inside could also effectively interact as the thickness of the 240-nm-thick ITO is applied as shown in figure 5.2.

Fabrication of the micro-cavity light emitting diode

Figure 5.3 shows a process flowchart for a nitride-based VCSEL. In this experiment, we used these process steps to fabricate a high-Q nitride-based MCLED. The sample used is the same one discussed in previous chapter (chapter 3) and was grown by a metal-organic chemical vapor deposition system on a polished c-face sapphire substrate. The sample structure composed of a 29-pair AlN/GaN DBR, a 5-λ optical thickness (λ = 460 nm) active *pn*-junction region, ten $In_{0.2}Ga_{0.8}N$(3 nm) / GaN(7 nm) multiple quantum wells, a 660 nm-thick Si-doped n-type GaN and a 120 nm-thick Mg-doped p-type GaN layers. The process of MCLED began with the deposition of a 0.3 μm-thick SiN_x etching mask by plasma enhanced chemical vapor deposition (PECVD) and the definition of mesa region by

photo-lithography. The mesa etching was then performed with Cl_2/Ar as the etching gas in an inductively coupled plasma reactive ion etching (ICP-RIE) system with the ICP power and bias power operated at 13.56 MHz. After removing the etching mask, we re-deposited and patterned a 0.2 μm-thick SiN_x layer to define a current aperture of 50 μm in diameter. Then, a 240 nm-thick layer of ITO corresponding to one λ optical thickness was deposited onto the current aperture region using an e-gun. The ITO was employed as a p-type ohmic contact material and annealed at 525°C for ten minutes under a nitrogen ambient to reduce the contact resistance and increase transparency. Only 2% of absorption was obtained at λ = 460 nm after annealing. The contact between ITO and p-GaN was nearly ohmic, and the contact resistance was about 2×10^{-2} ohm-cm as shown in figure 5.4. The metal contact layers were then patterned by a lift-off procedure and deposited onto samples by electron beam evaporation. Ti/Al/Ni/Au (20/150/20/150 nm) and Ni/Au (20/150 nm) served as the n-type electrode and p-type electrode, respectively. A 30-μm emission aperture was formed by lifting off the p-type metal atop the ITO layer. Finally, an 8-pair Ta_2O_5/SiO_2 DBR (measured reflectivity over 99% at λ = 460 nm) was evaporated as the top mirror to complete the MCLED device. Figure 5.5 shows a schematic diagram of the overall MCLED structure. The SEM images of the fabricated device are shown in figure 5.6 (A) and (B).

5-2 Devices Characteristics

The characteristics of the fabricated MCLED were performed by using a probe station and driven by a Keithley 238 CW current source as shown in figure 5.7. Figure 5.8 shows the current versus voltage and light output power of a fabricated device at room temperature. The turn-on voltage of the MCLED was about 3.5 V, indicating good electrical contact of the ITO transparent layer. The high resistance (530 Ω) of the device is due to non-optimization of doping condition of n-type GaN layer, which further limited device operation at higher current density. The emission images under different injection current are shown in figure 5.9(A). The

device emits blue light, and its intensity rapidly increases with the current increasing. The light output power of MCLED was measured by an integrating sphere with a calibrated large-area Si photodiode at room temperature. The measured MCLED chip (as shown in figure 5.9(B)) was previously mounted onto a metal can and then put into the integrating sphere. As shown in Fig. 5.8, the light output power of the MCLED shows a nearly linear increase with current up to 10 mA without thermal roll-over in this current range. As the current increased beyond 10 mA, thermal roll-over began and the output power started to saturate probably due to the high serial resistance of the device.

The emission light was then collected by a 25 μm-diameter multimode fiber using a microscope with a 40X objective and fed into the spectrometer with a spectral resolution of 0.15 nm. Figure 5.10 shows the emission spectrum of the MCLED operating at three different current, 3 mA, 6 mA, and 10 mA. As the injection current was increased, a single emission peak at 465.2 nm became dominant with rapidly increasing intensity and narrowing linewidth. The variation of the emission linewidth with increasing current is shown in Fig. 5.11(A). The full width at half maximum of the emission linewidth decreased from 0.57 nm to 0.52 nm as the driving current was increased to 10 mA, which is, to our best knowledge, the narrowest linewidth recorded for GaN-based MCLEDs. The narrowest the previous report was about 0.6 nm [1, 2]. From the emission peak wavelength at λ = 465.2 nm and the emission linewidth $\Delta\lambda$ = 0.52 nm, the cavity Q is estimated by $\lambda/\Delta\lambda$ to be ranging from 816 to 895. Since the cavity Q formed by our vertical cavity with both high reflectivity DBRs (R = 99% and 99%) and ITO current spreading layer was calculated to be about 900 without taking into account the absorption in the InGaN/GaN *pn*-junction region, the narrowing linewidth observed represents that the active region was approaching the transparency condition before lasing. The possibility of a GaN-based VCSEL could be realized by future optimization of higher DBR reflectivities and ITO transparency, lower resistive heating and better lateral mode confinement. In comparisons to conventional LEDs with a spectral linewidth of about 20 nm,

our high-Q VCLED has demonstrated a rather coherent emission. Figure 5.11(B) shows the emission peak wavelength as a function of current, which was almost invariant with increasing injection current. The emission peak wavelength as a function of temperature was also measured and shown in figure 5.12. The stable peak wavelength of the nitride-based MCLED, compared to that of normal nitride light emitting diodes, demonstrates a potential in temperature-insensitive applications. These results indicate that our high-Q MCLED has a stable emission wavelength and narrow linewidth property.

5-3 Fabrication Technique for Current Confinement - Implantation

The ion implantation and oxidation are two typical techniques for current confinement of laser devices. Ion implantation is relatively easy and stable method between these two techniques, especially for nitride devices, because the oxidation of GaN could only be achieved using a special process, photo-enhanced- chemical oxidation. In this section, we demonstrate the current confinement technique, magnesium ion (Mg^+) implantation, for nitride-based micro-cavity light emitters, for example, VCSEL. The energy and dose of Mg^+ implantation used in this experiment were 80KeV and 2×10^{15} cm^{-2}, respectively. We simulated the distribution of implanted ion inside our structure (as-grown sample shown in chapter 3) after the implantation using a software, TRIM. The result shows the ion range would be about 80nm which is smaller than the thickness of p-GaN (~120nm); however, some of ions implanted could go deeper and damage the active region. In order to avoid the ions damaging the active region of our structure, we further deposited SiNx film onto the sample surface to be a buffer layer. Figure 5.13(A) and (B) shows the simulation and secondary ion mass spectrometry (SIMS) data of Mg^+ ion distribution inside the implanted sample with 100nm-thick SiNx buffer layer, respectively. The simulation profile shows ions could be gathered at p-GaN but almost not harm the active region. The actual ion distribution inside was further confirmed by SIMS. The ion range measured was as deep as 15nm from the top

surface of p-GaN layer and the distribution was almost consistent with the simulation result.

The sample used in this experiment is similar to the structure previously showed. The process of Mg^+-implanted MCLED began from the definition of mesa region which formed by the photo-lithography and the ICP dry etching. The 100nm-thick SiNx film was then deposited as a buffer layer using PECVD system. The sample was patterned to define the current aperture and coated Au metal served as bombardment mask using E-gun evaporator before implantation. The aperture size defined were 15 μm, 20 μm, 25 μm, 30 μm, 35 μm, and 40 μm. The implantation was carried out using 80keV Mg ions with a dose of 2×10^{15} cm^{-2}. Then, we used acid solutions, KI and BOE, to remove Au and SiNx film, respectively. As shown in figure 5.14, the implantation region on sample could be seen clearly. The final was the deposition of 240nm-thick ITO served as transparent contact, and the Ti/Al/Ni/Au (20/150/20/150 nm) and Ni/Au (20/150 nm) served as n-type and p-type electrode, respectively,

Figure 5.15(A) shows emission images of Mg^+-implanted MCLEDs with six different aperture sizes after deposition and annealing of ITO. We could clearly find blue light to emit from defined current apertures of those devices. Figure 5.15(B) further shows a high-magnification emission image of the device with current aperture of 40 μm. The blue light obviously existed in the aperture region only. This confirms the Mg^+ implantation can provide effective current confinement for nitride-based micro-cavity light emitters. Furthermore, the emission image of the fabricated device with 40 μm aperture also reveals the light could only emit from the aperture due to well current confinement as shown in figure 5.15(C). The current-voltage (I-V) characteristics of the implanted and conventional devices are both measured and shown in Figure 5.16. The turn-on voltage of both MCLED was about 3.9 V. However, the resistivity of the implanted MCLED is about 170 Ω which is slightly higher than that (~120 Ω) of conventional one. This higher resistivity of the implanted device might caused by the crystal destruction resulting from the ion bombardment. Of course, the

strictly confined injection area of the implanted MCLED could also be one of reasons to cause higher resistivity because the current injected into the conventional MCLED would diffuse to result in a larger injection area than that we defined (The smaller aperture is the larger resistivity would be resulted in.).

References

1. Y. K. Song, M. Diagne, H. Zhou, A. V. Nurmikko, R. P. Scheider, Jr, and T. Takeuchi, *Appl. Phys. Lett.*, 77, 1744 (2000)

2. M. Diagne, Y. He, H. Zhou, E. Makarona, A. V. Nurmikko, J. Han, K. E. Waldrip, J. J. Figiel, T. Takeuchi, and M. Krames, *Appl. Phys. Lett.*, 79, 3720 (2001)

3. N. Nakada, M. Nakaji, H. Ishikawa, T. Egawa, M. Umeno, and T. Jimbo, *Appl. Phys. Lett.*, 76, 1804 (2000)

4. F. B. Naranjo, S. Fernandez, M. A. Sanchez-Garcia, F. Calle, and E. Calleja, *Appl. Phys. Lett.*, 80, 2198 (2002)

5. M. Diagne, Y. He, H. Zhou, E. Makarona, A. V. Nurmikko, J. Han, T. Takeuchi, and M. Krames, *phys. stat. sol. (a)*, 188, 105 (2001)

6. M. Arita, M. Nishioka, and Y. Arakawa, *phys. stat. sol. (a)*, 194, 403 (2002)

7. B. Roycroft, M. Akhter, P. Maaskant, P. D. Mierry, S. Fernandez, F. B. Naranjo, E. Calleja, T. M. Cormack, *phys. stat. sol. (a)*, 192, 97 (2002)

8. F. B. Naranjo, S. Fernandez, F. Calle, M. A. Sanchez-Garcia, and E. Calleja, *phys. stat. sol. (a)*, 192, 341 (2002)

9. P. Mackowwiak, T. Czyszanowski, R. P. Sarzala, M. Wasiak, and W. Nakwaski, *Opto-Electron. Rev.,* 11, 119 (2003)

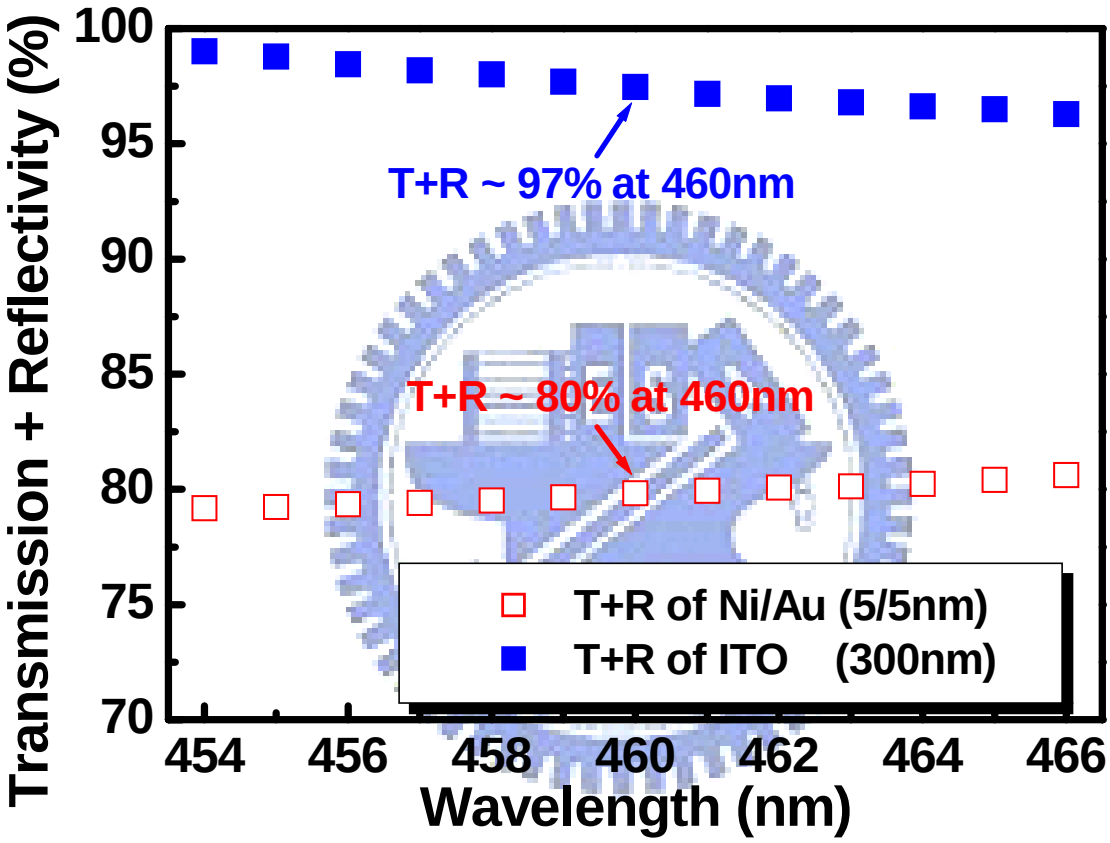

Figure 5.1 Transmission (T) and reflectivity (R) versus wavelength of Ni/Au (5/5nm) and ITO (300nm) films deposited on glass substrate.

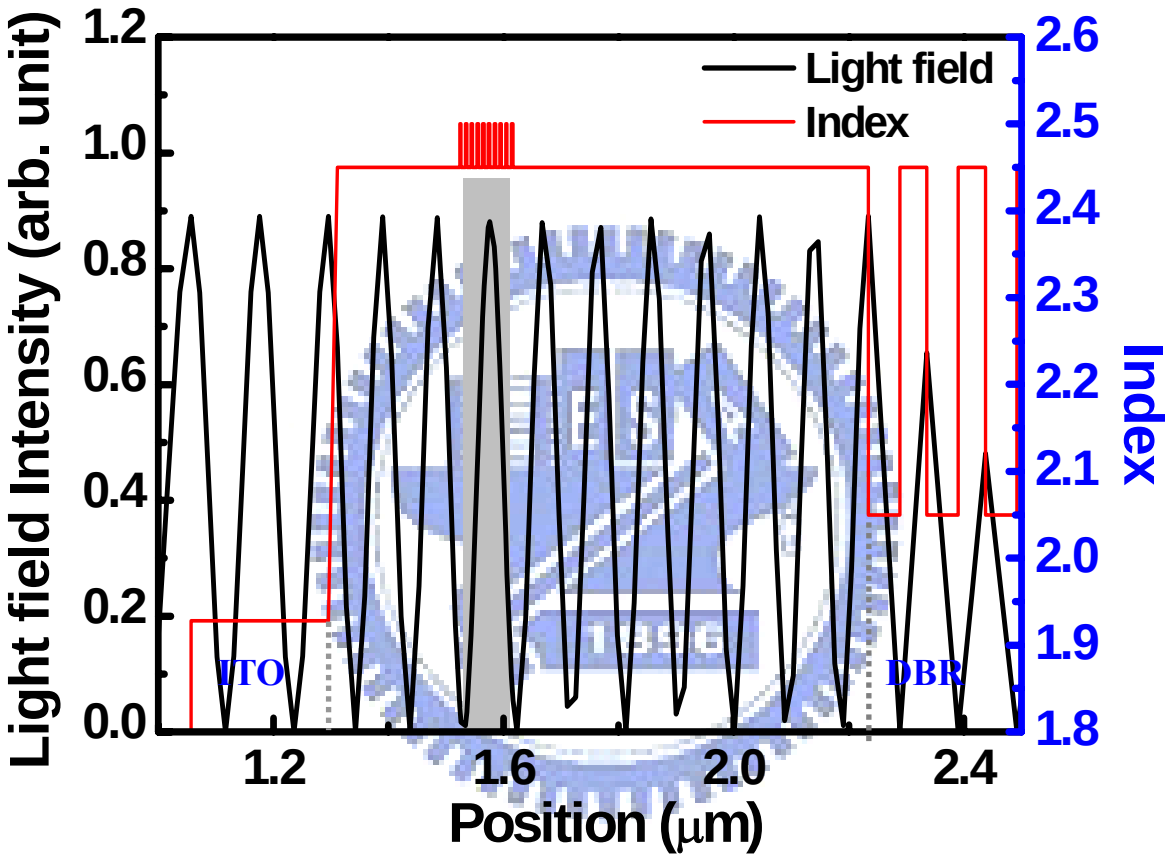

Figure 5.2 Electric field intensity and refractive index as a function of the distance from top layer.

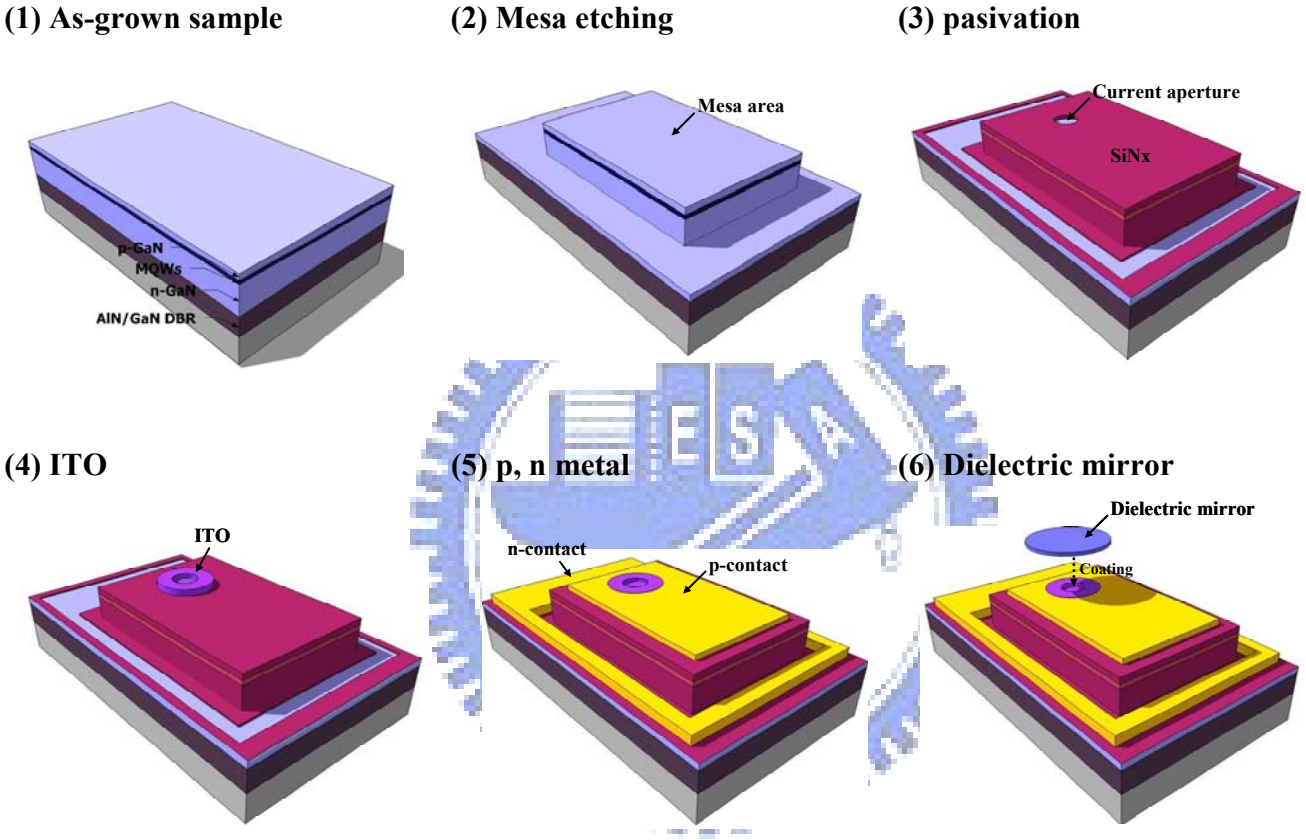

Figure 5.3 The process flowchart of nitride-based micro-cavity devices.

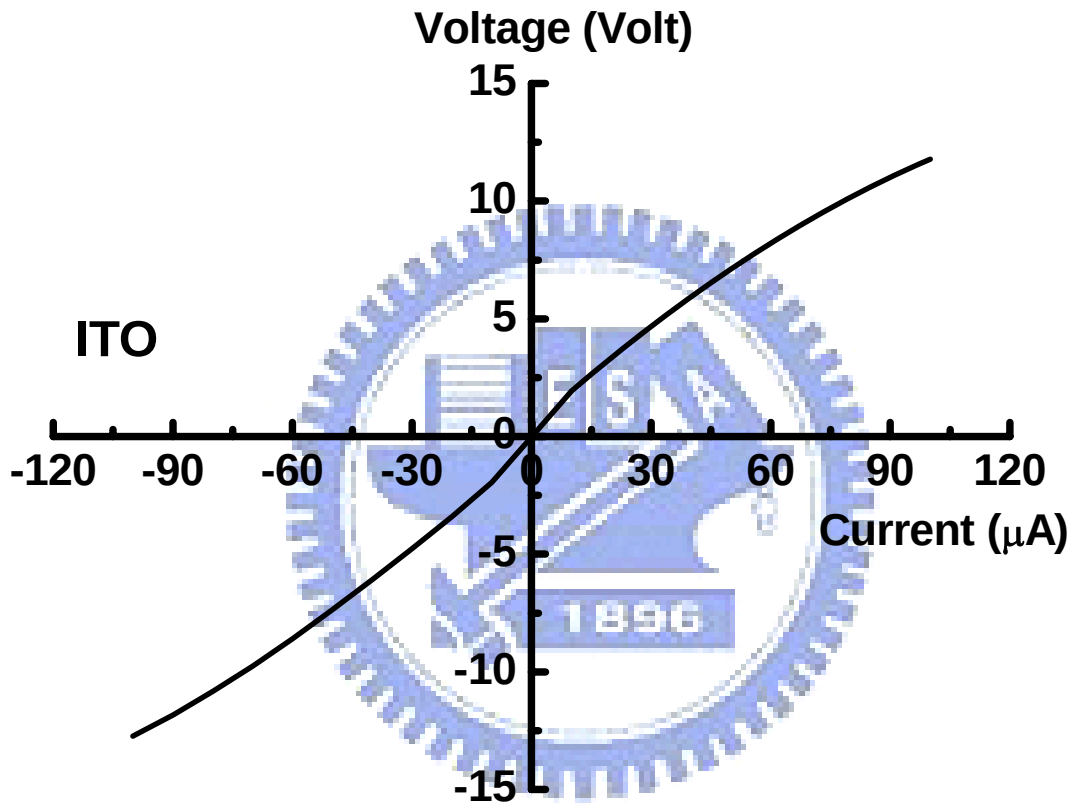

Figure 5.4 The current-voltage characteristic of ITO contact.

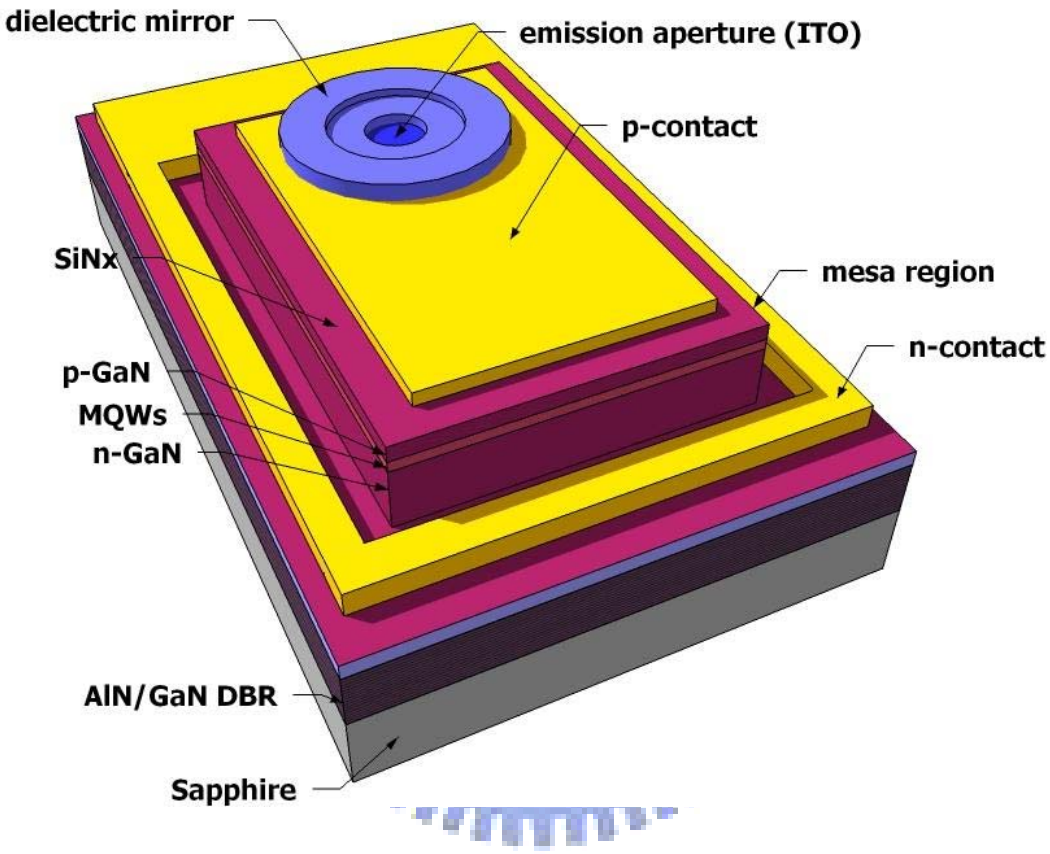

Figure 5.5 The schematic diagram of a fabricated micro-cavity light emitting diode.

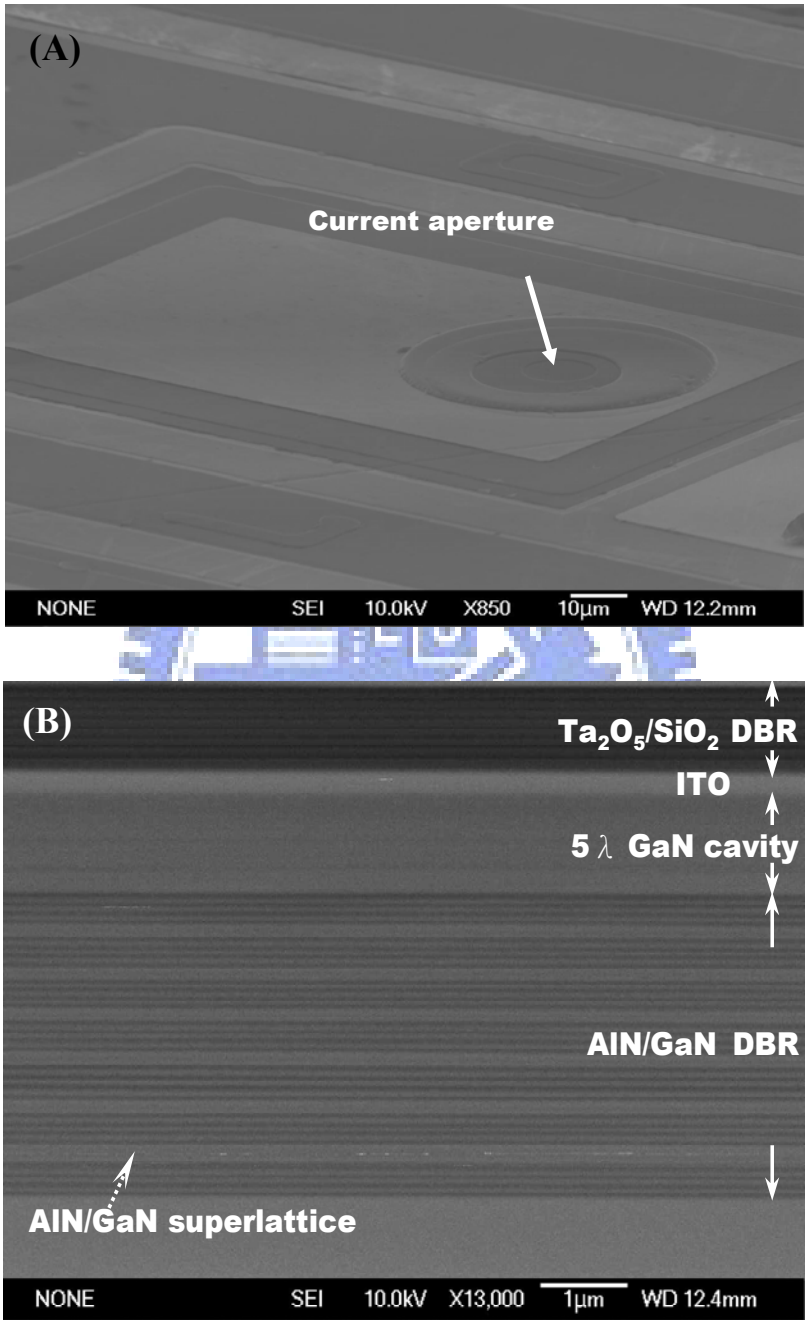

Figure 5.6 SEM images of the fabricated device. (A) Top view. (B) Cross-sectional view.

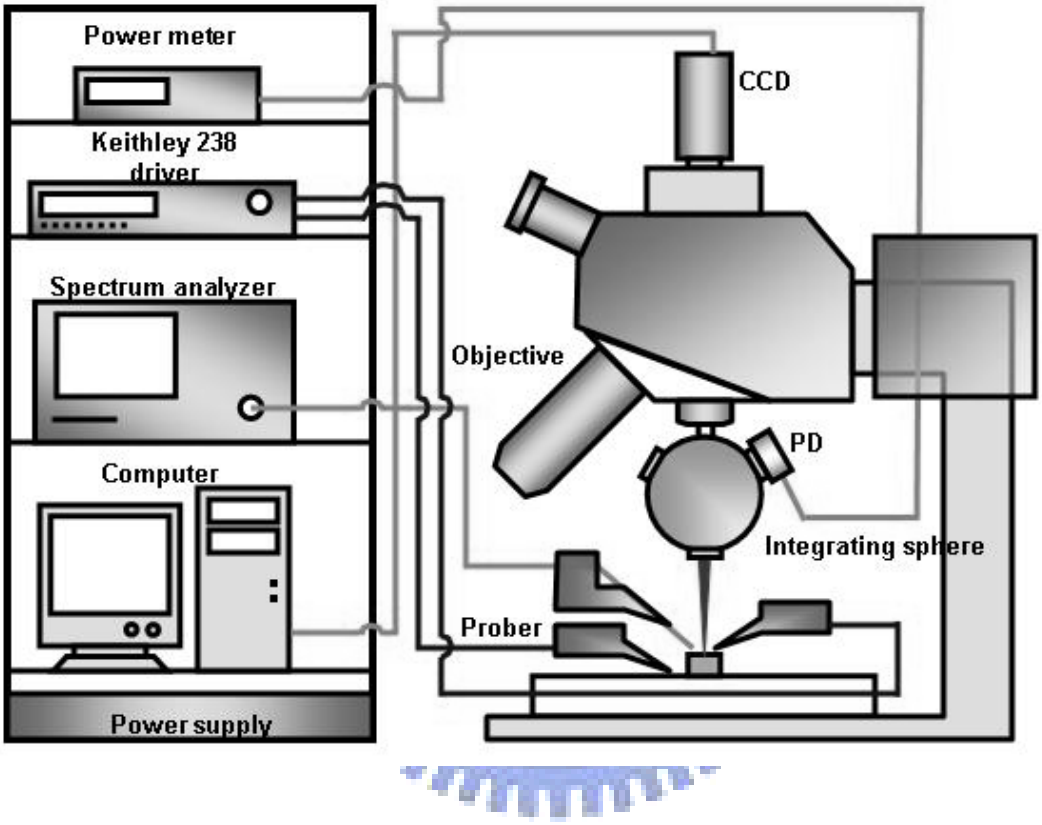

Figure 5.7 The Probe station measurement setup.

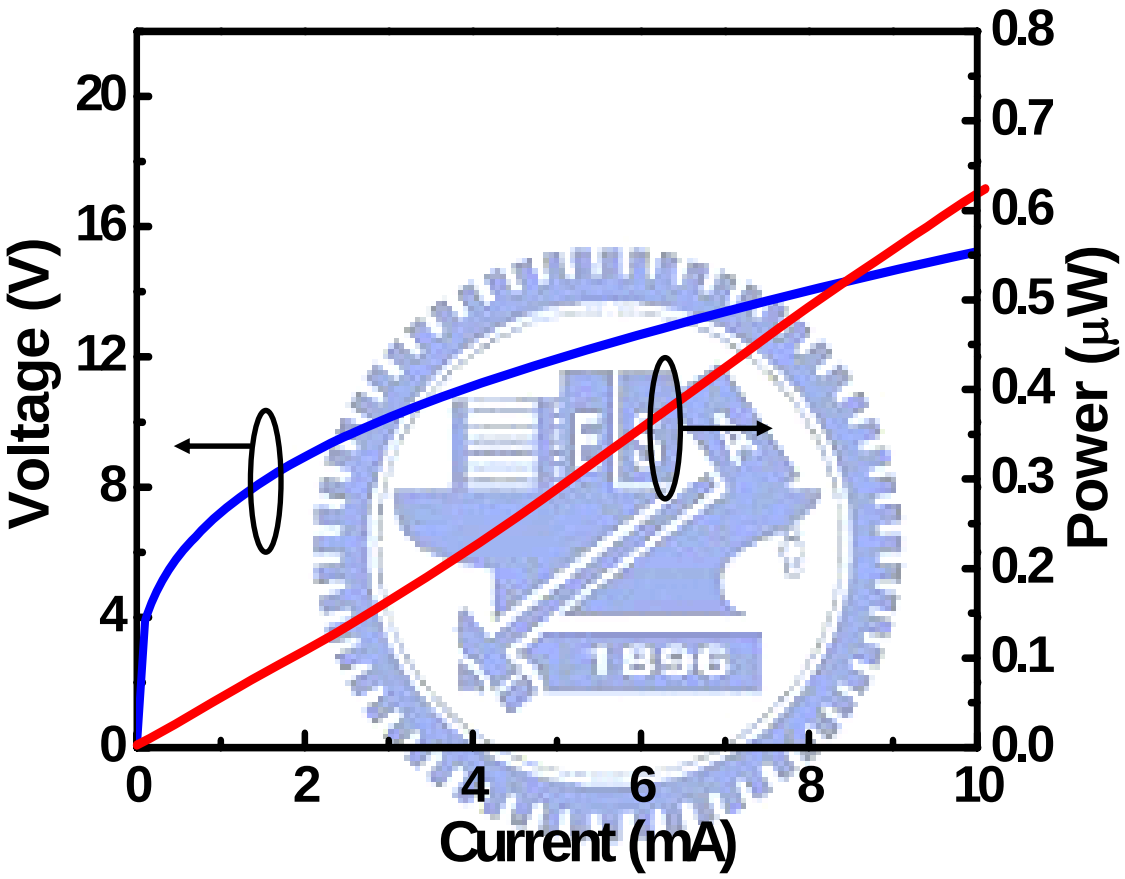

Figure 5.8 Current versus voltage and light output power curves of a fabricated device at room temperature.

(A)

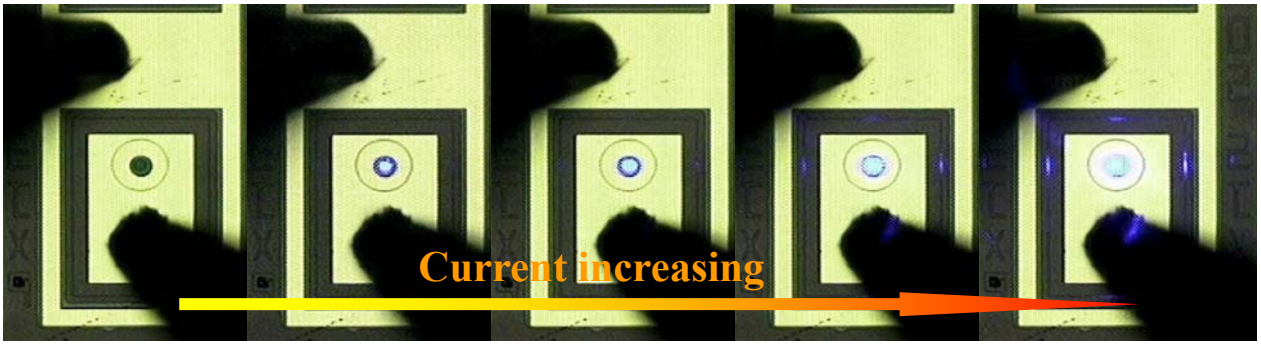

(B)

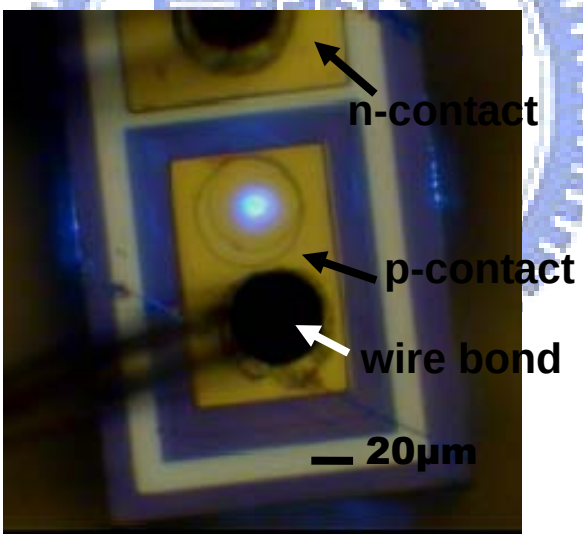

Figure 5.9 (A) Emission images under different injection current. (B) A MCLED chip monted on a metal can.

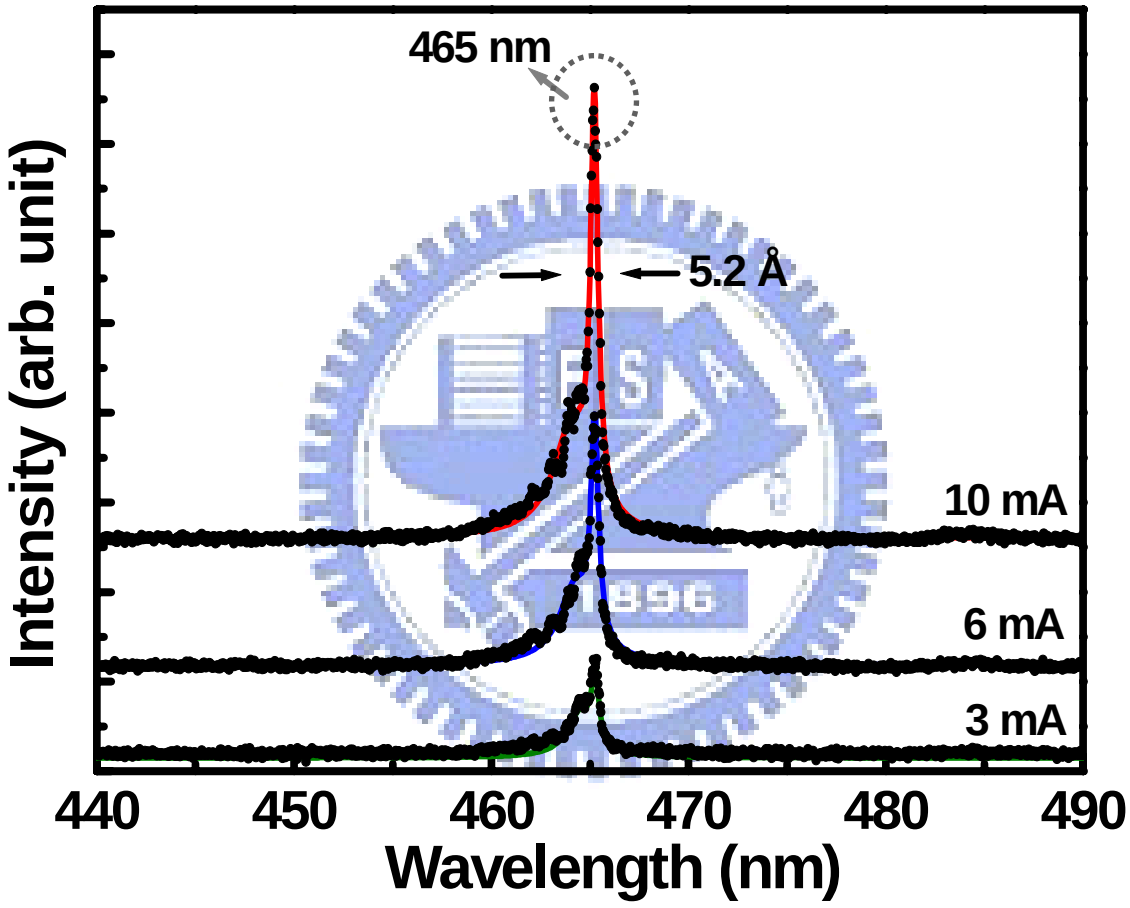

Figure 5.10 Emission spectra of the MCLED under different current of 3 mA, 6 mA, and 10 mA.

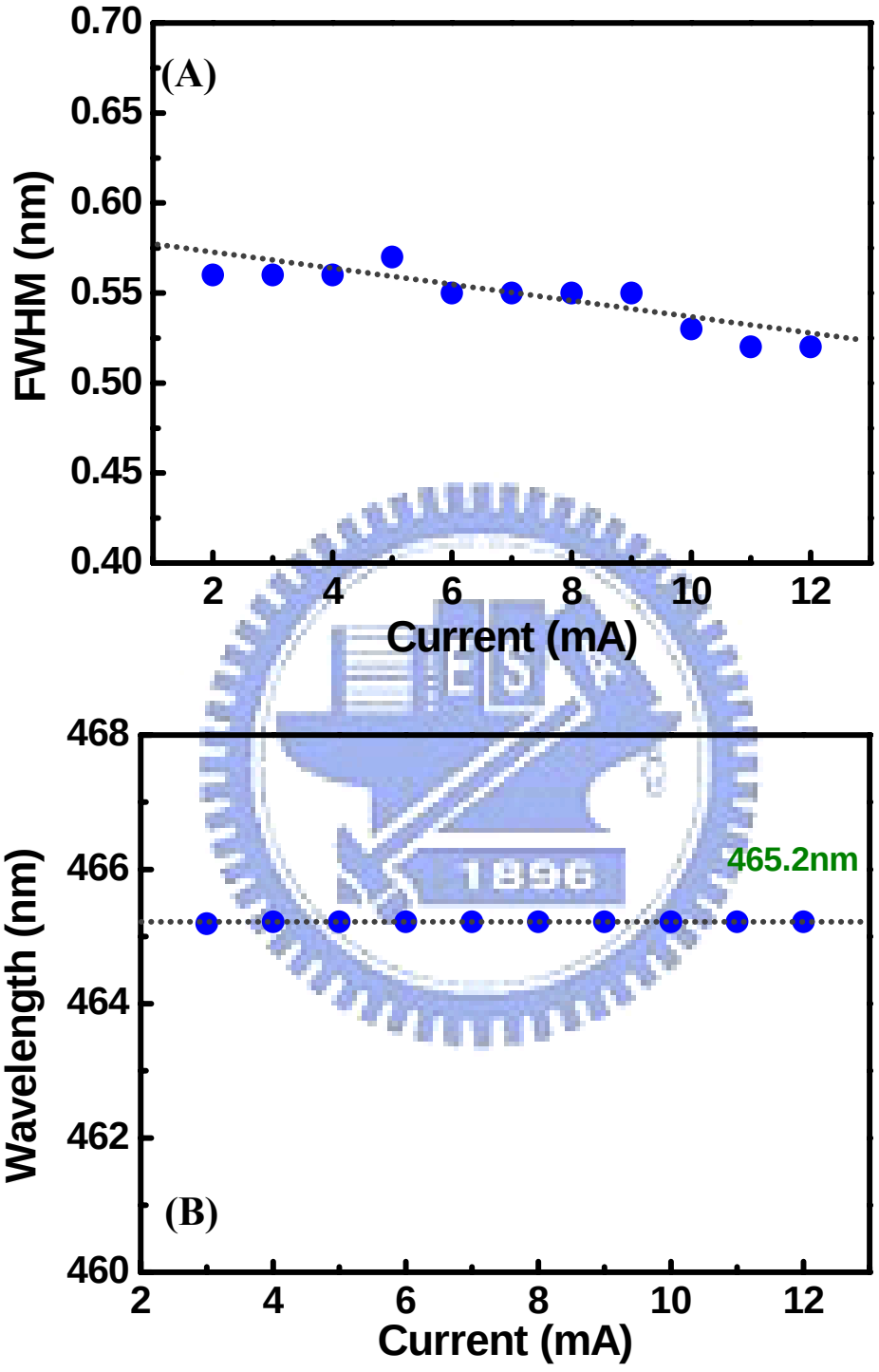

Figure 5.11 The Variation of emission (A) linewidth and (B) wavelength of the MCLED with increasing current.

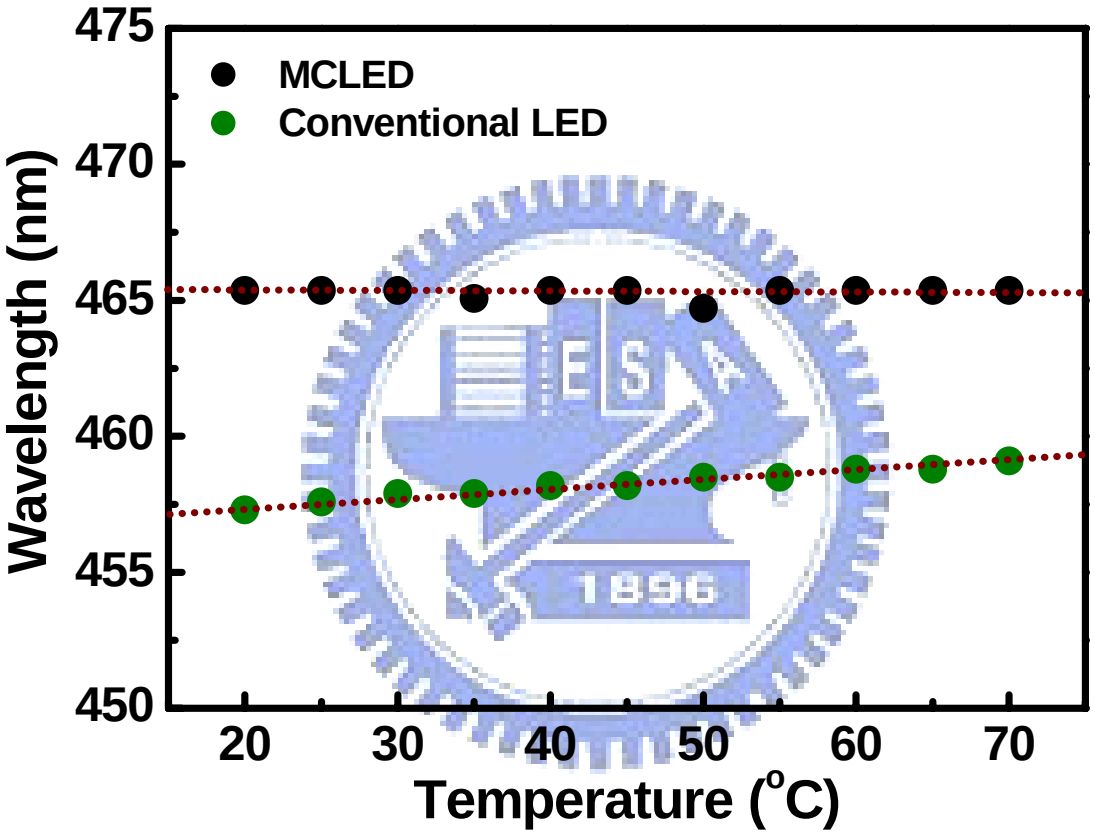

Figure 5.12 Emission peak wavelengths of the MCLED and conventional LED as a function of temperature.

(A)

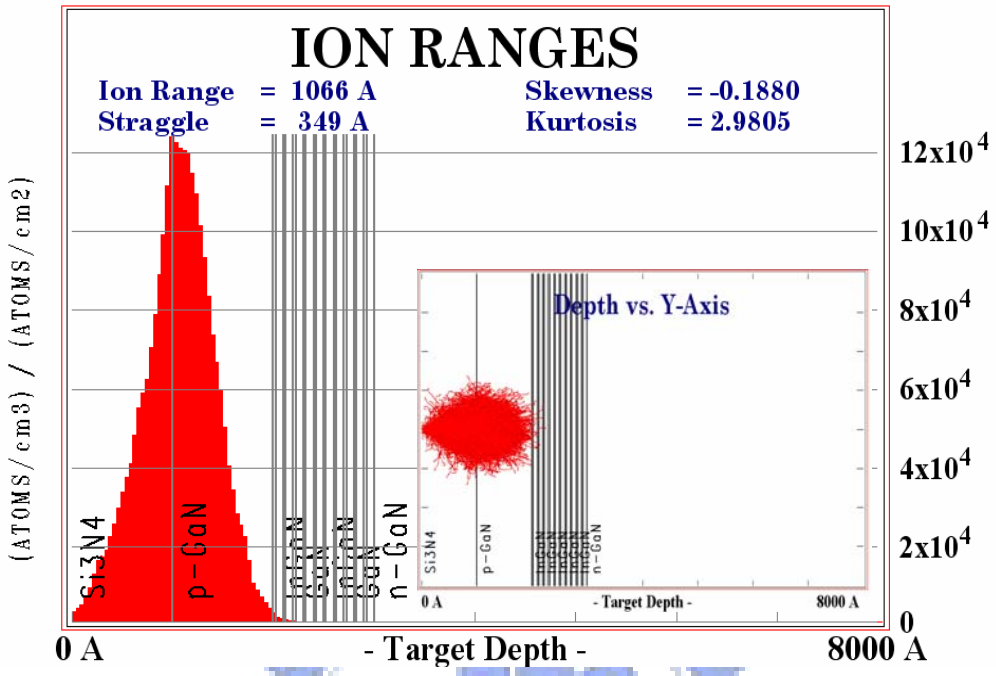

(B)

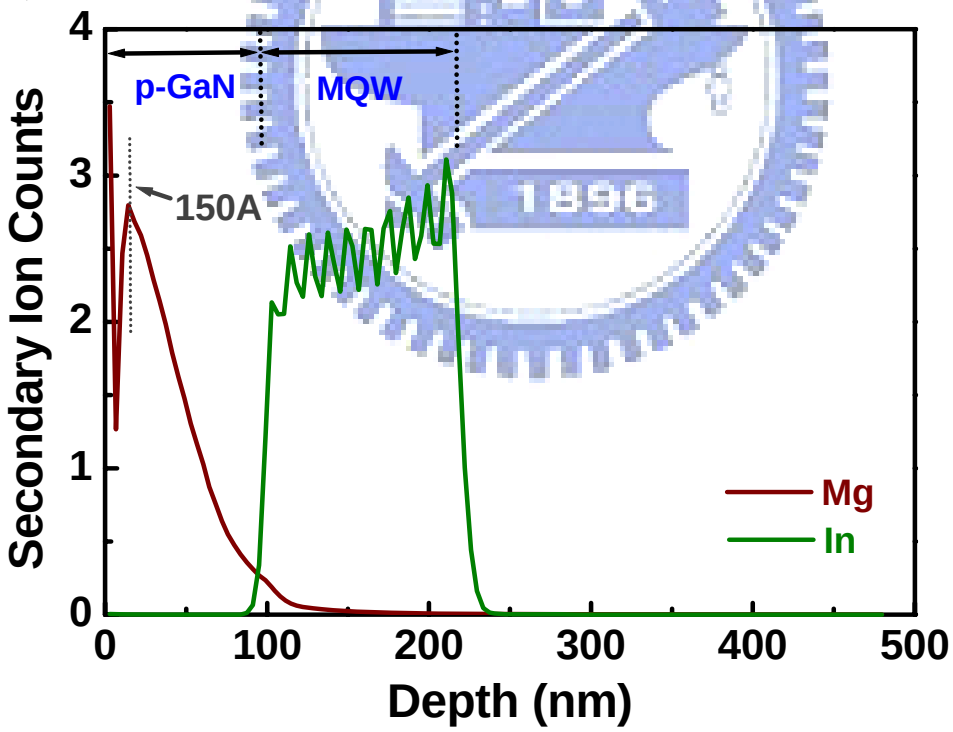

Figure 5.13 (A) The simulation and (B) SIMS data of Mg^+ ion distribution inside the implanted sample with 100nm-thick SiNx buffer layer.

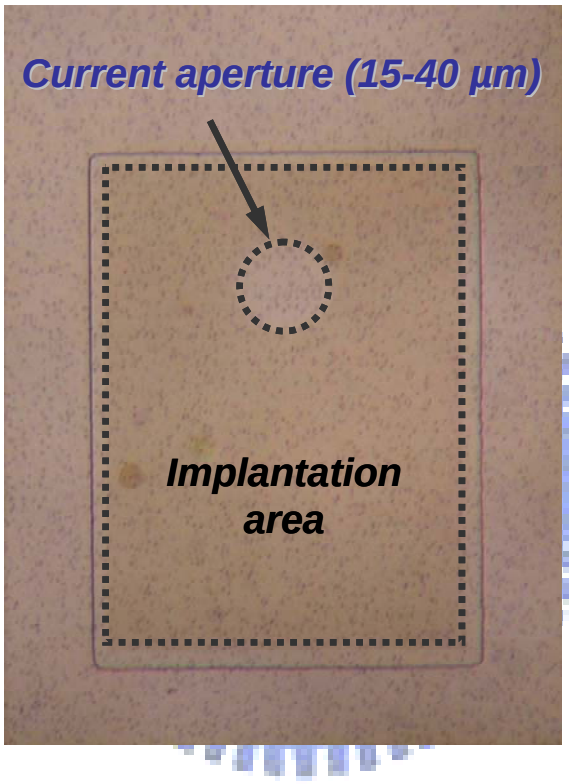

Figure 5.14 OM image of the implanted sample.

(A)

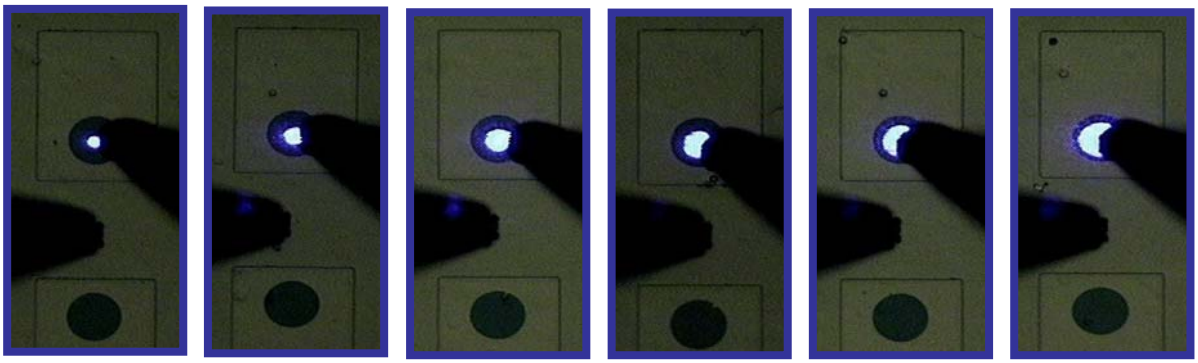

(B) (C)

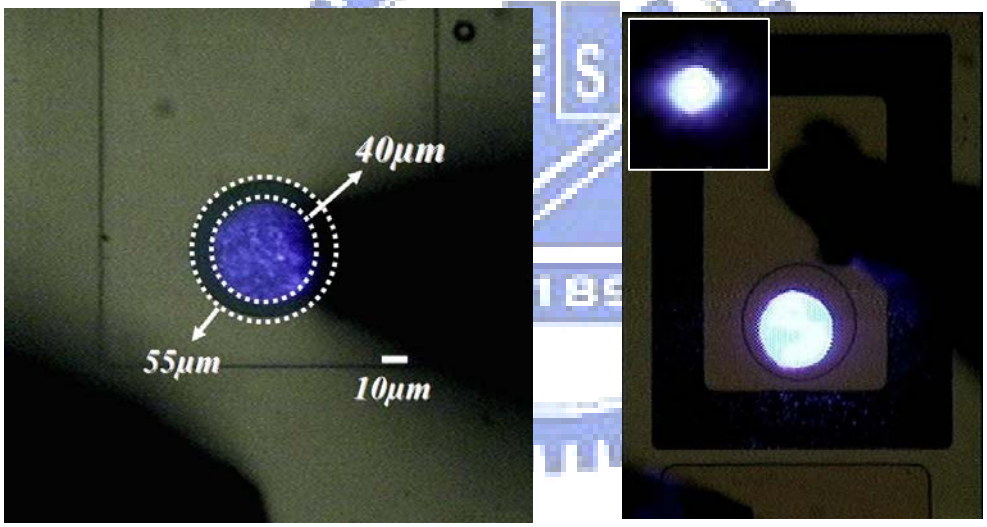

Figure 5.15 (A) Emission images of Mg^+ implanted MCLEDs after deposition of ITO transparent contact layer. (B) An emission image of MCLED with aperture size of 40 μm in high magnification. (C) An emission image of fabricated implanted MCLED.

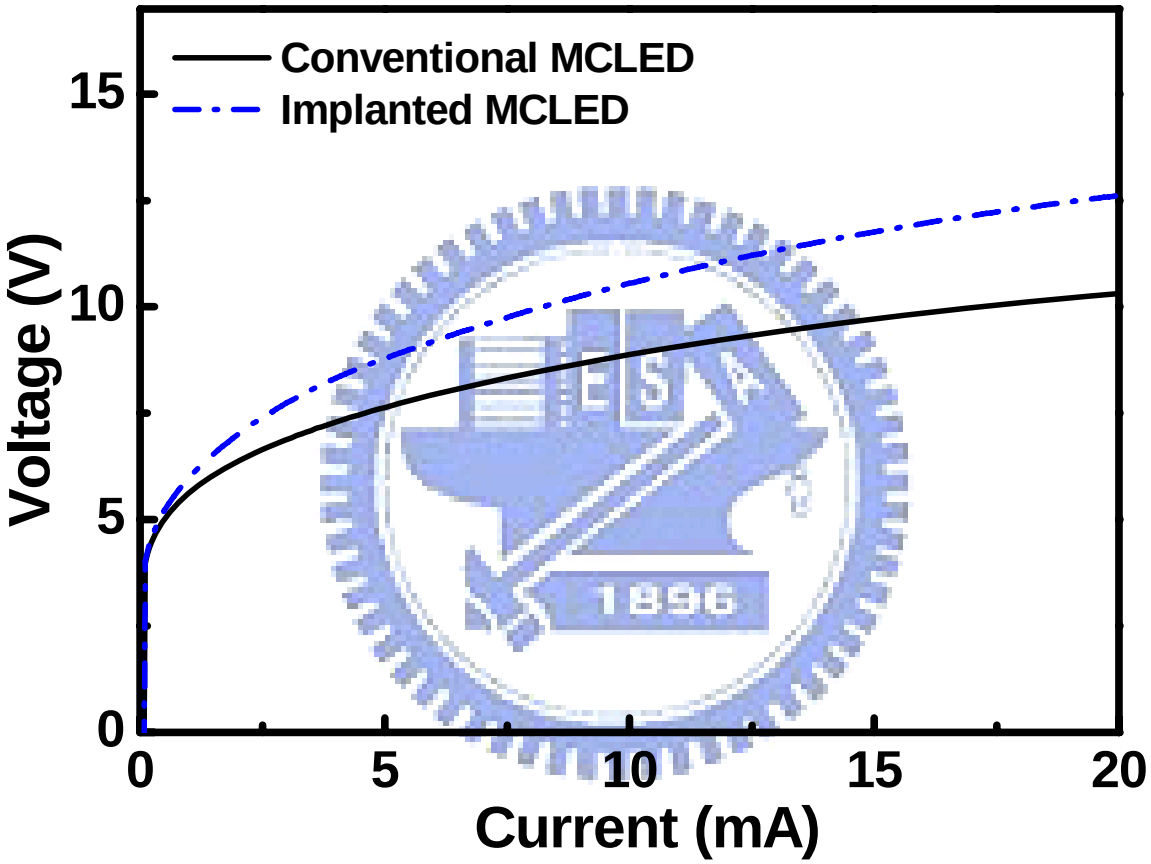

Figure 5.16 Current-voltage curves of the conventional and the Mg^{+} implanted MCLED.

Chapter 6

Fabrication and Characteristics of nitride-based two-dimensional photonic crystal surface emitting lasers

In this chapter, we investigate the fabrication and characteristics of a nitride-based two-dimensional (2-D) photonic crystal surface-emitting laser (PCSEL). The PCSEL is a novel type of semiconductor laser diode. The laser is characterized by large-area lasing, single-mode operation, and low divergence angle. This kind of laser diode has a highly potential to be the next-generation laser diode.

6-1 Fabrication Technique – Electron-Beam Lithography

Currently, photonic crystals, which are periodic patterns with sizes of sub-micrometer, are usually fabricated using electron-beam lithography. The electron-beam lithography (EBL) is a technique using electron beam to generate patterns on a surface with a resolution limited by De Broglie relationship ($\lambda < 0.1$ nm for 10-50 KeV electrons), which is far smaller than the light diffraction limitation. Therefore, it can beat the diffraction limit of light to create a pattern which only has a few nanometers line-width without any mask. The first EBL machine, based on SEM system, was developed in the 1960s. The EBL system usually consists of an electron gun for generating electron beam, a beam blanker for controlling the electron beam, electron lenses for focusing the electron beam, a stage and a computer control system as shown in figure 6.1.

In the process of EBL, the specific Polymethylmethacrylate (PMMA) is required and used to form patterns via exposure of electron beam. In the experiment, we used a special positive PMMA, A3, to form patterns. These parameters for EBL here are described as below.

1. Spin coating PMMA (A3):

a. first step : 1000 rpm for 10sec.

b. second step : 5000 rpm for 90sec.

2. **Hard bake :** hot plate 120^{o}C, 1hr.

3. **Exposure :**

   Beam voltage : 10KeV

   Writefield size : 50μm

   Dot dose : 0.08pAs

4. **Development :** dipping in IPA : MIBK(3 : 1) 50sec.

5. **Fixing :** rising in IPA 30sec.

6. **Hard bake :** hot plate 120^{o}C, 4min.

6-2 Design of Nitride-Based 2-D Photonic Crystal Surface-Emitting Lasers

In this section, we discuss the design of a GaN-based 2-D PCSEL. For a design of a PC laser, to realize the band diagram of the PC is very important because the normalized frequency, which is a ratio of the wavelengths of optical modes and the lattice constants of PC, could be obtained from the band diagram. We could know which lattice constant was required if the lasing wavelength we desired was determined. Of course, this lasing wavelength must be located within the emission of the active layer. According to the theory described in chapter 2, the surface emitting laser in the photonic crystal grating structure could only happen as the Bragg condition is satisfied.In additional, the Bragg condition is satisfied at Brillouin-zone boundary, Γ, K and M point. At these points, light waves can have opportunity to diffract normally to the surface which was described in section 2.5. Therefore, we can design a GaN-based 2-D PCSEL operating at the designed lasing wavelength with the optimized lattice constant at Brillouin-zone boundary, Γ、K and M point, which can be defined in the photonic band diagram.

In this study, we fix the parameter, r/a, to be 0.28 for calculating the band diagram of PC

using 2-D plan-wave expansion (PWE) method. In fact, the 2-D PWE method couldn't precisely evaluate the photonic band diagram of our 3-D structure. This means we should do some modification to parameters describing our structure and then bring them into the method of 2-D PWE to approximate real condition. Therefore, according to reference [1], we further consider two parameters such as confinement factor (Γ_g) and effective refractive index (n_{eff}). Γ_g is the ratio of the light confined within the 2-D PC structure to the light inside the entire device, and n_{eff} is the effective refractive index of the entire device with PC. Γ_g and n_{eff} could be used to estimate the effective dielectric constant of nano-hole (ε_a) and the background (ε_b) for 2-D PWE calculation to further approximate the 3-D structure. These two parameters can be obtained by solving the distribution of the electric field in the in-plane direction. The Γ_g and n_{eff} for describing our structure are estimated to be 0.613 and 2.2 considering fundamental mode, respectively. Then, we could determine ε_a and ε_b using two conditions:

$$n_{eff}^2 = f\varepsilon_a + (1-f)\varepsilon_b \tag{6.1}$$

$$\Delta\varepsilon = \varepsilon_b - \varepsilon_a = \Gamma_g(\varepsilon_{mat} - \varepsilon_{air}) \tag{6.2}$$

where the f is a filling factor, ε_{mat} is the dielectric constant of semiconductor, and ε_{air} is the dielectric constant of air. For a triangular-lattice PC, f is written as:

$$f = \frac{2\pi r^2}{\sqrt{3}a^2} \tag{6.3}$$

Therefore, the value of ε_a and ε_b for our PC device could be obtained to be 2.408 and 5.63, respectively.

To bring ε_a and ε_b into the calculation, a band diagram of the 2-D triangular-lattice PC structure with r/a=0.28 on our sample structure could be estimated as shown in figure 6.2. The figure shows lots of modes densely existed between the normalized frequencies of 0.45 and 0.7. According to the theory described in chapter 2, the surface emitting laser in the photonic crystal grating structure could only happen as the Bragg condition is satisfied. In order to have a high opportunity to meet those modes satisfying Bragg condition, the lattice constant of

photonic crystal were determined to range between 190nm to 300nm (the normalized frequency ranges between 0.45 and 0.7) considering a lasing wavelength of ~425 nm. (The photoluminescence of the sample used in this experiment was centered at around 425 nm.)

6-3 Fabrication of Nitride-Based 2-D Photonic Crystal Surface-Emitting Lasers

Figure 6.3 shows the schematic diagram of a triangular-lattice photonic crystal surface emitting laser. The nitride sample used in this experiment was similar to the as-grown sample shown in figure 3.8 (in chapter 3). The center wavelength of bottom DBR was about 430 nm. The DBR here could be a reflector to reflect downward light back to the photonic crystal region. The spontaneous emission of the sample was excited by a focused He-Cd laser (325 nm). Figure 6.4 shows the micro-photoluminescence (μ-PL) emission spectrum of the as-grown structure. The peak wavelength is centered at 425 nm with a FWHM of about 20 nm. The PC laser was fabricated by a few process steps. In the beginning, the SiN 200 nm was deposited as a hard mask using PECVD. The PMMA layer (150 nm) was spun by spinner and patterned using an e-beam lithography system (Raith, ELPHY QUANTUM) to form a soft mask. The lattice constants of PCs were patterned to be the range between 190 nm and 300 nm. The diameter of each PC device was 50 μm. The PC pattern on soft mask was transferred to SiN film by using ICP-RIE (Oxford Plasmalab system 100), and the PMMA layer was removed by dipping ACE tone. Then, the sample was performed a dry etching in an ICP-RIE system (SAMCO RIE-101PH) to etch GaN as deep as 400 nm. Finally, the sample was dipped in BOE to remove the hard mask to complete PC lasers. Figure 6.5(A) and (B) shows the SEM photos of fabricated photonic crystal in top view and cross-section view, respectively.

6-4 Characteristics of Nitride-Based 2-D Photonic Crystal Surface-Emitting Lasers

Threshold characteristics

The threshold characteristics of the nitride-based 2-D PCSEL were measured using the optical pumping with a pumping spot size of around 50 μm. The lasing action could be observed in several different devices (different lattice constant a=190-300 nm) with different lasing wavelength. We plot normalized frequencies of those lasers versus lattice constants as shown in figure 6.6. The figure shows the PC device with larger lattice constant has the larger normalized frequency. Taking one of them (a=290 nm) as example, the laser emission intensity from the 2-D PCSEL as a function of the exciting energy density is shown in Fig. 6.7. The threshold energy density (E_{th}) was observed to be around 3.5 mJ/cm^2. The light intensity increased rapidly and linearly as the excitation energy density was above the threshold. Figure 6.8 shows the lasing spectra at different pumping energy, and the inset shows the emission spectrum at the energy density of 0.66 E_{th}. The spontaneous emission of the PC device below the threshold was centered at around 405 nm. A sharp and narrow laser emission was then clearly observed as the pumping energy increased above the threshold energy. The lasing wavelength located at around 424.3 nm, and the FWHM of the laser is around 0.11 nm. It evidently expresses the laser action actually happened at the PC device. Other PC devices also could be excited to lase at the similar threshold energy and emitted different lasing wavelengths. The most interesting is the variation of lasing wavelengths of devices with different lattice constants. Figure 6.9 shows the lasing spectra of PC devices with three different lattice constants, 201 nm, 244 nm, and 290 nm (points I, II, and III marked in figure 6.6). The lasing wavelengths of these three devices were 402.2 nm, 412.4 nm, and 424.3 nm for PC devices with 201 nm, 244 nm, and 290 nm of lattice constant, respectively. The lasing wavelengths show an obvious red shift with the increase of lattice constant. The lasing wavelength differences among them are around 10 nm and 12 nm. We further put the simulated band diagram (figure 6.2) and experiment data (figure 6.6) together for comparison and show it in figure 6.10. The comparison between these two figures helps us to be able to

classify normalized frequencies of our lasers in figure 6.6 into a few groups. Each group of them could correspond to one of simulated band edges at Brillouin-zone boundaries, Γ、M and K. This means the lasing action could only occur at the specific normalized frequency satisfied the Bragg condition. Furthermore, the device with a larger lattice constant of PC would lase at the PC band edge with a larger normalized frequency.

Figure 6.11(A) and (B) show the spontaneous emission image at $0.92E_{th}$ (pumping spot size was about 50μm) and the laser emission image at $1.47E_{th}$, respectively. As the pumping energy was below the threshold, the light emission intensity was uniform across the whole PC region (the diameter is 50μm). With the pumping energy increasing above the threshold, a great portion of the PC region started to brighten substantially. Theoretically, the lasing emission in such device should exist in entire PC region; however, figure 6.11(B) shows the lasing area is not full of the PC region. It could be attributed to the disorder of PC, un-uniformity of pumping laser beam, or inhomogeneiety of InGaN-based gain material. Nevertheless, the nitride-based 2-D PCSEL could actually have an obviously larger lasing area than that of nitride-based VCSEL, which is just several micro-meters.

Polarization

The polarization of the laser was measured by inserting and rotating a polarizer in front of a fiber which collects light into a spectrometer. Figure 6.12 shows the laser emission intensity as a function of the angle of the polarizer. Here we defined the degree of polarization (DOP) as $DOP = (I_{max}-I_{min})/(I_{max}+I_{min})$, where I_{max} is the maximum intensity and I_{min} is the minimum intensity. From the figure, we could estimate the degree of polarization of the laser to be about 53%. In fact, the calculation of electric-field vectors in triangular lattice PCs was reported [2], and results suggested that this kind of the laser has weightless polarization property of the laser emission. This could explain the low DOP of our lasers.

We also varied the detecting angle of a fiber which collects light into a spectrometer to measure the laser emission. The fiber is mounted on a stage which could be rotated from -90°

to 90°. We measured the emission intensity every 10 degree. Here the 90° is the direction parallel to the sample surface. Figure 6.13 shows the laser emission intensity as a function of the detecting angle of the fiber. The result suggests the laser is vertically emitted. This characteristic is a strong enough evidence to reveal the PCSEL is a kind of considerably excellent single-mode surface emitting laser.

References

1. M. Imada, A. Chutinan, S. Node, and M. Mochizuki, *Phy. Rev. B*, **65**, 195306 (2002)

2. S. L. Chuang, Physics of Optoelectronic Devices, *John Wiley & Sons, Inc* (1995)

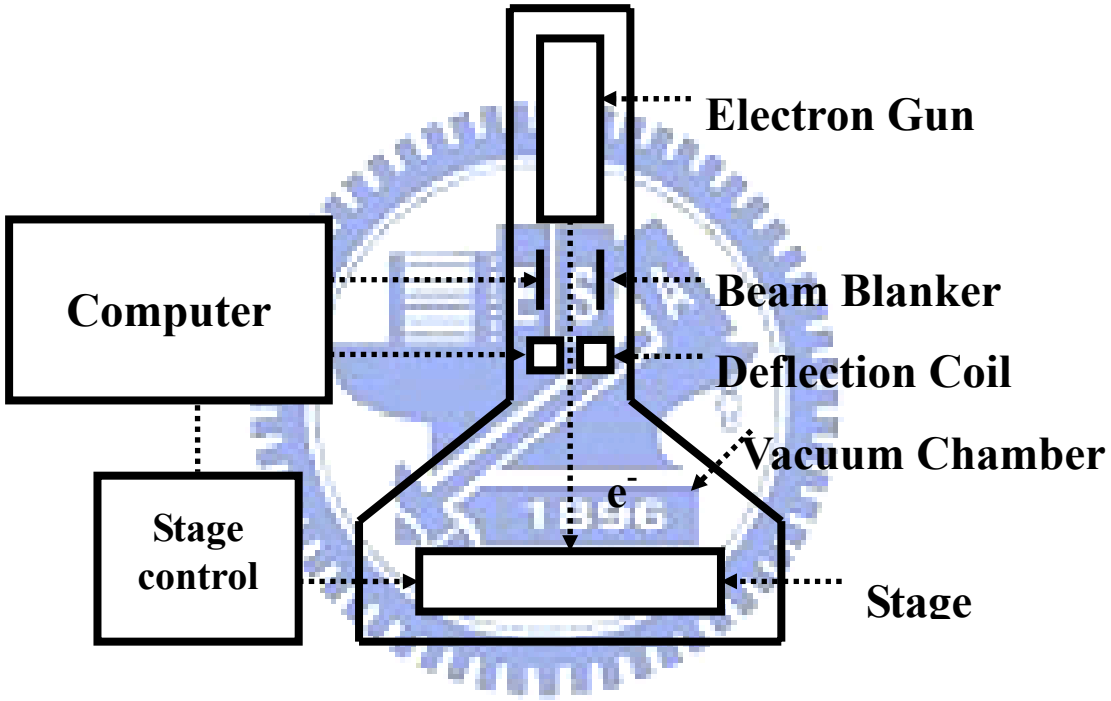

Figure 6.1 A schematic diagram of a typical electron beam lithography system.

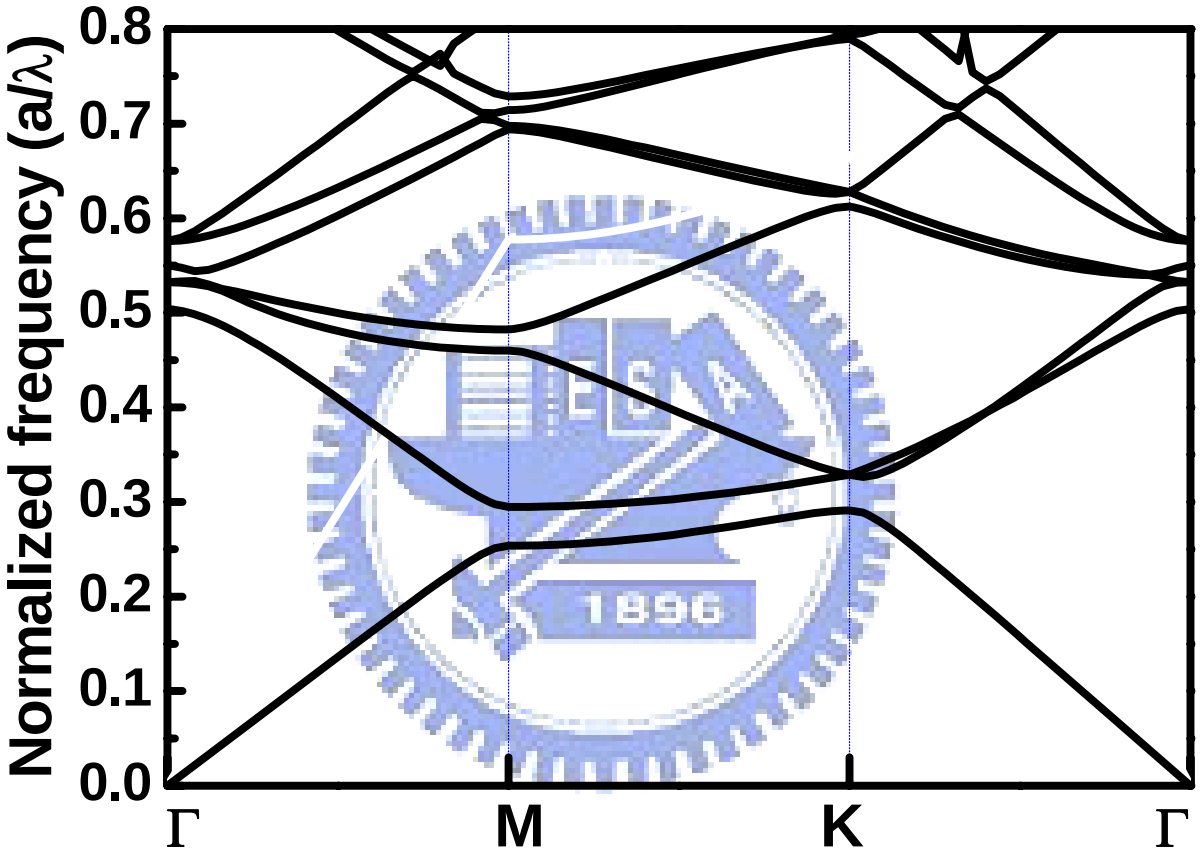

Figure 6.2 The band diagram of the 2-D triangular-lattice PC structure on our sample structure. The value of r/a here is 0.28.

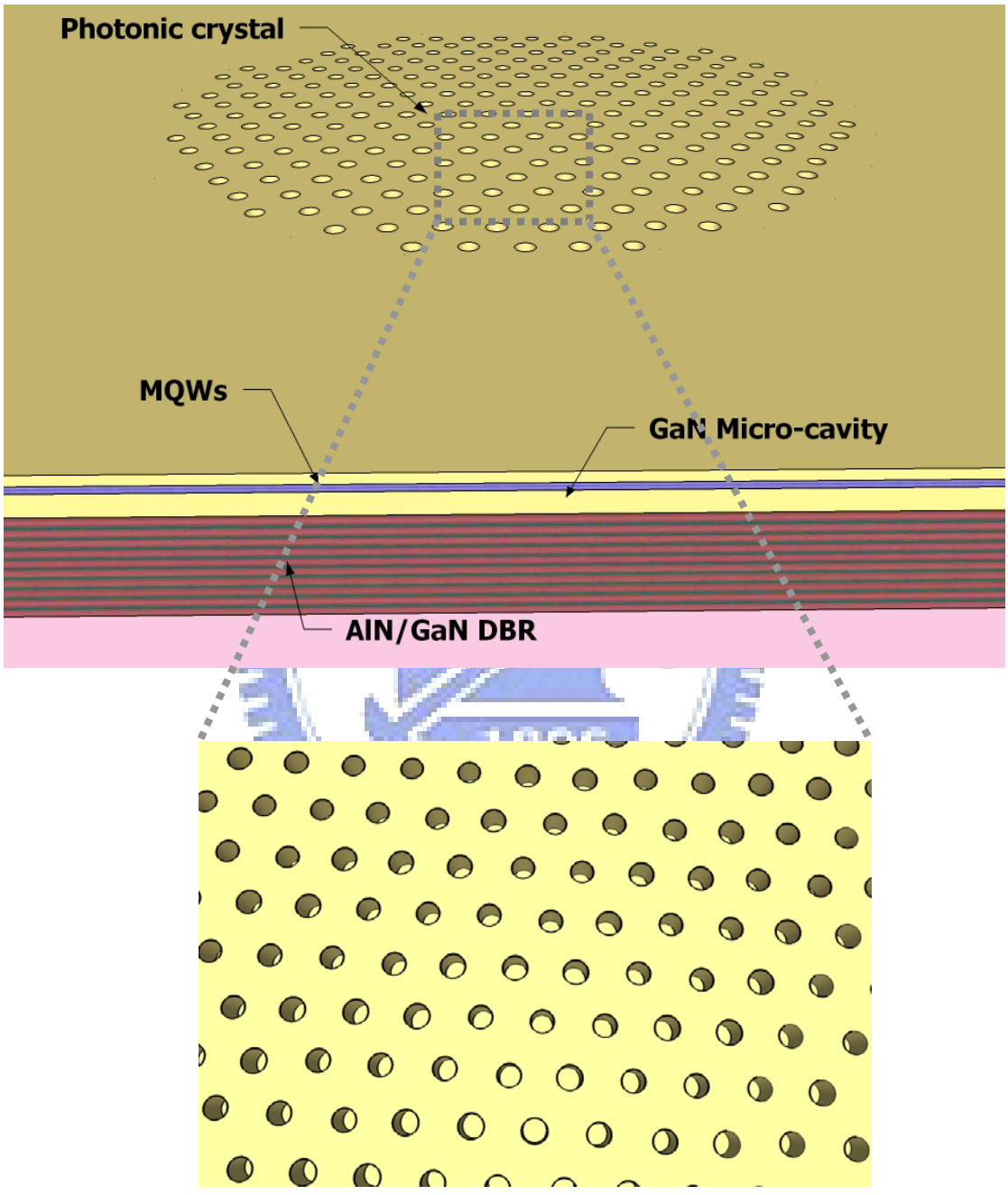

Figure 6.3 The schematic diagram of our photonic crystal surface emitting lasers.

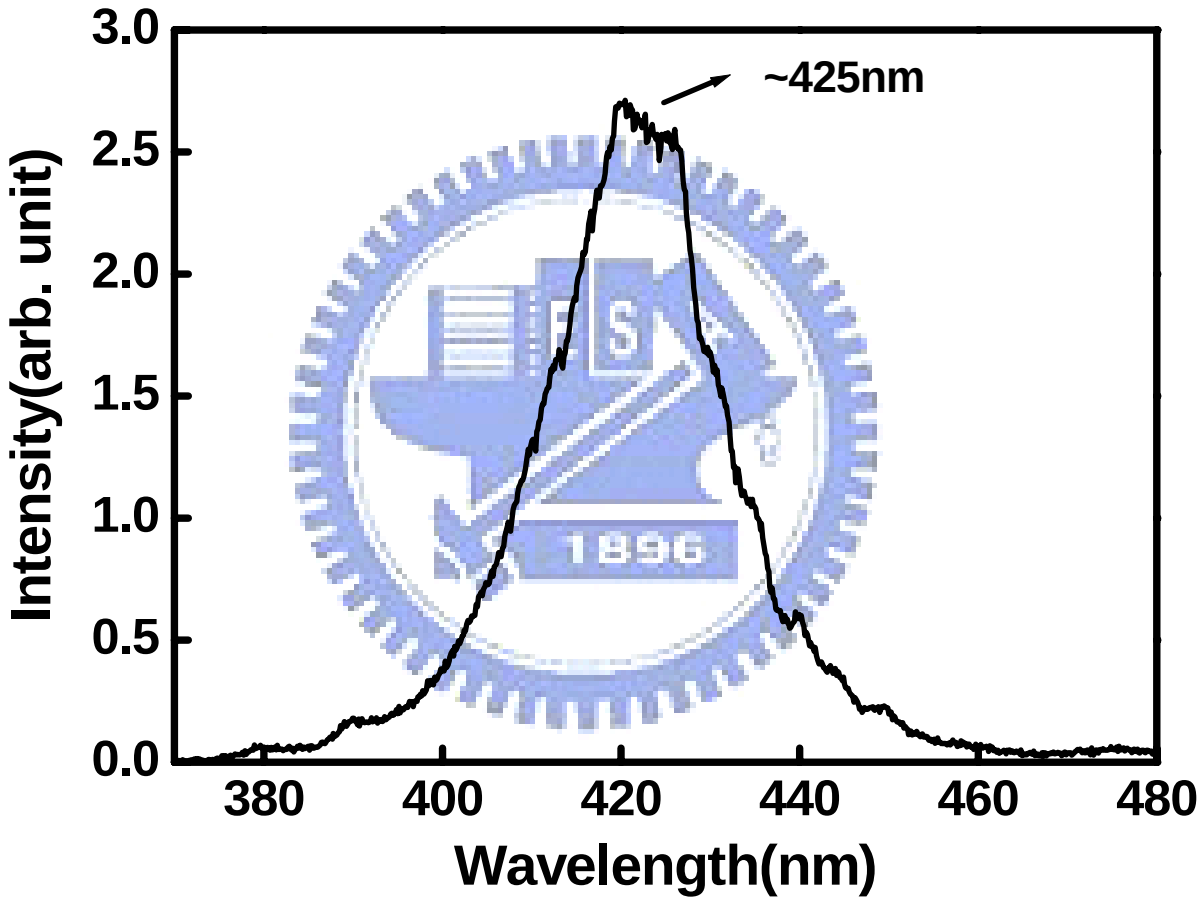

Figure 6.4 The μ-PL of the as-grown sample.

(A)

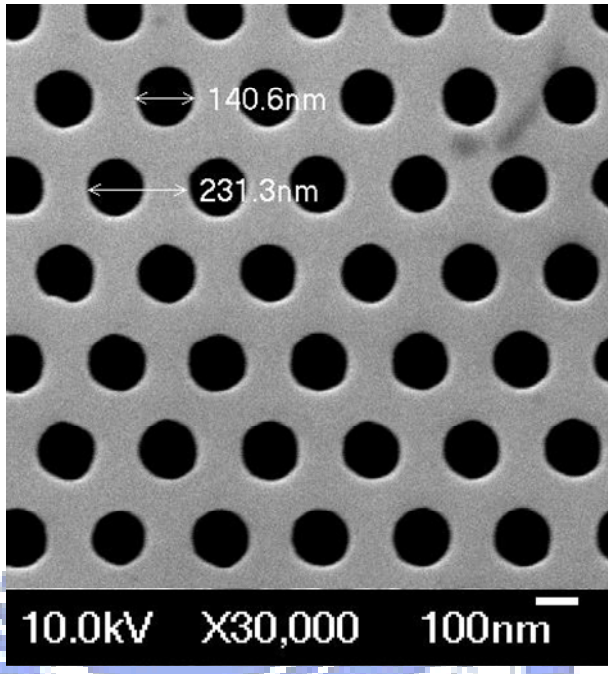

(B)

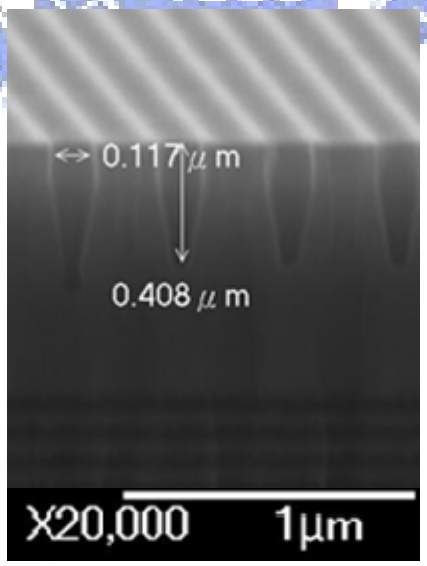

Figure 6.5 SEM images of our photonic crystal surface emitting lasers. (A) Top view. (B) Cross-sectional view.

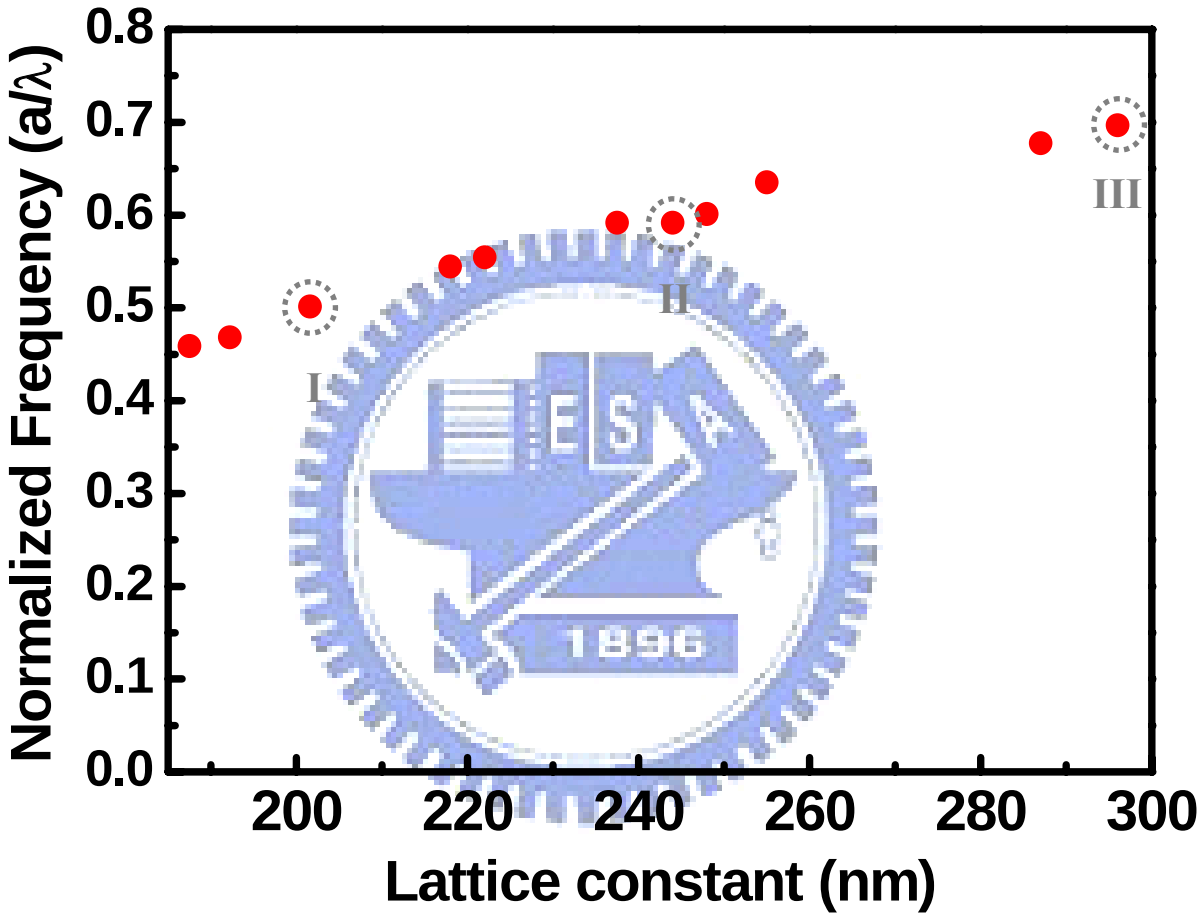

Figure 6.6 Normalized frequencies of our PCSELs as a function of lattice constant.

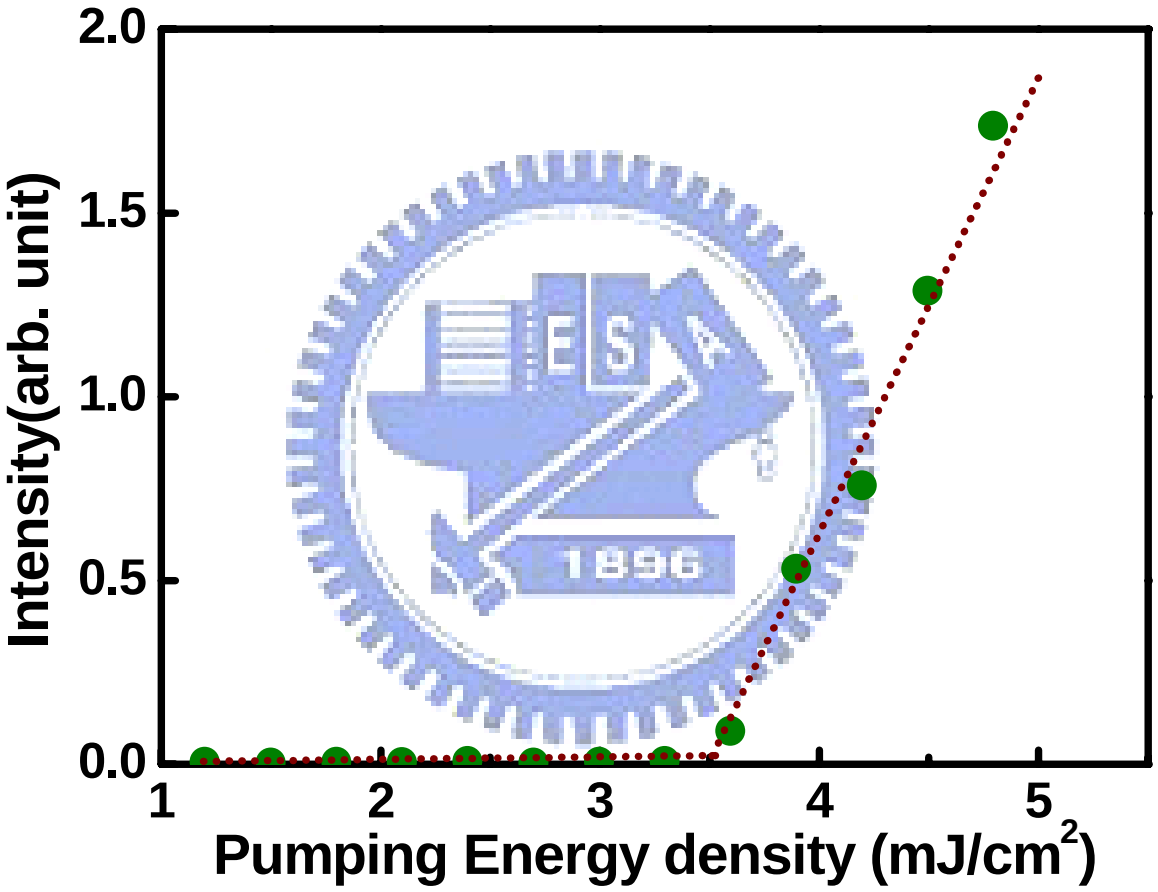

Figure 6.7 The laser emission intensity from a 2-D PCSEL as a function of the pumping energy density.

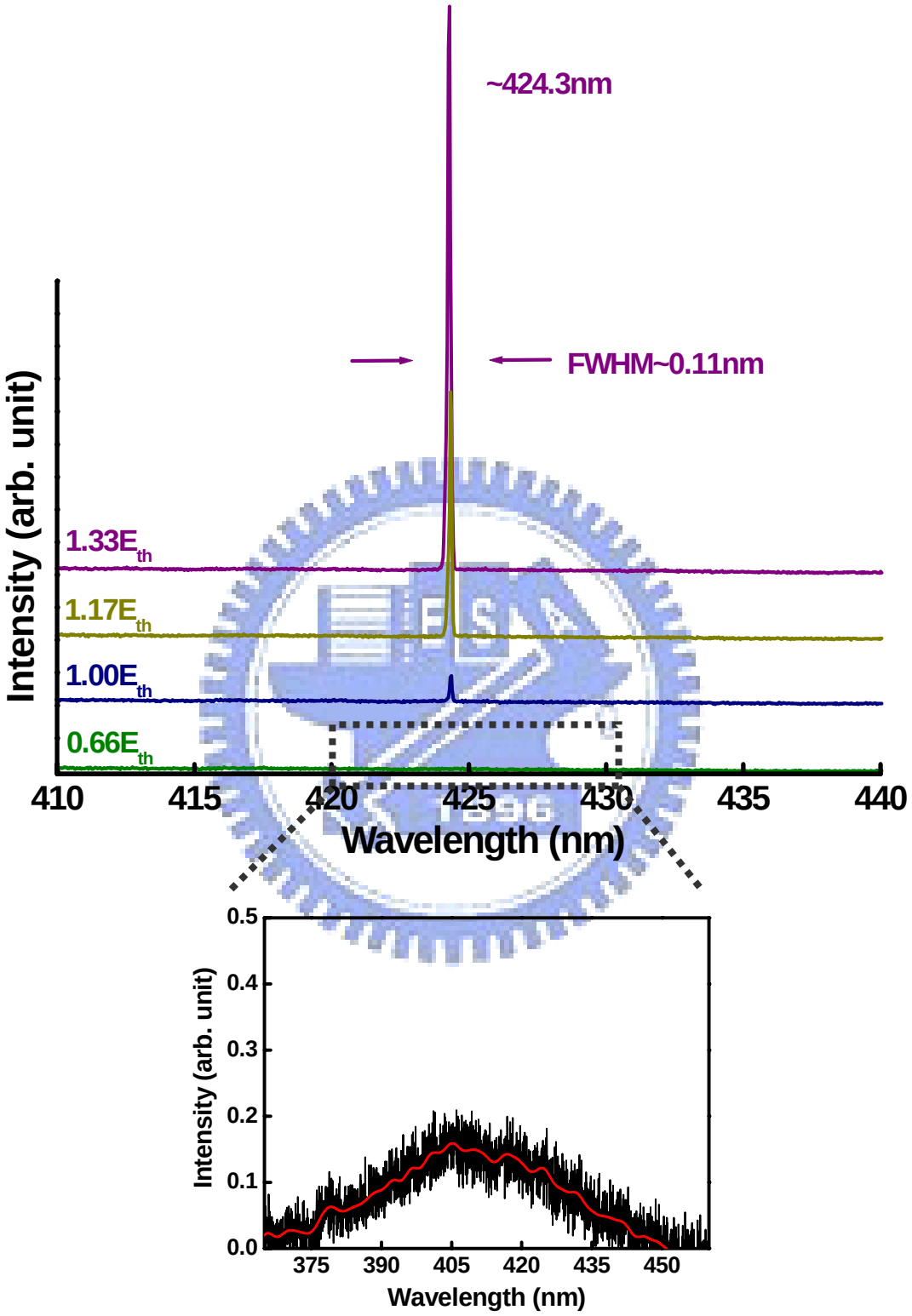

Figure 6.8 Emission spectra of a 2-D PCSEL under four different pumping energy densities.

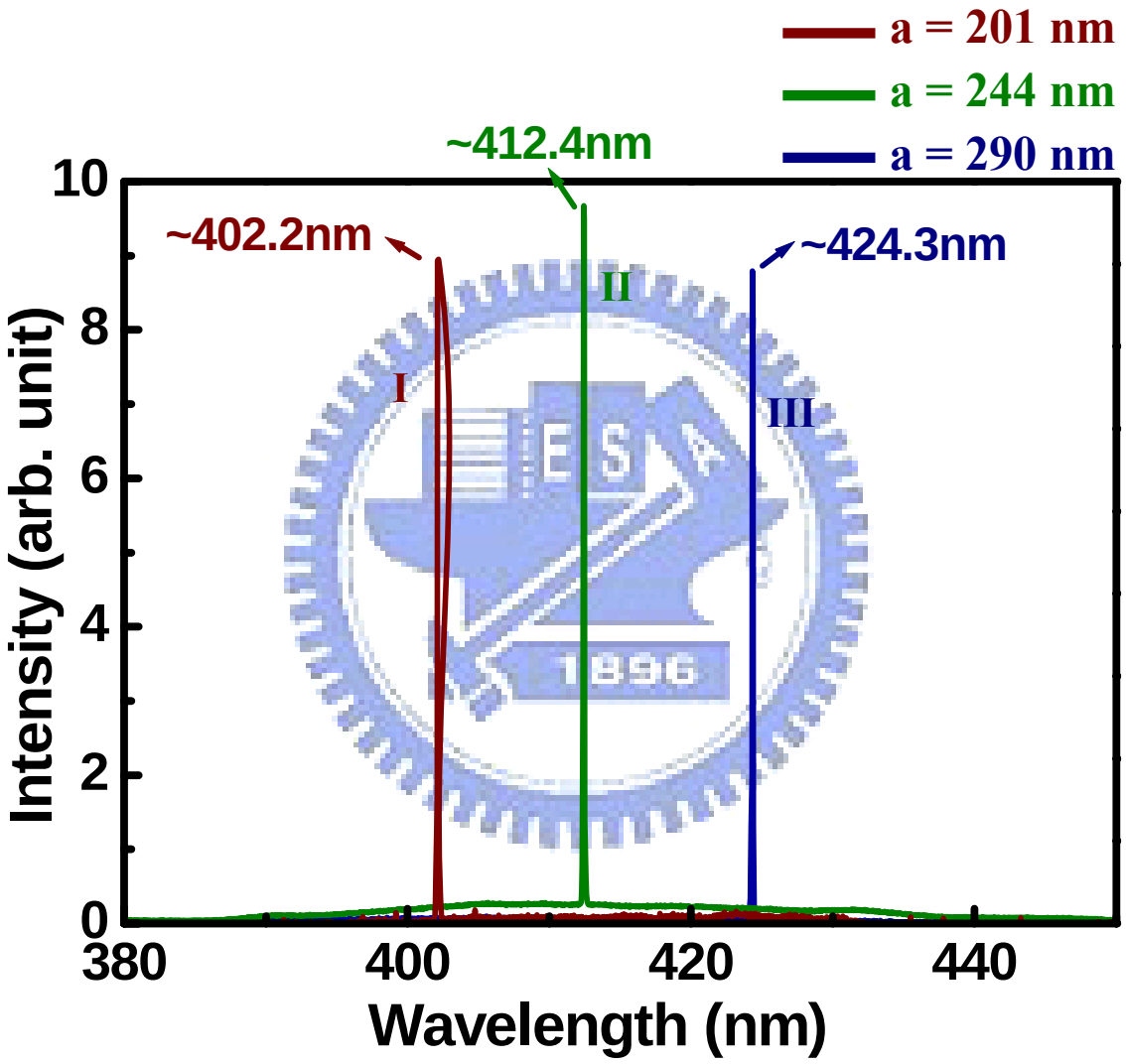

Figure 6.9 Lasing spectra of PC devices I, II, and III with three different lattice constants, 201 nm, 244 nm, and 290 nm, respectively.

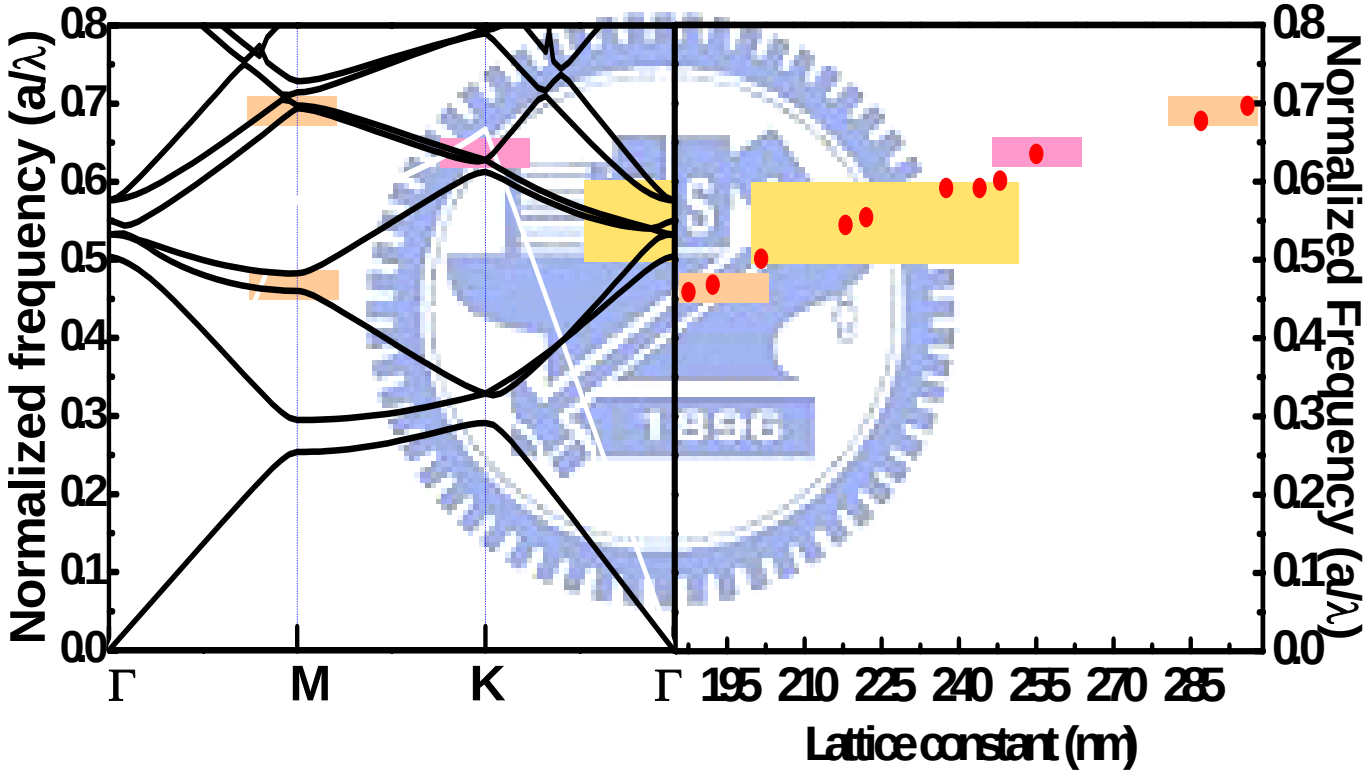

Figure 6.10 The comparison of simulated PC band diagram (figure 6.2) and experiment data (figure 6.6).

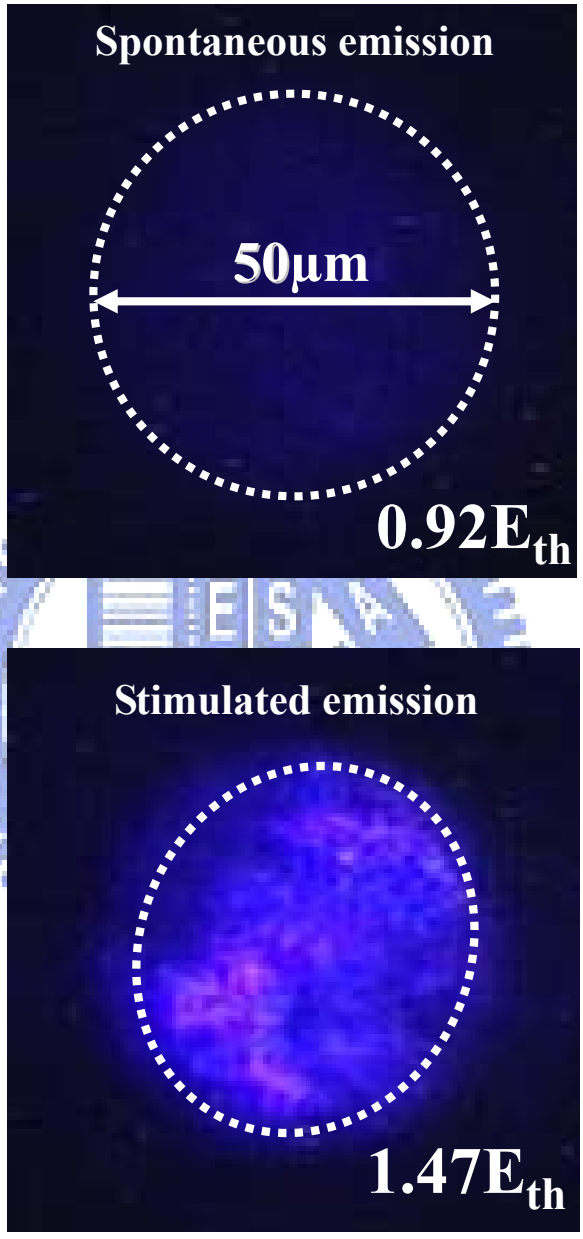

Figure 6.11 (A) The spontaneous emission image at $0.92E_{th}$ (pumping spot size was about 50μm) and (B) The laser emission image at $1.47E_{th}$.

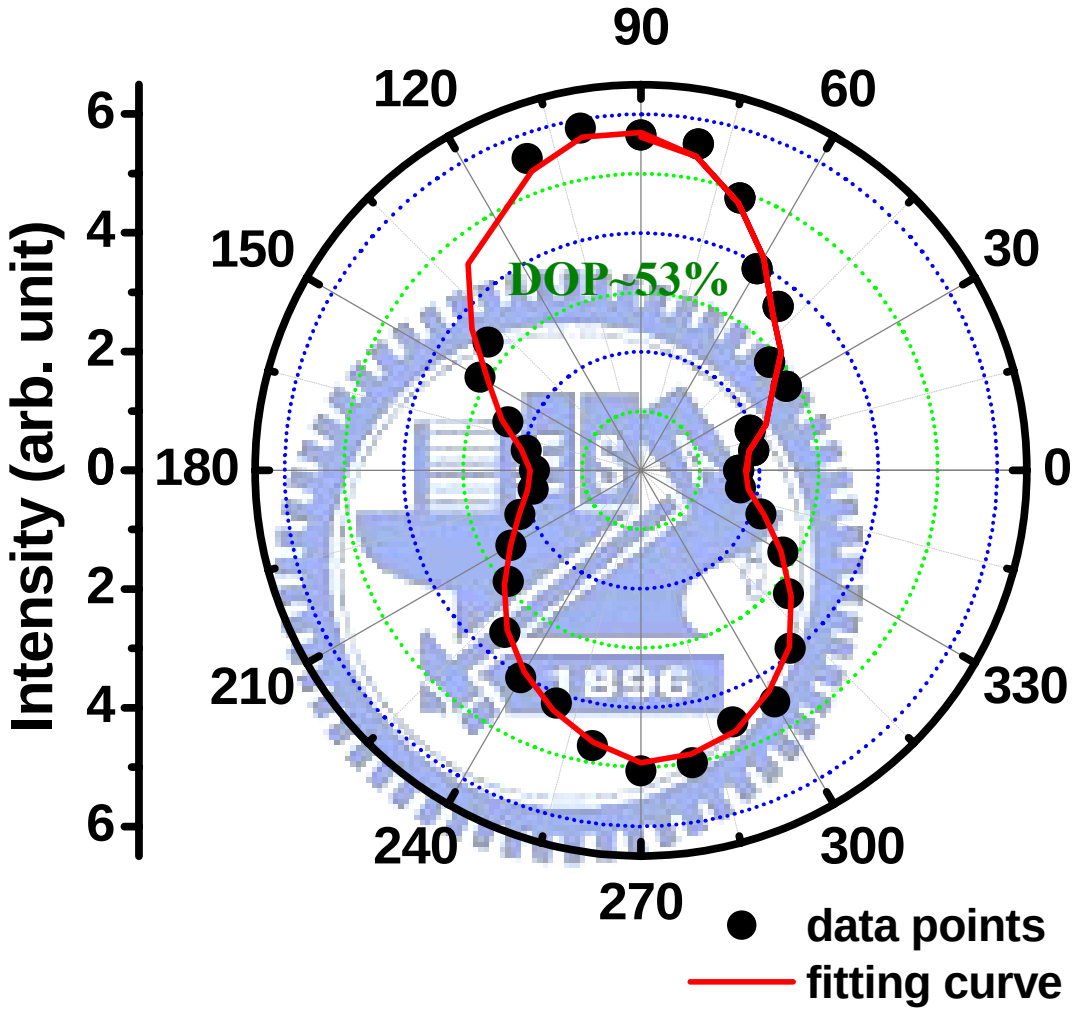

Figure 6.12 The laser emission intensity of a PCSEL as a function of the angle of the polarizer.

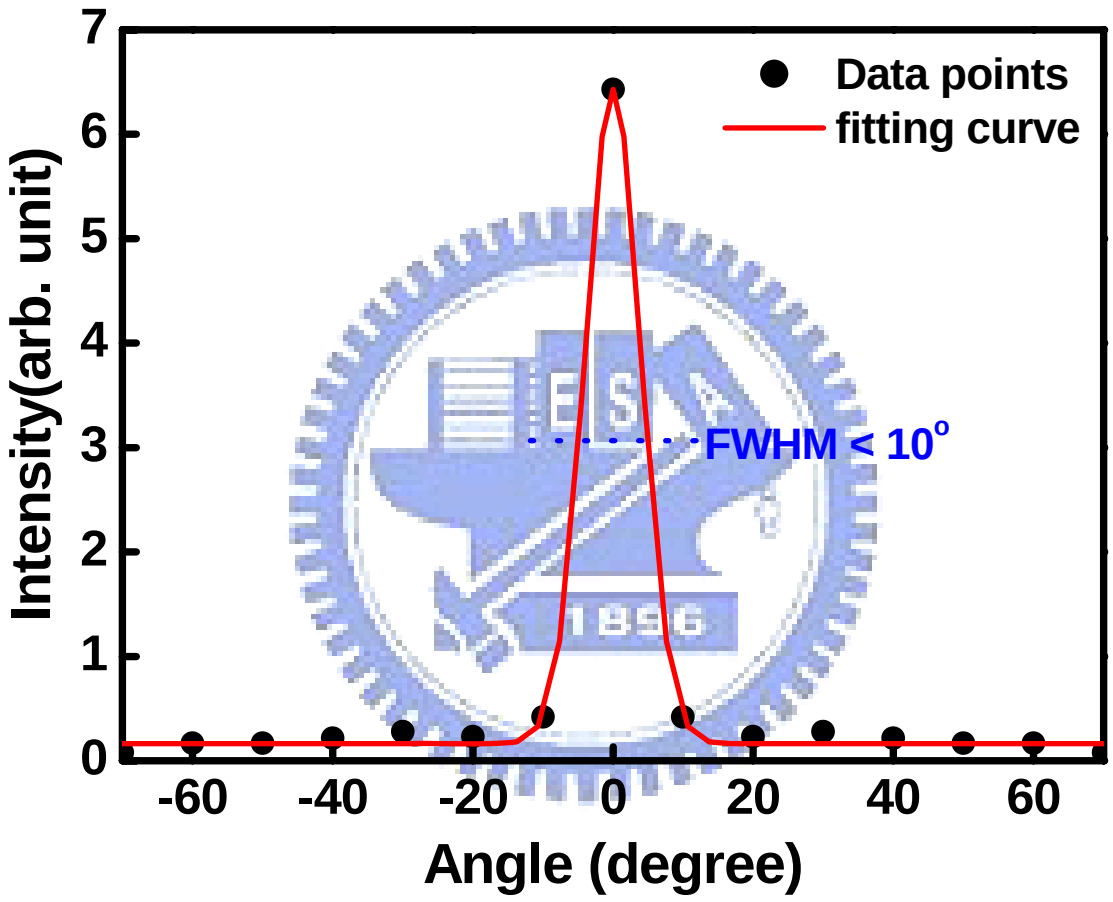

Figure 6.13 The laser emission intensity of a PCSEL as a function of the detecting angle of the fiber.

Chapter 7

Conclusions and Future Works

In conclusion, we have demonstrated the fabrication of the optically-pumped nitride-based vertical cavity surface emitting laser (VCSEL) and the photonic crystal surface emitting laser (PCSEL), and investigated characteristics of these two kinds of lasers. We also have established the fabrication process for nitride-based VCSELs and used the process to complete a cuurent-injected high-Q micro-cavity light emitting diode (MCLED). These achievements are listed and described as following:

(1) The demonstration of laser performances of an optically-pumped nitride-based VCSEL

A nitride-based VCSEL with hybrid DBR mirrors, consisting of AlN/GaN DBR and Ta_2O_5/SiO_2 was fabricated. The laser action was achieved under the optical pumping at room temperature with a threshold pumping energy density of about 2.6 mJ/cm^2. The GaN VCSEL emits 456 nm blue wavelength with a linewidth of 0.2 nm and the laser beam shows a degree of polarization of about 84%. Besides, the laser shows a high characteristic temperature to be about 244 K and a small divergence angle to be about 7.6^o. The coupling efficiency of spontaneous emission (β) of our VCSEL was fitted to be a value as high as 0.02. This β value of the VCSEL is three order of magnitude higher than that of the typical edge emitting semiconductor lasers (normally about 10^{-5}) [1, 15] indicating the enhancement of the spontaneous emission into a lasing mode by the high quality factor microcavity effect in the VCSEL structure.

(2)The demonstration of specific lasing phenomena resulting from the

inhomogeneous gain and cavity

We have investigated the multiple laser spots and stable mode behaviors of nitride-based VCSEL using optical pumping. The non-uniform PL intensity and wavelength distribution were measured for understanding the possible gain and cavity distributions. The multiple laser spots could be attributed to the inhomogeneous gain in our structure. Besides, the optical pumping was carried out at four regions with different PL intensity distribution to study the relation between lasing behavior and gain distribution. All these four regions could achieve lasing operation. However, the emission patterns of laser emission in these four regions are very different. Those patterns were very similar to TEM_{00}, TEM_{01}, TEM_{02}, and TEM_{11}. Furthermore, these modes individually and stably existed in those pumping regions at high pumping energy.

(3) The demonstration of fabrication and characteristics of a high-Q nitride-based MCLED

We have established the fabrication for the current-injected nitride-based VCSEL. The cavity loss and current confinement of the current-injected devices were optimized by using ITO and ion implantation, respectively. We also have used the established process to fabricate a high-Q GaN-based MCLED with a 29-pair high-reflectivity AlN/GaN DBR (R = 99%), a 5-λ optical thickness $In_{0.2}Ga_{0.8}N$/GaN active *pn*-junction region, an ITO transparent current spreading layer and an 8-pairs SiO_2/Ta_2O_5 DBR (R = 99%). The MCLED showed a very narrow linewidth of 0.52 nm equivalent to a cavity Q value of 895 at a driving current of 10 mA and a dominant emission peak wavelength at 465.3 nm. The MCLED also showed an invariant emission peak wavelength with varying current and temperature. The results in this report should be promising for developing GaN-based VCSELs.

(4)The demonstration of fabrication and characteristics of a novel nitride-based PCSEL

We have demonstrated the fabrication and characteristics of the nitride-based 2-D PCSEL. We also simulated the band diagram of the PC structure to realize the lasing mechanism by using plane-wave expansion method. The laser action of photonic crystal devices was achieved under the optical pumping at room temperature. The lasing characteristics in these devices which have different lattice constants (a=190-300 nm) and emit different lasing wavelengths were measured and realized using the plot of normalized frequencies as a function of the lasing wavelengths. All these devices showed a similar threshold pumping energy densities to be about 3.5mJ/cm^2. These nitride-based 2-D PCSELs emit violet wavelengths ranging from 395nm to 425nm with a linewidth of about 0.11 nm. The degree of polarization and the divergence angle of the laser emission were measured to be about 53% and smaller than 10^o, respectively. The measured emission images of the laser indicated that the stimulated emission occurs over a large area, and the lasing spectrum shows the laser is a single mode laser. We also found that normalized frequency of each laser emission from photonic crystal devices can exactly correspond to the points of Brillouin-zone boundary, Γ、M、K points. Furthermore, the device with a larger lattice constant of PC would lase at the PC band edge with a larger normalized frequency. This observation could be a direction for designing this kind of laser device. These results suggest PCSEL could have strong competitiveness for the application of high power and single mode lasers.

Future Works

With these achievements, we have the enough ability to further develop novel micro-cavity light emitters, such as the current-injected VCSEL, the polariton laser, the single photon emitter, and the photonic crystal laser. The polariton laser is a very potential device to achieve thresholdless operation. The single photon emitter is a strong cansidate to be the light source for next generation quantum information technology. All these studies provide some

information for us to improve our techniques toward those goals. These future works are described as following:

1. To improve epitaxy technique to achiever high-reflectivity AlN/GaN DBR

For a polariton laser or current-injected VCSEL, the hight reflectivity of DBRs is very important. Only high enough reflectivity of DBRs could provide a very high quality and very low loss cavity for lowering threshold of VCSELs and enhancing the coupling between cavity photons and excitons. Although we have achieved a high reflectivity of 99%, the reflectivity is still not enough until achieving the value above 99.9%.

2. To improve the uniformity of the active region and the cavity

Our VCSEL is a just several micro-meters laser spot. The size of laser should be improved as large as possible. In our study, this phenomenon is associated with the uniformity of the cavity and the active region. Therefore, the uniformity of epitaxial structure should be further improved.

3. To improve the resistivity of micro-cavity light emitting devices and decreasing the heating effect

The fabricated micro-cavity light emitting device shows a high resistivity of several hundred ohm probably resulting from the non-optimized n-type doping and the current crowding at small current aperture. This high reflectivity would cause a great amount of heat to degrade performances of devices and to limit the operation current.

4. To develop the current-injected nitride-based PCSEL

The fabrication process of the PC laser device should be established. The schematic diagram of the device is shown in figure 7.1. This kind of laser could have large-area and single-mode lasing. That means the tolerance of uniformity for this laser is relatively large compared to VCSEL. It could be a strong candidate to be the next generation high power and single mode laser device.

5. To understand the polariton characteristics of nitride-based micro-cavity

The polariton formed by strong coupling between cavity photons and excitons could be observed in a very high-Q micro-cavity. Especially, nitride materials could have lots of excitons at room temperature; that is, the polariton emission in nitride cavity could be observed at room temperature and further achieve lasing action and Boson condensation. In order to achieve thresholdless laser and well control photons, the realization of polariton in nitride-based micro-cavity is necessary.

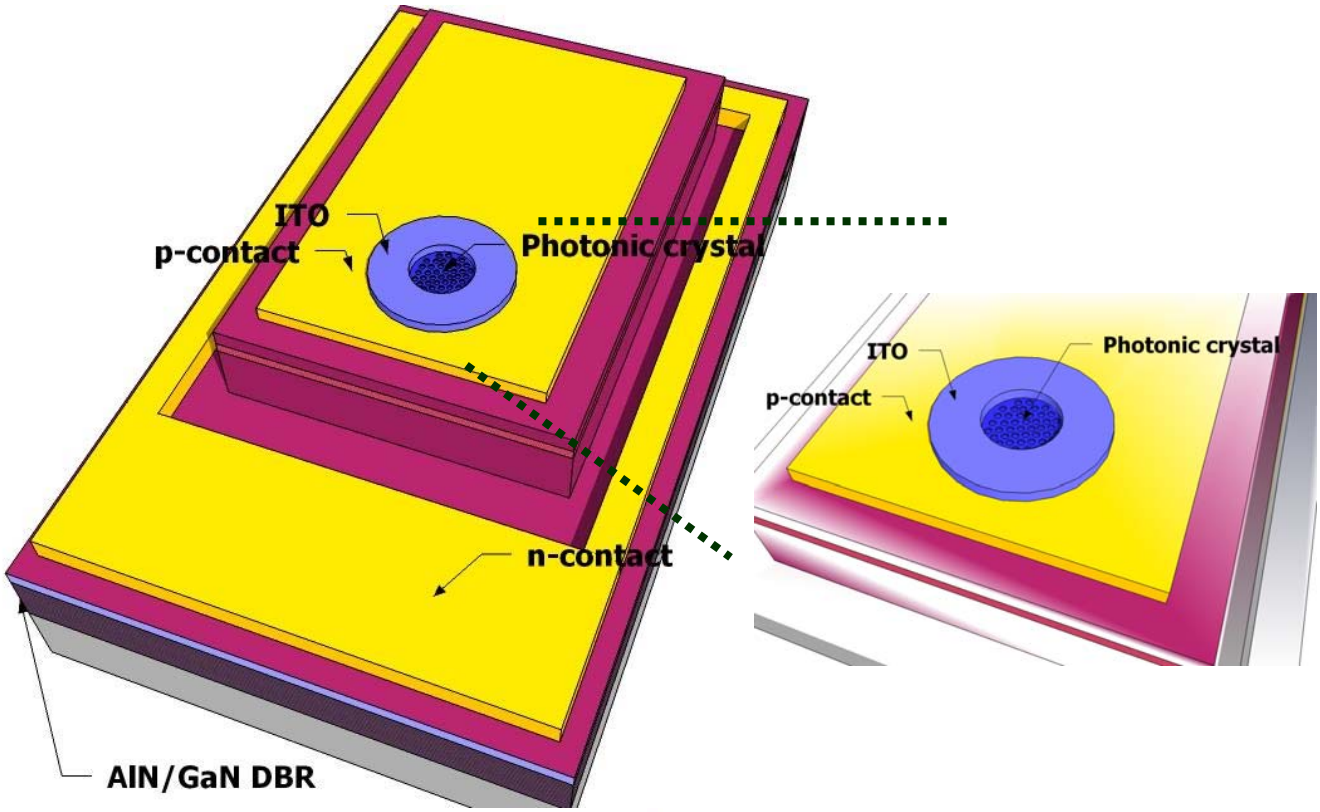

Figure 7.1 Schematic diagram of a photonic crystal surface emitting laser.

Publication List

Journal Papers:

1. **C. C. Kao**, H.W. Huang, J.Y. Tsai, C.C. Yu, C.F. Lin, H.C. Kuo, and S.C. Wang, "Study of dry etching for GaN and InGaN-based laser structure using inductively coupled plasma reactive ion etching", *Mater. Sci. Eng. B*, **107**, 283-288 (2004).
2. H. W. Huang, **C.C. Kao**, J.T. Chu, H.C. Kuo, S.C. Wang, C.C. Yu, and C.F. Lin, "Investigation of GaN LED with Be-implanted Mg-doped GaN layer", *Mater. Sci. Eng. B*., **113**, 19-23 (2004).
3. H. W. Huang, **C.C. Kao**, J.Y. Tsai, C.C. Yu, C.F. Chu, J.Y. Lee, S.Y. Kuo, C.F. Lin, H.C. Kuo, S.C. Wang, "Effect of rapid thermal annealing on beryllium implanted p-type GaN" *Mater. Sci. Eng. B*. **107**, 237-240 (2004).
4. J. T. Chu, H. C. Kuo, **C. C. Kao**, H.W. Huang, C. F. Chu, C. F. Lin, and S. C. Wang, "Fabrication of p-side down GaN vertical light emitting diodes on copper substrates by laser lift-off", *phys. stat. sol. (c)*, **1**, pp.2413–2416 (2004).
5. H. W. Huang, **C. C. Kao**, T. H. Hsueh, C. C. Yu, C. F. Lin, J. T. Chu, H. C. Kuo, and S. C. Wang, "Fabrication of GaN-based nanorod light emitting diodes using self-assemble nickel nano-mask and inductively coupled plasma reactive ion etching", *Mater. Sci. Eng. B*. **113**, 125-129 (2004).
6. **C. C. Kao**, Y. C. Peng, H. H. Yao, J. Y. Tsai, Y. H. Chang, J. T. Chu, H. W. Huang, T. T. Kao, T. C. Lu, H. C. Kuo, and S. C. Wang, and C. F. Lin, "Fabrication and performance of blue GaN-based vertical-cavity surface emitting laser employing AlN/GaN and Ta2O5 /SiO2 distributed Bragg reflector" *Appl. Phys. Lett*. **87**, 081105 (2005).
7. **C. C. Kao**, H. C. Kuo, H. W. Huang, J. T. Chu, Y. C. Peng, Y. L. Hsieh, C. Y. Luo,

Shing-Chung Wang, Chang-Chin Yu, and Chia-Feng Lin, "Light–Output Enhancement in a Nitride-Based Light-Emitting Diode With 22° Undercut Sidewalls" *IEEE Photon. Technol. lett.*, **17**, pp.19-21 (2005).

8. H. W. Huang, J. T. Chu, **C. C. Kao**, T.H. Hseuh, T. C. Lu, H. C. Kuo, S. C. Wang and C. C. Yu, **"**Enhanced light output of an InGaN/GaN light emitting diode with a nano-roughened p-GaN surface", *Nanotechnology*, **16**, pp**.**1844–1848 (2005).

9. H. W. Huang, **C. C. Kao**, J. T. Chu, H. C. Kuo, S. C. Wang, and C. C. Yu, "Improvement of InGaN–GaN Light-Emitting Diode PerformanceWith a Nano-Roughened p-GaN Surface" *IEEE Photon. Technol. lett.*, **17**, pp.983-985 (2005).

10. J. T. Chu, H. W. Huang, **C. C. Kao**, W. D. Liang, F. I Lai, C. F. Chu, H. C. Kuo and S. C. Wang, "Fabrication of Large-Area GaN-Based Light-Emitting Diodes on Cu Substrate" *Jpn. J. Appl. Phys.*, **44**, pp.2509-2511 (2005).

11.T. H. Hsueh, H. W. Huang, **C. C. Kao**, Y. H. Chang, M. C. Ou-Yang, H. C. Kuo and S. C. Wang,"Characterization of InGaN/GaN Multi-Quantum-Well Nanorods Fabricated by Plasma Etching with Self-assembled Nickel Metal Nanomasks", *Jpn. J. Appl. Phys.*,**44**, pp.2661-2663 (2005).

12. T. H. Hsueh, J. K. Sheu, H. W. Huang, J. Y. Chu, **C. C. Kao**, H. C. Kuo, and S. C. Wang, "Enhancement in Light Output of InGaN-Based Microhole Array Light-Emitting Diodes" *IEEE Photon. Technol. lett.*, **17**, pp.1163-1165 (2005).

13. J.T. Chu, **C.C. Kao**, H. W. Huang, W.D. Liang, C. F. Chu, T.C. Lu, H.C. Kuo and S.C. Wang, "Effects of Different n-Electrode Patterns on Optical Characteristics of Large-Area p-Side-Down InGaN Light-Emitting Diodes Fabricated by Laser Lift-Off" *Jpn. J. Appl. Phys.*, 44, 7910-7912 (2005).

14. **C. C. Kao**, T. C. Lu, H. W. Huang, J. T. Chu, Y. C. Peng, H. H. Yao, J. Y. Tsai, T. T. Kao, H. C. Kuo and S. C. Wang, "The Lasing Characteristics of GaN-Based Vertical-cavity Surface-Emitting Laser with AlN/GaN and Ta2O5/SiO2 Distributed Bragg

Reflectors", *IEEE Photon. Technol. lett*., **18**, 877-879 (2006).

15. C. H. Lin, J. Y. Tsai, **C. C. Kao**, H.C. Kuo, C. C. Yu, J. R. Lo, and K. M. Leung, "Enhanced Light Output in InGaN-based Light-Emitting Diodes with Omnidirectional One-dimensional Photonic Crystals", *Jpn. J. Appl. Phys.*, 45, 1591-1593 (2006).

16. Y. C. Peng, **C. C. Kao**, H. W. Huang, J. T. Chu, T. C. Lu, H. C. Kuo, S. C. Wang, and C. C. Yu, "Fabrication and characteristics of GaN-based Microcavity LEDs with high reflectivity AlN/GaN DBRs", *Jpn. J. Appl. Phys.*, 45, 3446-3448 (2006).

17. J.T. Chu, T. C. Lu, H.H. Yao, **C.C. Kao**, W.D. Liang, J.Y. Tsai, H.C. Kuo and S.C. Wang, "Room Temperature Operation of Optically Pumped Blue-violet GaN-based VCSELs Fabricating by Laser Lift-off Technique" *Jpn. J. Appl. Phys.*, 45, 2556-2558 (2006).

18. H. W. Huang, **C.C. Kao**, Y.A. Chang, H.C. Kuo ., L.H. Laih, and S.C. Wang, "A novel method to improve VCSELs oxide-confined aperture uniformity using selective As+-implanted underlying layer", *Mater. Chem. Phys.*, 97, 10-13 (2006).

19. H. W. Huang, J. T. Chu, **C. C. Kao**, T. H. Hsueh, T. C. Lu, H. C. Kuo, S. C. Wang, C. C. Yu, and S. Y. Kuo, "Enhanced light output in InGaN/GaN Light Emitting Diodes with Excimer Laser Etching Surface", *Jpn. J. Appl. Phys.*, 45 (4B), 3442-3445 (2006).

20. H. W. Huang, **C.C. Kao**, J.T. Chu, W.D. Liang, H.C. Kuo, S.C. Wang, and C.C. Yu, "Improvement of InGaN/GaN light emitting diode performance with a nano-roughened p-GaN surface by excimer laser-irradiation", *Mater. Chem. Phys.*, 99, 414-417 (2006).

21. F. I. Lai, W. Y. Chen, **C. C. Kao**, H. C. Kuo and S. C. Wang, "Light-Output Enhancement of GaN-Based Light-Emitting Diodes by Photoelectrochemical Oxidation in H_2O", *Jpn. J. Appl. Phys*, 45, 6927-6929 (2006).

22. J. T. Chu, T. C. Lu, M. You, B. J. Su, **C. C. Kao**, H. C. Kuo, and S. C. Wang, " Emission Characteristics of Optically Pumped GaN-Based Vertical-Cavity Surface-Emitting Lasers", *Appl. Phys. Lett.*, **89**, 121112 (2006).

23. G. R. Lin, H. C. Kuo, H. S. Lin, and **C. C. Kao**, "Rapid Self-Assembly of Ni Nanodots on

Si Substrate Covered by a Less-Adhesive and Heat-Accumulated SiO2 Layers", *Appl. Phys. Lett.*, **89**, 073108 (2006).

24. **C. C. Kao**, H. C. Kuo, K. F. Yeh, J. T. Chu, W. L. Peng, T. C. Lu, and S. C. Wang, "Light–Output Enhancement of Nano-Roughened GaN Laser Lift-Off Light-Emitting Diodes Formed by ICP Dry Etching" *IEEE Photon. Technol. lett*.,19, 849-851 (2007).
25. H. W. Huang, **C. C. Kao**, J. T. Chu, W. C. Wang, T. C. Lu, H. C. Kuo, S. C. Wang C. C. Yu, and S. Y. Kuo, "Investigation of InGaN/GaN Light Emitting Diodes with Nano-roughened surface by Excimer Laser Etching Method", *Mater. Sci. Eng. B*, 136, 182-186 (2007).
26. T. C. Lu, T. T. Kao, **C. C. Kao**, J. T. Chu, K. F. Yeh, L. F. Lin, Y. C. Peng, H. W. Huang, H. C. Kuo, and S. C. Wang, "GaN-Based High-Q Vertical-cavity Light Emitting Diodes" has been accepted by *IEEE Electron Device Lett.*

Conference Papers:

1. **C. C. Kao**, H. H. Yao, Y. C. Peng, T. C. Lu, H. C. Kuo and S. C. Wang, "An Optically Pumped Blue GaN-Based Vertical-Cavity Surface Emitting Laser Employing AlN/GaN and Ta_2O_5/SiO_2 Distributed Bragg Reflectors" *PR/CLEO 2005***,** paper CTuJ3-6.
2. **C. C. Kao**, Y. C. Peng**,** J. Y. Tsai, C. F. Lin, H. C. Kuo, and S. C. Wang, "Fabrication and Characteristic of InGaN/GaN Micro-Cavity Emitter," APWS 2005**.**
3. **C. C. Kao**, J. T. Chu, H. W. Huang, Y. C. Peng, C. C. Yu, Y. L. Hseih, C. F. Lin, H. C. Kuo, and S. C. Wang, "InGaN-Based Light-Emitting Diode With Undercut Side Wall," LEOS 2004.
4. H. W. Huang, T. H. Hsueh, J. T. Chu, **C. C. Kao**, Y. H. Chang, M. C. Ou-Yang, H. C. Kuo, and S.C. Wang, "InGaN/GaN Multi-Quantum-Well Nanorods Fabricated by Plasma Etching Using Self-assembled Nickel Nano-masks**"** LEOS 2004.
5. J. T. Chu, W. D. Liang, **C.C. Kao**, H. W. Huang,T. C. Lu, H. C. Kuo and S. C. Wang,

"Optically Pumped GaN-based Vertical Cavity Surface Emitting Laser at Room Temperature" *PR/CLEO 2005.*

6. Y. C. Peng**, C. C. Kao**, J. Y. Tsai, T. C. Lu, H. H. Yao, T. T. Kao, C. F> Lin, H. C. Kuo, and S. C. Wang, "Fabrication and Characteristics of GaN-Based Microcavity LEDs with High Reflectivity AlN/GaN DBRs," paper No. 5613, SSDM 2005.

7. H.W. Huang, T.H. Hsueh, **C.C. Kao**, Y.H. Chang, M.C. Ou-Yang, H.C. Kuo, S.C. Wang, "Fabrication and Characterization of InGaN-Based Nanorods by Plasma Etching with Nanoscale Nickel Metal Islands," The 1st international conference on one-dimensional nanomaterials (ICON) 2005, NAC106.

8. H. W. Huang, T. H. Hsueh, **C. C. Kao**, Y. H. Chang, M.C. Ou-Yang, H. C. Kuo and S. C. Wang, "Fabrication of InGaN Multi-Quantum-Well Nanorod by Ni Nano-Mask", The IUMRS International Conference in Asia (IUMRS-ICA) , pp.168 (2004).

9. T. H. Hsueh, H. W. Huang, **C. C. Kao**, Y. H. Chang, M. C. Ou-Yang, H. C. Kuo, S. C. Wang," InGaN/GaN Multi-Quantum-Well Nanorods Fabricated by Plasma Etching Using Self-assembled Nickel Nano-masks", SSDM 2004.

10. C. C. Kao, T. C. Lu, T. T. Kao, L. F. Lin, H. C. Kuo, S. C. Wang, "The Characteristics of a High-Q GaN Micro-Cavity Light Emitting Diode**",** *CLEO 2007***,** 07-C-1958-CLEO.